

DTIC FILE COPY

4

AD-A214 297

GL-TR-89-0108

Calculation of Source and Structure Parameters
at Regional and Teleseismic Distances

Charles A. Langston
Roy J. Greenfield

Pennsylvania State University
114 Kern Building
University Park, PA 16802

13 April 1989

Final Report
1 February 1987-31 January 1989

APPROVED FOR PUBLIC RELEASE; DISTRIBUTION UNLIMITED

GEOPHYSICS LABORATORY
AIR FORCE SYSTEMS COMMAND
UNITED STATES AIR FORCE
HANSCOM AIR FORCE BASE, MASSACHUSETTS 01731-5000

DTIC
ELECTE
NOV. 13. 1989
S B D

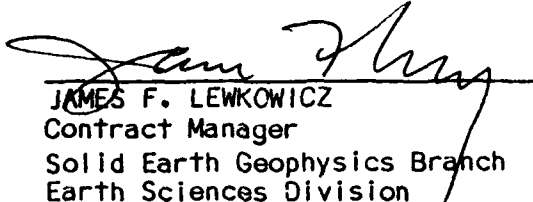
89 11 09 014

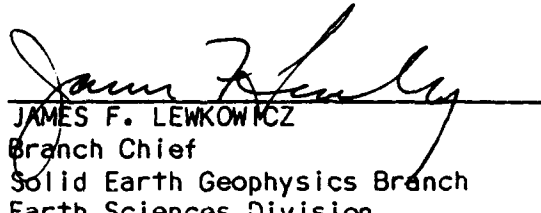
SPONSORED BY
Defense Advanced Research Projects Agency
Nuclear Monitoring Research Office
ARPA ORDER NO. 5299

MONITORED BY
Air Force Geophysics Laboratory
Contract No. F19628-87-K-0024


The views and conclusions contained in this document are those of the authors and should not be interpreted as representing the official policies, either expressed or implied, of the Defense Advanced Research Projects Agency or the U.S. Government.

This technical report has been reviewed and is approved for publication.


JAMES F. LEWKOWICZ
Contract Manager
Solid Earth Geophysics Branch
Earth Sciences Division


JAMES F. LEWKOWICZ
Branch Chief
Solid Earth Geophysics Branch
Earth Sciences Division

FOR THE COMMANDER


DONALD H. ECKHARDT, Director
Earth Sciences Division

This report has been reviewed by the ESD Public Affairs Office (PA) and is releasable to the National Technical Information Service (NTIS).

Qualified requestors may obtain additional copies from the Defense Technical Information Center. All others should apply to the National Technical Information Service.

If your address has changed, or if you wish to be removed from the mailing list, or if the addressee is no longer employed by your organization, please notify AFGL/DAA, Hanscom AFB, MA 01731-5000. This will assist us in maintaining a current mailing list.

Do not return copies of this report unless contractual obligations or notices on a specific document requires that it be returned.

REPORT DOCUMENTATION PAGE

1a. REPORT SECURITY CLASSIFICATION Unclassified			1b. RESTRICTIVE MARKINGS	
2a. SECURITY CLASSIFICATION AUTHORITY			3. DISTRIBUTION/AVAILABILITY OF REPORT Approved for public release; Distribution unlimited	
2b. DECLASSIFICATION/DOWNGRADING SCHEDULE				
4. PERFORMING ORGANIZATION REPORT NUMBER(S)			5. MONITORING ORGANIZATION REPORT NUMBER(S) GL-TR-89-0108	
6a. NAME OF PERFORMING ORGANIZATION Pennsylvania State University		6b. OFFICE SYMBOL (if applicable)	7a. NAME OF MONITORING ORGANIZATION Geophysics Laboratory	
6c. ADDRESS (City, State, and ZIP Code) 114 Kern Building University Park, PA 16802			7b. ADDRESS (City, State, and ZIP Code) Hanscom AFB Massachusetts 01731-5000	
8a. NAME OF FUNDING / SPONSORING ORGANIZATION		8b. OFFICE SYMBOL (if applicable)	9. PROCUREMENT INSTRUMENT IDENTIFICATION NUMBER F19628-87-K-0024	
8c. ADDRESS (City, State, and ZIP Code)			10. SOURCE OF FUNDING NUMBERS	
			PROGRAM ELEMENT NO. 61101E	PROJECT NO. 7A10
11. TITLE (Include Security Classification) Calculation of Source and Structure Parameters at Regional and Teleseismic Distances				
12. PERSONAL AUTHOR(S) Charles A. Langston; Roy J. Greenfield				
13a. TYPE OF REPORT FINAL REPORT		13b. TIME COVERED FROM 2/1/87 TO 1/31/89	14. DATE OF REPORT (Year, Month, Day) 1989 April 13	
15. PAGE COUNT 130				
16. SUPPLEMENTARY NOTATION				
17. COSATI CODES			18. SUBJECT TERMS (Continue on reverse if necessary and identify by block number) Scattering Anelasticity Pnl waves Teleseismic body waves Receiver functions Mantle structure CODA Q Ps Conversions	
FIELD	GROUP	SUB-GROUP		
19. ABSTRACT (Continue on reverse if necessary and identify by block number) Teleseismic receiver functions for structure under Pasadena, California (PAS) are derived from azimuthally distributed teleseismic P waves recorded on Benioff 1-90 instrumentation. The broadband three-component Benioff 1-90 system is peaked at a 1-s period and allows resolution of major crustal interfaces from large Ps conversions seen in the receiver function data. The observed body wave data are quite complex, showing exceptionally large Ps conversions and scattered waves on horizontal components. Radial and tangential motions are of equal magnitude and show major off-azimuth converted Ps waves, suggesting large-scale crustal heterogeneity beneath the station. Stochastic simulations of one-dimensional plane layered structure show that geologically unreasonable one-dimensional models are required to fit the data. The observed coda decay yields a scattering Q estimate of 239 at a 2-s period using an energy flux model for a propagating plane wave interacting with a scattering layer over a homogeneous half-space. Observed and synthetic coda decay follows the theoretical exponential decay predicted by the model and is due entirely to diffusion of coda energy out of the layer into the half-space. PAS coda				
20. DISTRIBUTION/AVAILABILITY OF ABSTRACT <input type="checkbox"/> UNCLASSIFIED/UNLIMITED <input type="checkbox"/> SAME AS RPT <input type="checkbox"/> DTIC USERS			21. ABSTRACT SECURITY CLASSIFICATION Unclassified	
22a. NAME OF RESPONSIBLE INDIVIDUAL James Lewkowicz			22b. TELEPHONE (Include Area Code) (617) 377-3222	22c. OFFICE SYMBOL GL/LWH

is compared to coda from deep teleseisms, recorded at State College, Pennsylvania, and it is seen that scattering is more severe at PAS, as reflected in higher coda levels and slower decay rate. Consideration of energy partitioning and coda amplitude suggests that much of the coda consists of scattered surface waves. Analysis of a major Ps conversion arriving 3 s after direct P indicates that a major crustal discontinuity at about 20 km depth dips at moderate angles to the north under the San Gabriel Mountains. This interface probably represents the crustal tectonic boundary between the Transverse Ranges and the Los Angeles Basin.

The codas of long-period Rayleigh waves recorded at WWSSN and Canadian network stations in Western North America from eight underground explosions at NTS are examined in an effort to separate scattering and anelastic attenuation effects. Coda behavior of 0.1 and 0.2 Hz Rayleigh waves follows coda characteristics seen in studies of short-period S waves. Coda decay rate is seen to be a stable observation over most stations in Western North America and is consistent with the hypothesis that backscattered surface waves from heterogeneities contained within the western half of the continent form the Rayleigh wave coda. The basic data observables of coda level and decay are interpreted using several plausible models. The single scattering model yields a coda Q consistent with previously determined Rayleigh anelastic attenuation coefficients. Separation of anelastic and scattering Q is possible using an energy flux model and shows that scattering Q is one to two orders of magnitude higher than anelastic Q. However, an energy flux model which incorporates a layer of scatterers over a homogeneous half-space shows that all Rayleigh wave attenuation can be explained purely by scattering effects which include Rayleigh to body wave conversion. Coda can be fit equally well by these mutually incompatible models. It is not likely that the mechanisms of scattering or anelastic attenuation can be addressed by coda observations of a single homogeneous data set.

P_{n1} waveforms from two moderate-sized earthquakes in Zambia are used to determine an upper mantle P-wave velocity model for southern Africa. The events are: 5/15/68, $m_b=5.7$, depth = 28 km; and 12/2/68, $m_b=5.9$, depth = 6 km. Focal parameters for these events are constrained by previous workers from teleseismic body wave inversion. Synthetic seismograms are generated for various mantle velocity models using a wavenumber integration method until an acceptable fit to the data is obtained. Quality of fit is measured primarily by the P_n/PL amplitude ratio. Source-station geometry also allows for the independent sampling of the upper mantle beneath the Kapvaal-Rhodesian craton and the mobile belt provinces. Synthetics from a three-layer crust over half-space mantle model do not show prominent precursor arrivals seen in the data; these are interpreted to be P-waves turning in the upper mantle. The synthetics also give a too low P_n/PL amplitude ratio. Synthetics for models with a mantle P-wave velocity gradient of 0.00333/sec fit the cratonic path data very well. Since there is no indication of interaction with a low-velocity zone, this gives a minimum lithospheric thickness of 120 km. A slightly lower gradient is indicated for the mobile belt regions, with a minimum lithospheric thickness of 140 km. Though the data is small, there is no evidence for a major low velocity zone beneath either province. Different velocity gradients between the two provinces implies different temperature structure, which supports the hypothesis that a deep, cool lithospheric root exists beneath the Kapvaal-Rhodesian craton.

Table of Contents

	Page
List of Scientists Contributing to Report	iv
List of Publications Resulting from Total or Partial Sponsorship	iv
Report Summary	v
Task Objectives	v
Technical Problem	v
General Methodology	v
Technical Results	v
Important Findings and Conclusions	vi
Significant Hardware Development	vii
Special Comments	vii
Implications for Further Research	vii
Section 1 - Scattering of Teleseismic Body Waves Under Pasadena, California	1
Section 2 - Scattering of Long-Period Surface Waves in Western North America and the Interpretation of Coda Q Measurements	18
Section 3 - Upper Mantle P-Wave Velocity Structure Beneath Southern Africa from P_n Waves	56

Accession For	
NTIS GRA&I	<input checked="" type="checkbox"/>
DTIC TAB	<input type="checkbox"/>
Unannounced	<input type="checkbox"/>
Justification	
By	
Distribution/	
Availability Codes	
Dist	Avail and/or Special
A-1	

List of Scientists Contributing to Report

C.A. Langston
Robert Clouser
Kristin Vogfjord
Gregory Wagner

List of Publications Resulting from Total or Partial Sponsorship

- Vogfjord, K.S., and C.A. Langston (1987). The Meckering earthquake of 14 October 1968: A possible downward propagating rupture, Bull. Seism. Soc. Am., 77, 1558-1578.
- Langston, C.A.(1987). Depth of faulting during the 1968 Meckering, Australia, earthquake sequence determined from waveform analysis of local seismograms, Jour. Geophys. Res., 92, 11,561-11,574.
- Varadan, V.K., A. Lakhtakia, V.V. Varadan, and C.A. Langston(1987). Radiation characteristics of elastodynamic line sources buried in layered media with periodic interfaces.I.SH-wave analysis, Bull. Seism. Soc. Am., 77, 2181-2191.
- Varadan, V.K., A. Lakhtakia, V.V. Varadan, and C.A. Langston(1987). Radiation characteristics of elastodynamic line sources buried in layered media with periodic interfaces.II. P- and SV-wave analysis, Bull. Seism. Soc. Am., 77, 2192-2211.
- Clouser, R.H.(1988). Upper mantle P-wave velocity structure beneath Southern Africa from P_{nl} Waves, M.S. thesis, Pennsylvania State University.
- Langston, C.A.(1989). Scattering of teleseismic body waves under Pasadena, California, Jour. Geophys. Res., 94, 1935-1951.
- Langston, C.A.(1989). Scattering of long-period Rayleigh waves in western North America and the interpretation of Coda Q Measurements, Bull. Seism. Soc. Am., in press.

Report Summary

Task Objectives

The general objective of this research is to understand the factors important in shaping the seismic signature of small events recorded at local and regional distances. Specific objectives are 1) the identification of deterministic aspects of the wavefield from small earthquakes and explosions to allow the inference of source depth and other source parameters, and 2) to understand the effects of scattering and lithospheric heterogeneity on the propagation of high frequency regional phases. The combined analysis of "deterministic" and "stochastic" wave propagation effects is required to unravel the complexity of regional phases for the purposes of event discrimination.

Technical Problem

Regional phases from small events are affected by complex interactions between source radiation and wave propagation effects due to structure in the crust and upper mantle. Because observations are confined to the high frequency band (>2 Hz), lithospheric heterogeneity becomes important in shaping high frequency regional phases. Typical wave lengths are much shorter than the total travel path and are comparable to known geologic structure. An aspect of the problem of regional wave propagation is examined here involving the nature of coda associated with major arrivals. Simple wholospace scattering models are often applied to the coda of regional S phases to deduce scattering or anelastic attenuation. The level and amplitude decay of coda is a characteristic of the data which seems to be robust for particular regions and can be used to deduce source magnitude, once calibrated. Factors affecting the level of scattering near the source and near the receiver are also obviously important in yield estimation problems and waveform modeling for source parameters. It is important, therefore, to investigate the major assumptions contained in these wholospace models and to determine which are appropriate.

Several problems have been addressed in this research and include analysis of P wave coda from teleseismic events, analysis of long-period Rayleigh wave coda from explosions at NTS, and regional wave propagation of P and S body waves. The first two problems are reciprocal in some respects and involve the nature of scattering of waves in the lithosphere and how such scattering affects the seismogram. The analysis of body wave and surface wave data using similar formalisms is useful in characterizing observed scattered coda waves behind the direct arrivals and in investigating the degree of lithospheric heterogeneity. Specific problems concerning teleseismic P coda waves are 1) determination of the behavior of P wave coda, and 2) deducing the scattering mechanisms involved in supporting high coda energy levels. Long-period Rayleigh waves were studied to determine characteristics of coda, if any, and the relationship of coda Q measurements to other standard attenuation measurements. This study is also a prelude to determining whether Rayleigh coda would be a useful measure of yield. In addition to studies of scattered waves several other deterministic studies of long and short-period waves were performed to determine vertically inhomogeneous earth structure.

General Methodology

The general methodology of this research involves theoretical development of scattering models to apply to time series data and the simulation of wave propagation in models of plane layered elastic earth structure. In all cases synthetic seismograms are computed to compare with the observed seismic data.

Technical Results

The scattering of waves by 2 and 3D heterogeneity in the lithosphere is a complex process which is poorly understood. In the first section of this report, broadband teleseismic P wave data from PAS station was studied to develop an appropriate scattering model. Scattering under the station was seen to be quite severe because of the existence of a substantial tangential component of motion comparable to vertical and radial motions. The level and decay of coda was modeled

first using simple 1D stochastic structure models. The results of this study showed that unreasonably high 1D velocity variations, amounting to 20% and more, were needed to explain the slow decay and high level of coda. The 1D simulations also showed that the single scattering model for a simple plane wave in a homogeneous whole space was not particularly useful in interpreting coda behavior. In fact, the interpretation of coda decay with the single scattering model would imply that scattering attenuation is greatest for those structures which are not heterogeneous. The 1D models showed that decay rate decreases with degree of scattering. Observational aspects of the coda data were modeled using an energy flux model for scattering in a layer over homogeneous halfspace. The energy flux model is a useful parameterization of the teleseismic coda data which can be used in comparative coda studies between seismic stations.

These unusual results prompted a study of coda from regionally propagating waves. The teleseismic scattering model suggested that apparent attenuation deduced from coda decay is strongly affected by the gross distribution of scatterers as well as their density. Fast coda decay with time, and consequently low Q , implies that waves quickly radiate into the mantle rather than being attenuated through scattering losses. Section 2 describes a study of long-period Rayleigh wave coda where various mechanisms of coda formation were investigated. There has been extensive previous work on attenuation of Rayleigh waves in western North America using amplitude decay of fundamental mode Rayleigh waves. The coda study was attempted to first determine if long-period Rayleigh waves had coda (they do) and then to investigate whether scattering mechanisms could be separated from anelasticity (they can't). The single scattering model and two different energy flux models were used to model coda. The results show that coda decay is the most observationally robust measurement and that coda decay could be due to anelastic attenuation. However, an energy flux model which allows the scattering and subsequent radiation of surface wave to body wave conversions into the mantle produces attenuation effects comparable to the scattering of teleseismic P waves seen in the PAS data. Both of these scattering studies raise very interesting questions on the mechanisms of scattering as well as on the role of scatterer geometry in controlling the characteristics of coda.

In conjunction with these studies on coda, an analysis of regional P wave propagation was completed to determine upper mantle structure in the South African shield (Section 3). This was prompted by observations of anomalous P_n waveforms for crustal events believed to be associated with southern extension of the east African rift zone into Zambia. Structure and wave propagation in shield areas is a recurring problem in discrimination and detection since there are large shield areas of Asia and Europe which must be monitored. Past studies of the P_n phase have concentrated in using this phase to infer gross crustal structure and focal mechanisms. In the present study, aspects of the observed P_n phases were used to infer the character of P wave velocity gradients in the upper mantle. The study showed that substantial positive velocity gradients are required to fit the large long-period P_n waves observed in the data. Positive velocity gradients in the uppermost mantle give rise to turning waves and high relative amplitudes for direct P and S wave phases seen at regional distances. This kind of structure is conducive for detection of small events at regional distances. It is also important to recognize when such structure exists between source and receiver since magnitudes and yields determined from direct body wave phases may be overestimated due to the more efficient wave propagation.

Important Findings and Conclusions

Analysis of coda in teleseismic receiver functions suggests that there are other mechanisms which control the formation and decay of scattered coda waves which are separate from intrinsic or scattering attenuation. In particular, the simple geometry of an elastic scattering layer over halfspace produces coda decay which would be interpreted as an attenuation effect but is due to the simple redistribution of scattered energy from the layer to the halfspace. Such effects can be studied first by analyzing coda from teleseismic events at a receiver or array and then applying the parameters of the layer model to an appropriate energy flux model for a source contained within the layer.

Study of regional long-period surface propagation shows that several mechanisms affect coda decay and level. Although coda decay can be explained and is consistent with anelastic

attenuation measured previously, scattering mechanisms can be assumed to create the same effects. This has important implications in the interpretation of coda in all wave propagation regimes.

Significant Hardware Development

N/A

Special Comments

N/A

Implications for Further Research

Scattering Q models are based on a number of assumptions concerning the distribution of the reservoir of energy contained in the scattered field. Further research will concentrate on combined application of teleseismic scattering determinations and regional phase scattering. This combined analysis may offer constraints on scattering physics not obtainable by analysis of each data set alone. Results of this research will have important implications on studies of regional phase propagation, discrimination of small events, and yield estimation problems.

The work performed on this contract has generated several new areas of research which are being pursued. Figure 1 shows results of a finite difference calculation designed to study the energy flux model developed here for teleseismic P waves and receiver scattering. The finite difference model consists of a 2D scattering layer over a homogeneous halfspace (acoustic case only). The calculations are being performed to first test the assumptions that go into the energy flux model and then to gain understanding of the nature of scattering in the 2D layer compared to the 1D structures used before. Simulations in solid elastic structure are also being performed to look at the partitioning of scattered waves into rotational and dilatational fields and how such partitioning affects the interpretations of the parameters of the energy flux model. Such calculations will also be extended to scattering with a source in the layer for regional wave propagation studies.

An observational study of high frequency data recorded by the NORESS array has also been started to investigate regional phases and the influence of deterministic (1D structure) vs stochastic earth structure. Figure 2 displays several wave forms from different events recorded by NORESS. The study is taking advantage of the array capabilities by analyzing any individual phase seen sweeping across the array. k - ω analysis and beam forming is being used to first detect phases and then to model their characteristics using plane layered models. Figure 2 shows the result of stacking individual time windows about an observed phase at the optimal phase velocity (velocity shown by numbers, time windows by vertical dotted lines). Each stack is then patched together, for an event, to display an enhanced seismogram. Incoherent scattered waves are reduced by this method. The stacked data show a number of impulsive phases, some with quite high phase velocities. The high velocities can be understood by considering the crustal structure inferred for the area. For example, the 9.2 km/sec velocity is consistent with a precritical wide angle P reflection from the Moho. Initial results from this study show that a number of unusual phases occur in the data associated with multiples and conversions within the crust. These phases can be used to locate the event as well as determine crustal structure. Ultimately, we want to be able to understand the short-period regional seismogram to find near-source depth phases for discrimination purposes. This particular study is also a prelude to a larger study of scattering of teleseismic and regional P waves at NORESS, following up on several issues associated with the energy flux model developed in this contract.

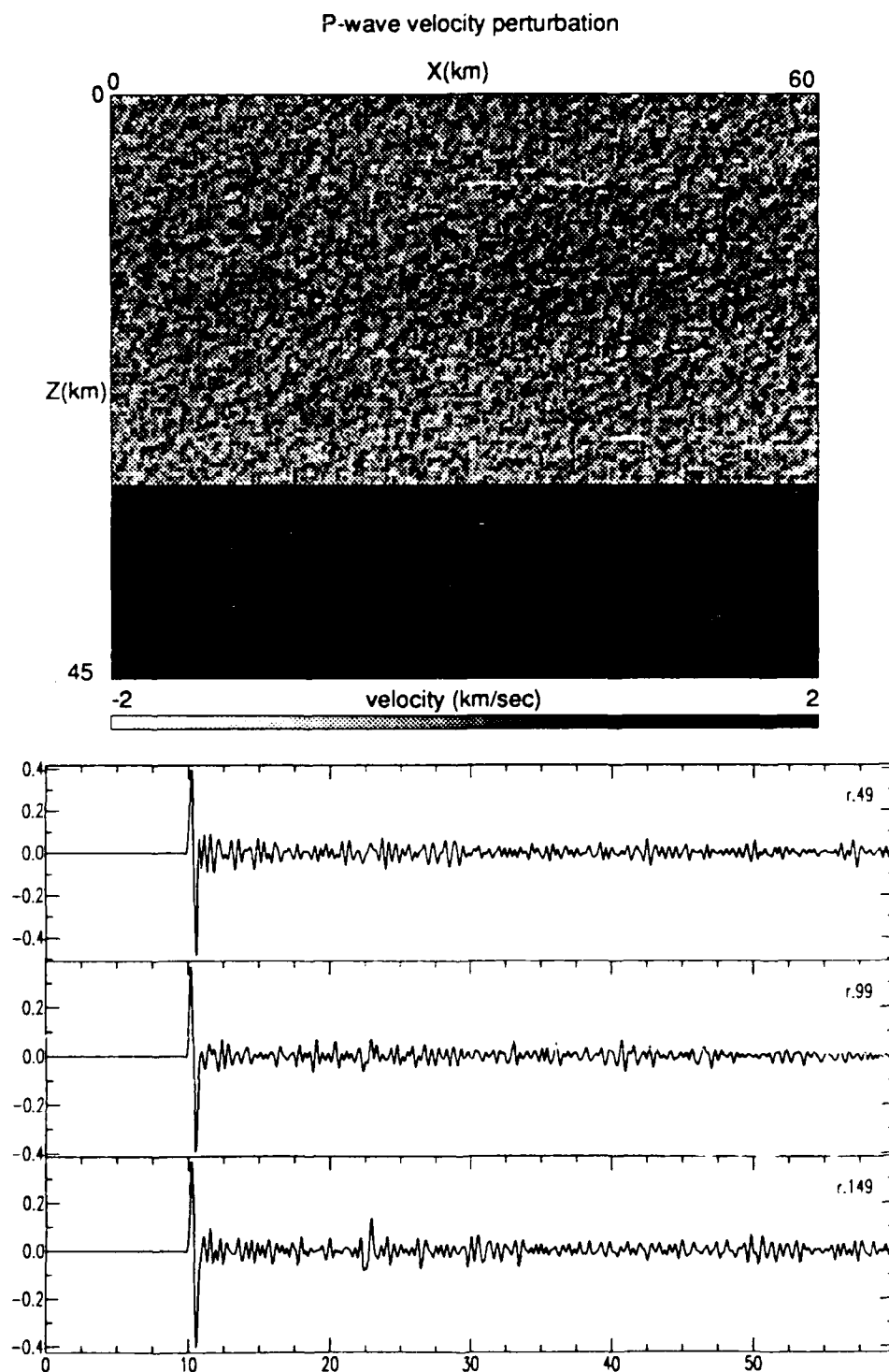


Figure 1 - Layer over halfspace model (top) of a scattering layer with a random velocity described by a 10% standard deviation. Average P wave velocities for the layer and halfspace are 5 and 8 km/sec. respectively. The velocity scale shows deviations from the average. The lower three traces are synthetic seismograms for receivers at the surface near the center of the model. A vertically incident P wave was assumed. Note the long duration of coda and its near-constant level.

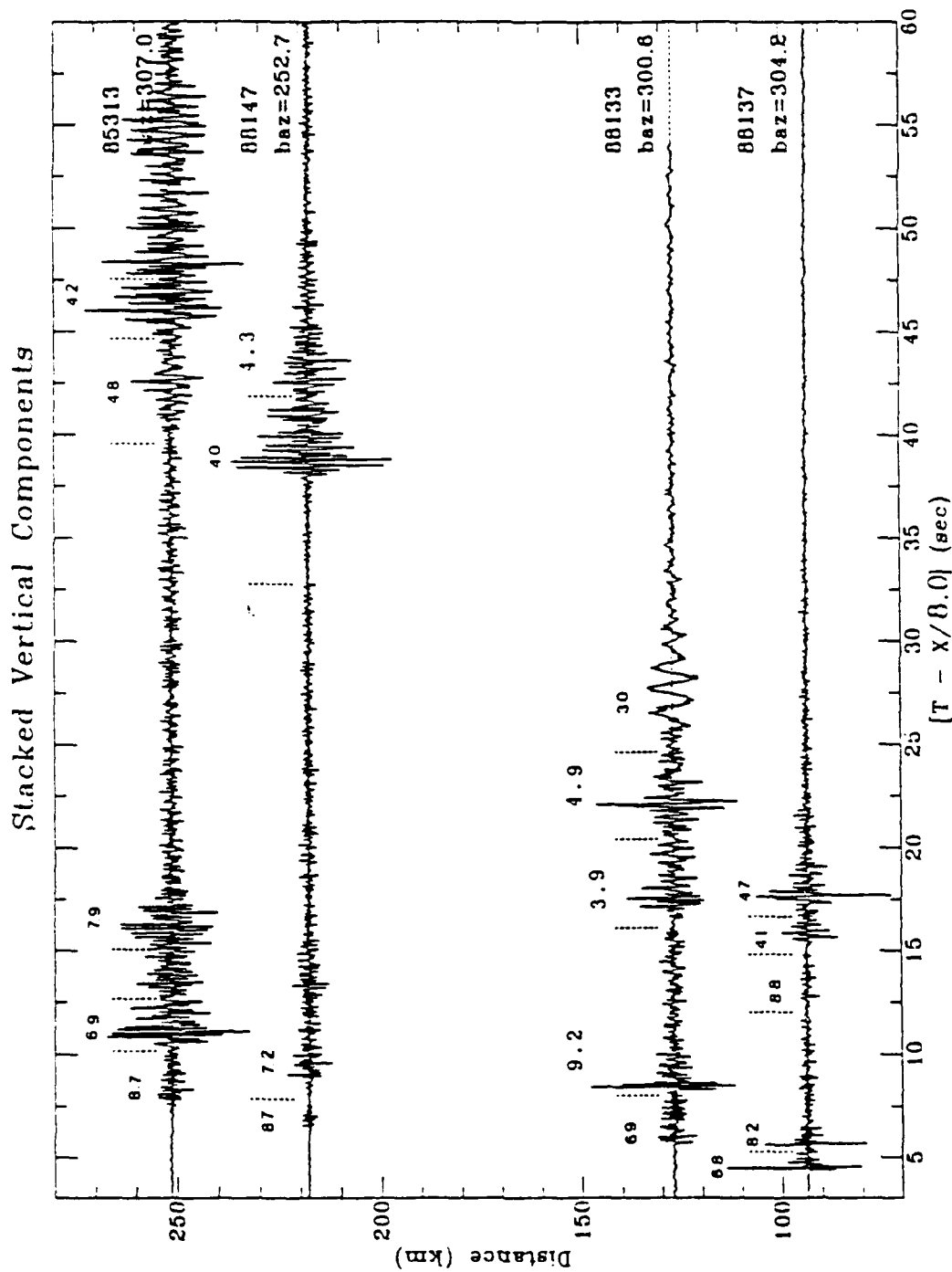


Figure 2 - Enhanced vertical seismograms, normalized to maximum amplitude, plotted as a function of distance. The stacking velocity within each slant-stack time window is indicated.

Scattering of Teleseismic Body Waves Under Pasadena, California

CHARLES A. LANGSTON

Department of Geosciences, Pennsylvania State University, University Park

Teleseismic receiver functions for structure under Pasadena, California (PAS) are derived from azimuthally distributed teleseismic *P* waves recorded on Benioff 1-90 instrumentation. The broadband three-component Benioff 1-90 system is peaked at a 1-s period and allows resolution of major crustal interfaces from large *Ps* conversions seen in the receiver function data. The observed body wave data are quite complex, showing exceptionally large *Ps* conversions and scattered waves on horizontal components. Radial and tangential motions are of equal magnitude and show major off-azimuth converted *Ps* waves, suggesting large-scale crustal heterogeneity beneath the station. Stochastic simulations of one-dimensional plane layered structure show that geologically unreasonable one-dimensional models are required to fit the data. The observed coda decay yields a scattering *Q* estimate of 239 at a 2-s period using an energy flux model for a propagating plane wave interacting with a scattering layer over a homogeneous half-space. Observed and synthetic coda decay follows the theoretical exponential decay predicted by the model and is due entirely to diffusion of coda energy out of the layer into the half-space. PAS coda is compared to coda from deep teleseisms recorded at State College, Pennsylvania, and it is seen that scattering is more severe at PAS, as reflected in higher coda levels and slower decay rate. Consideration of energy partitioning and coda amplitude suggests that much of the coda consists of scattered surface waves. Analysis of a major *Ps* conversion arriving 3 s after direct *P* indicates that a major crustal discontinuity at about 20 km depth dips at moderate angles to the north under the San Gabriel Mountains. This interface probably represents the crustal tectonic boundary between the Transverse Ranges and the Los Angeles Basin.

INTRODUCTION

The analysis of teleseismic receiver functions represents an inexpensive and convenient way of imaging major crustal and upper mantle discontinuities under isolated receivers. The transmissivity of structure under a three-component seismometer is inferred from the timing and amplitude of *Ps* conversions seen on horizontal ground motions and is modeled to determine the location and velocity contrasts of the causative interfaces [Burdick and Langston, 1977; Langston, 1979; Owens, 1984]. The technique has been particularly useful in large-scale structure studies using long-period body waves [e.g., Burdick and Langston, 1977; Langston and Isaacs, 1981; Hebert and Langston, 1985] to determine average crustal thickness and is increasingly being applied to broadband, high-frequency data to obtain more resolution on structure [Owens, 1984; Owens *et al.*, 1984; 1987].

One of the inevitable trade-offs in using higher-frequency data is increased sensitivity to lateral heterogeneity in crustal structure. In one sense this is desirable since a goal of such studies is to determine as much information about structure under the receiver as possible. However, it is also obvious that the wave field is severely spatially aliased through observations made at only a single surface point. Imaging procedures implicitly rely on modeling assumptions such as plane layering or, at most, simple curved interfaces. It is often observed that much of the wave field is inaccessible to standard explanation using simple modeling techniques [Langston, 1979; Owens *et al.*, 1987]. For example, receiver function data often display anomalous wave behavior such as *P* wave particle motions which have significant tangential amplitudes.

A purpose of this paper is to examine strategies of treatment of broadband receiver function data which take into account

both stochastic and deterministic scattering effects due to heterogeneous structure. Structure under the station Pasadena, California (PAS) will be the focus of this effort. This station lies in a geologically complex area of southern California and has had broadband instrumentation over a long period of time (Figure 1). The study was initially motivated by observations of complex particle motions in the teleseismic *P* wave data [Langston, 1977]. The data were previously examined by Lee [1983], who attempted to model the receiver functions using dynamic ray tracing with models consisting of homogeneous layers separated by curved three-dimensional interfaces. Lee's study was partially successful in explaining qualitative aspects of the data for early arrivals, but he found that ray theory was inadequate to explain the high amplitude of inferred converted waves and the duration of signal.

In this paper the receiver function data will be examined from two points of view. The first is from the standard method of treating the data to infer major velocity discontinuities under the station using observations of isolated body wave phases and simple velocity models. *Ps* conversions from teleseismic *P* waves are found to be unusually large and are used to suggest the existence of a large velocity contrast interface in the lower crust which dips to the north under the San Gabriel Mountains.

The other point of view is to treat the data as resulting from an unknown scattering process and to attempt to infer the severity of wave scattering under the station. Using simple measures of the *P* coda amplitude decay along with one-dimensional stochastic structure simulations, the question is asked: Are the data consistent with scattering due to reasonable plane layered structure? The negative answer for PAS suggests that such an analysis can be used to justify or not justify a research effort in modeling data with simple plane layered structure models. The severity of observed scattering under PAS also points out deficiencies in some simple scattering models and the need to develop appropriate models for two- and three-dimensional stochastic structures.

Copyright 1989 by the American Geophysical Union

Paper number 85JB03977

0148-0227/89/88JB-03977\$05.00

The U.S. Government is authorized to reproduce and sell this report. Permission for further reproduction by others must be obtained from the copyright owner.

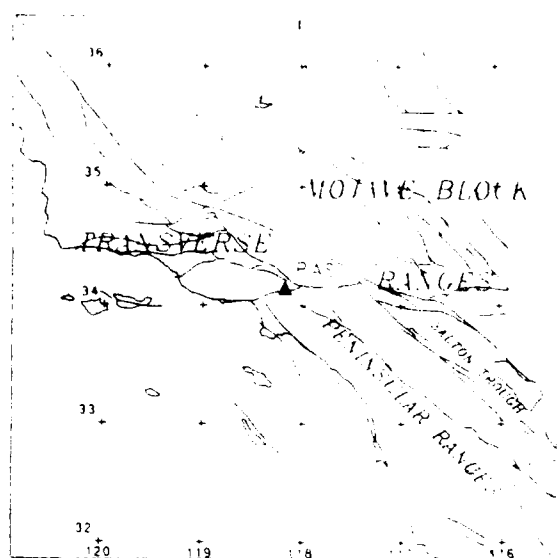


Fig. 1 Sketch map of southern California showing the location of PAS station and major faults of the area.

PAS STATION AND REGIONAL STRUCTURE

PAS station has been in operation since the mid-1930s and has had a full complement of experimental long- and short-period instrumentation. Of interest to this study are the Benioff 1-90 (seismometer period is 1 s, galvanometer period is 90 s) and, to a lesser extent, the Press-Ewing 30-90 systems. The Benioff 1-90 system is peaked at 1-s period but records across a wide frequency band comparable to the intermediate-period Digital World-Wide Standard Seismograph Network (DWWSSN) passband (see the appendix). The system has routinely recorded teleseisms throughout its existence. Although the data are recorded in analog photographic format, the broad passband of the instrument allows for significant time resolution of crustal *Ps* conversions. This potential, in conjunction with the complexity of the receiver signal [Langston, 1977] as well as the tectonic problems associated with the Transverse Ranges Province of southern California, motivates the present study of crustal structure under the receiver.

PAS station lies near the southern boundary of the Transverse Ranges Province and the Los Angeles Basin-Peninsular Range Province (Figure 1). Crustal thickness from long-range refraction [Hadley and Kanamori, 1977] and time term analysis [Hearn and Clayton, 1986b] suggest that the crust under PAS is about 31 km thick. Geologic structure of the upper crust is known to be quite complex with major active faults separating regions of diverse rock type. For example, crystalline rocks of the San Gabriel Mountains a few kilometers north of PAS abut valley sediments that attain depths of up to 10 km in the surrounding basins [Yerkes et al., 1985]. The geology of the Transverse Ranges and the San Gabriel Mountains suggest that these ranges are in part allochthonous, being thrust over younger rocks of the Peninsular Range Province.

Hadley and Kanamori [1977] review a number of long-range refraction and travel time studies for the area and show that the Transverse Ranges are a locus of both upper mantle and crustal velocity anomalies. Using the Southern California Seismic Network, they showed that *P* delays from a *PKIKP* phase outlined an east-west trending zone of high velocities in

the upper mantle. This zone was studied by Humphreys et al. [1984] using a tomographic imaging technique for teleseismic *P* waves recorded by the network. They determined that the vertical zone of high mantle velocities was contained within the Transverse Ranges Province and attained depths of at least 150 km. This zone was interpreted as a region of mantle downwelling analogous to a subduction zone but driven by relative movements of microplates making up the San Andreas fault system. In this model, upper crustal microplate movements may be decoupled from lower crust and upper mantle structures with the result that the surface expression of the San Andreas fault is offset by a midcrustal horizontal shear zone from the fault at depth [Webb and Kanamori, 1985].

The Transverse Ranges are also a locus of change in crustal structure between the western Peninsular Ranges-Los Angeles Basin and the Mojave Block to the east. Hadley and Kanamori [1977] suggest that a high-velocity lower crustal layer comprises about half of the crust in the Peninsular Ranges but tapers to only a few kilometers in the Mojave Block. Tomographic study of *Pq* and *Pn* waves in southern California [Hearn and Clayton, 1986a, b] support this suggestion by showing slower average velocities in the Mojave Block relative to crust to the west.

A major goal of the present work was initially to provide constraints on crustal thickness under this important transition between tectonic provinces. Site specific information provided by the receiver function technique will complement these earlier crustal and upper mantle structure studies but will also show the presence of a major midcrustal to lower crustal interface.

DATA AND SOURCE FUNCTION EQUALIZATION

Wave form data from 21 teleseismic earthquakes were obtained from the seismogram archives of California Institute of Technology (Table 1). The seismograms were photographed and enlarged for hand digitization. Wave forms were digitized at an irregular sampling interval and interpolated to an equal sampling interval of 0.1 s. Processing included vector rotation of the horizontal components into the theoretical back azimuth of the *P* wave arrival to obtain radial (positive away from the source) and tangential (positive clockwise around the source looking at the receiver) ground motions.

A source function equalization procedure was then performed to remove the instrument response and unknown effective source function from the radial and tangential wave form data [Langston, 1979]. In this procedure the vertical component of motion is assumed to be free of any effect of near-receiver structure (reverberations or conversions) but contains the common instrument response and wave propagation effects from the mantle and near-source region. The data are time-windowed and Fourier-transformed. The vertical spectrum is divided into the horizontal spectra and then multiplied by a Gaussian function to remove high-frequency noise. The spectral division is also accompanied by prewhitening the vertical component spectra using a "water level" parameter to remove spurious spectral holes. The water level used for data considered here was 0.1% of the maximum of the vertical component amplitude spectrum. The Gaussian filter used is equivalent to a Gaussian pulse in the time domain with a half width of 1 s (i.e., $a = 1.67$ in $e^{-a^2 t^2}$).

Figure 2 shows examples of wave form data for events in the three major back azimuth ranges 128°, 235°, and 315°.

TABLE 1. Event Parameters for Pasadena Data

Origin Date	Time, UT	Latitude, deg	Longitude, deg	M_b	Depth, km	Distance, deg	Back Azimuth, deg	Stack Group
March 17, 1966	1550:33	21.1S	179.2W	6.2	639	79.9	236.1	235
Nov. 20, 1971	0728:01	13.4S	179.9W	6.0	551	81.9	234.8	235
Feb. 1, 1973	0514:20	22.7S	62.2W	6.1	229	77.6	128.4	128*
Dec. 28, 1973	0531:06	23.9S	180.0E	6.3	549	82.3	234.5	235*
March 23, 1974	1428:35	23.9S	179.8E	6.1	535	82.5	234.6	235*
Oct. 20, 1974	0412:29	17.9S	178.6W	6.0	602	77.4	238.1	235
Nov. 29, 1974	2205:22	30.7N	138.3E	6.1	419	83.3	302.5	315*
Feb. 22, 1975	2204:37	24.9S	179.1W	6.2	375	82.4	233.7	235
June 29, 1975	1037:41	38.8N	130.0E	6.2	560	83.9	313.2	315
Jan. 23, 1976	0545:30	7.5S	119.9E	6.4	614	120.0	282.4	235
Dec. 12, 1976	0108:50	28.0N	139.6E	5.9	491	83.9	299.7	315
Sept. 23, 1978	1644:26	11.0S	167.2E	6.5	200	85.4	249.9	235
April 24, 1979	0156:14	20.8S	178.7W	6.0	450	79.4	236.0	235
May 13, 1979	0638:15	18.9N	145.3E	5.9	250	84.8	289.2	315
May 21, 1979	2232:58	15.2S	70.1W	6.0	208	67.1	128.8	128
June 27, 1979	0958:03	7.1N	82.0W	5.8	150	42.9	120.6	128
Aug. 16, 1979	2142:44	41.8N	130.7E	6.1	588	81.5	315.2	315
Nov. 23, 1979	2349:04	4.8N	76.2W	6.4	200	48.6	117.4	128
Dec. 11, 1980	1826:26	21.3S	68.1W	6.1	100	72.9	131.6	128

*Used in coda analysis.

Also shown are *PKIKP* wave forms of the January 23, 1976, event which was used in *Hadley and Kanamori's* [1977] study. This phase will be used as a constraint on structure under the station. Note that, in all cases, the magnitude of tangential motions excited by the *P* wave is comparable to radial motions. In a radially stratified earth, *P* and resulting *P-SV* conversions would be restricted to the sagittal plane containing the ray. Note also that tangential and radial motions differ quite substantially in wave form, suggesting that simple instrument miscalibration or magnification differences cannot give rise to these anomalous particle motions (see the appendix).

The *PKIKP* phase for the January 23, 1976, event also shows very anomalous particle motions. This phase is incident below the crust at an incident angle of about 4°. Horizontal motions, however, are not small as expected. They are about half the size of the vertical *P* wave, and both components are grossly different. Furthermore, this event has a back azimuth in which the observed E-W component is almost perfectly radial, and the observed N-S component, tangential. The data of Figure 2 strongly suggest that heterogeneous three-dimensional structure is causing large scattering effects in the receiver function data.

Because of the location of teleseismic source zones, the equalized radial and tangential component data were grouped into three back azimuth groups and stacked (see Table 1 for groupings). The stacking was done by shifting all traces to a common time based on the *P* first arrival and then adding them. Wave forms for one standard deviation about the mean at each sample point were also computed. The resulting wave form stacks are shown in Figure 3 with their standard deviations. A comparison of stacks from the three back azimuth groups are shown in Figure 4. Displays of this type yield information on the coherency of arrivals within the wave form and of the level of processing noise [Owens, 1984].

Only the first 15 s of the wave forms are shown in Figure 3. The data of Figure 2 show major arrivals in the horizontal wave forms for at least 60 s. This poses a dilemma for velocity models that can be considered, since it is difficult to get such arrivals from plausible plane layered models. This problem

will be addressed in a later section; here I concentrate on major initial arrivals.

Figure 3a shows the wave form stacks for events from a back azimuth of 128°. The bounding envelope for one standard deviation is large for tangential motions and for arrivals after direct *P* on the radial component. A phase marked "*Ps*" on the radial stack is also observed on the radial data of the other back azimuth groups.

The other two back azimuth groups (Figures 3b and 3c) show remarkably large arrivals. The *Ps* conversion is roughly half the size of direct *P* on the radial components and is also large on the tangential components. Note that the tangential components show that the direct *P* wave amplitude is variable within the noise of measurement. There are indications of later, coherent arrivals in the wave forms, but these are problematical.

Figure 4 shows the stacks displayed together with *P* and *Ps* phases annotated. My working hypothesis is that this secondary phase is a direct *P*-to-*SV* conversion beneath the station. Its large size, relative to direct *P*, on all except the 128° tangential stack is remarkable and can be directly seen in the data of Figure 2 (also see the appendix). Figure 5 shows particle motion plots of the radial and tangential stacks for 315° and 235° back azimuths. Note that the direct *P* wave conforms to nearly radial motions as expected for ideal *P* particle motion but that the *Ps* conversion has been rotated 45° or more out of the sagittal plane. It is very difficult to produce such *Ps* arrivals from simple dipping interfaces that dip only a few degrees or have velocity contrasts typical of continental crustal models [Langston, 1977; Lee, 1983]. The implication is that there is a major discontinuity under PAS which has high dip and/or high *S* wave velocity contrast.

These arrivals are also evident in long-period data. Figure 6 compares observed wave forms for the November 29, 1974, event recorded on the Benioff 1-90 and Press-Ewing 30-90 systems at PAS. The data have been shifted to a common time base. The vertical components, although showing some scattered waves in the coda, are pulselike and show one major *P* arrival. The N-S 1-90 component is dominated by the *Ps* con-

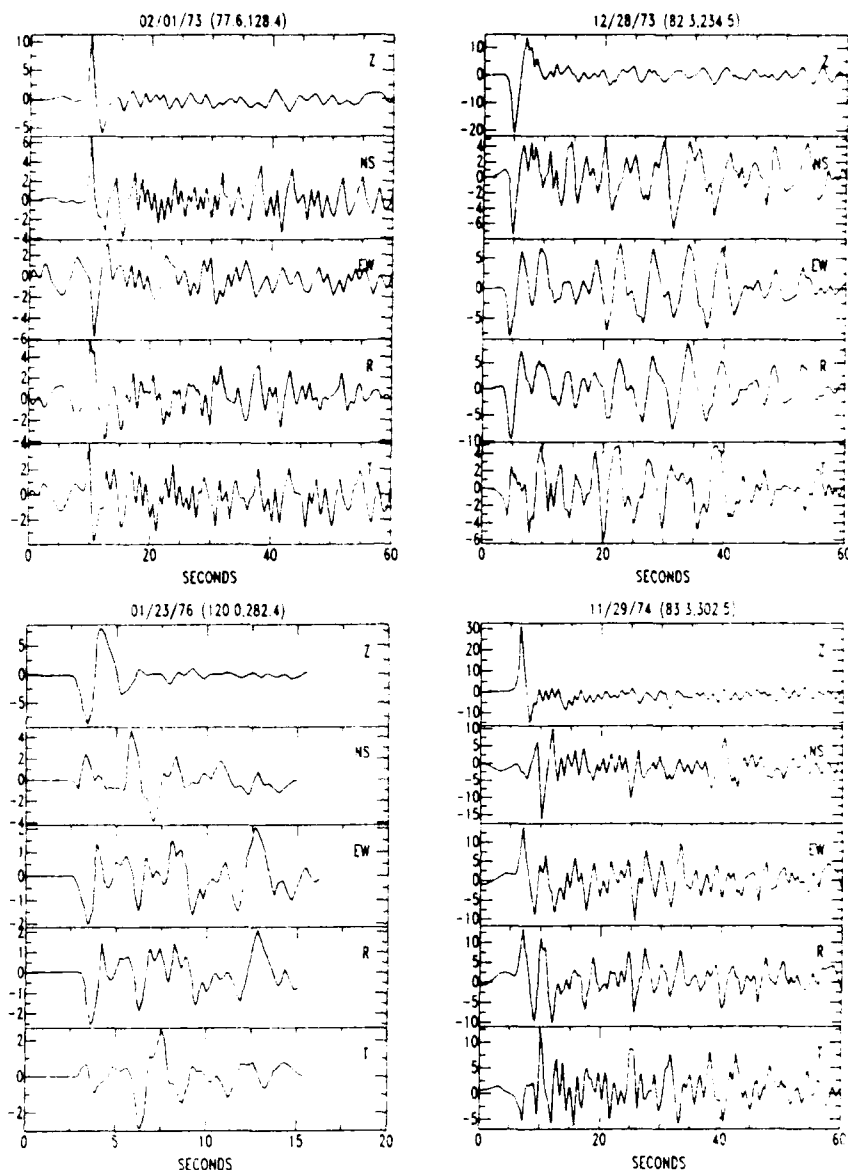


Fig. 2. Selected data from deep earthquakes (see Table 1) recorded on Benioff 1-90 instrumentation. Z, N-S, and E-W wave forms denote observed vertical, north-south, and east-west components. R and T wave forms are the result of rotating the observed horizontal components into the theoretical back azimuth of the ray. The distance and back azimuth angle are given, in order, in the parentheses to the right of each event's date. Note the time scale difference for the January 23, 1976, event.

version, and direct *P* is a minor initial arrival. The 30-90 N-S record shows that the *P_s* conversion (arrow) also dominates the long-period wave form. The *P_s* conversion is present on the E-W components, but direct *P*, the first pulse, is larger. The *P_s* conversion is evident, having the effect of broadening the initial pulse by a factor of 2 compared to the vertical long-period *P* wave, producing a shoulder on this pulse. This comparison of data recorded on two different seismometer systems demonstrates that the crustal structure responsible for these scattering effects is large and that the effect is not an artifact of instrument miscalibration.

Langston [1977, 1979] suggests that the amplitude and polarity behavior with azimuth of tangential *P_s* can constrain the direction and magnitude of interface dip. Unfortunately,

this phase is only well developed in the 235° and 315° azimuth groups, although it may be significant that it is poorly developed in the 128° azimuth group. The *PKIKP* phase from the January 23, 1976, event, however, offers some independent information in this regard.

Since this phase propagates nearly vertically, any *P_s* conversion from a dipping interface will be contained in the plane of the ray and dip direction. Thus a simple plot of particle motion of the *P_s* conversion will be a direct measurement of the dip direction (Figure 7). The *P_s* conversion is the largest arrival on the N-S component and is easily seen in the particle motion plot. Note that it is polarized almost perfectly northward. Because *P_s* is the same polarity as direct radial *P* (Figure 4), it is due to conversion at the boundary between

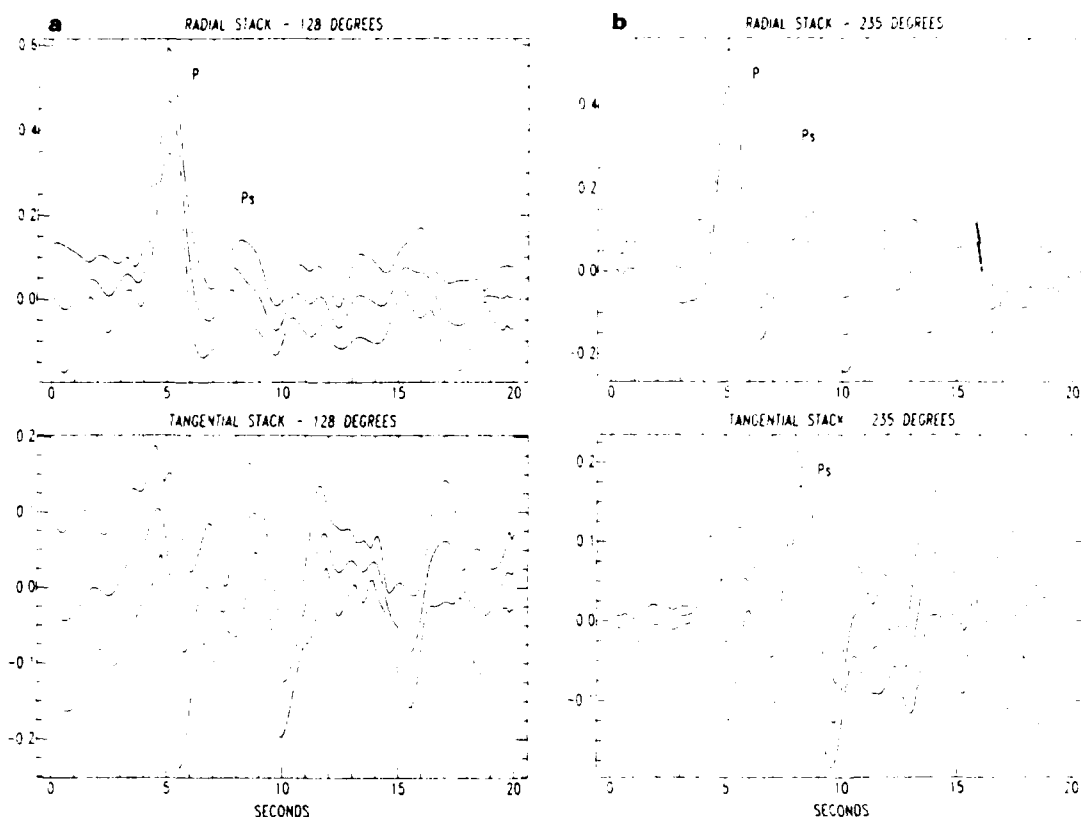


Fig. 3. Stacks of source-equalized radial (top) and tangential (bottom) data for the three azimuthal groups considered in the text. The average and ± 1 standard deviation wave forms are shown in each panel. *P* and *Ps* arrivals are annotated. (a) 128° group. (b) 235° group. (c) 315° group.

deeper high velocity material under shallower lower velocity material. Taking the negative polarity of the *PKIKP* phase into account yields a northward dip direction for the postulated interface. This is consistent with the tangential *Ps* polarities displayed by the 235° and 315° stacks.

DETERMINISTIC MODELING OF THE *Ps* CONVERSION

Recent efforts in modeling receiver function data have concentrated on formal inversion of the data to obtain plane-layered crustal and upper mantle models [e.g., Owens *et al.*, 1987]. Characteristics of the Pasadena data set preclude this approach. The duration and amplitude of the horizontal component coda and large tangential amplitudes all argue against finding reasonable plane layered models. Figure 8 shows a comparison of observed and synthetic radial component wave forms. The radial stack for 235° azimuth is shown below a synthetic radial seismogram computed for a crustal model proposed for the area by Hadley and Kanamori [1977]. The Thompson-Haskell method was used to construct the synthetic [Haskell, 1962]. The crustal model is shown in Figure 9 with parameters tabulated in Table 2. The Moho occurs at 31 km depth and produces a moderately large *Ps* conversion which arrives 4 s after direct *P* (shown by arrow in Figure 8). The observed *Ps* conversion is larger and arrives at least 1 s earlier, suggesting several other models.

First, if the *Ps* conversion is from the Moho, then the crust must be at most 27 km thick if Hadley and Kanamori's velocities are assumed. However, Hearn and Clayton's [1986a] study using *P₄* waves suggested average crustal *P* wave velocities in

the area of about 6.3 km/s and a crustal thickness of about 31 km. It is possible that the receiver function data are sampling a local anomaly unresolved by Hearn and Clayton's data. Alternatively, if the crust is 31 km thick, then the average *S* wave velocity in the crust must be at least 4 km/s. The corresponding *P* wave velocity would be high at 6.9 km/s, assuming Poisson ratios near 0.25 appropriate for crustal rocks. In either the case of a slow thin crust or a thicker high-velocity crust there should be an anomalous mass excess in the crust and upper mantle column which would show up in the gravity field. No such anomaly is observed [Hadley and Kanamori, 1977].

One simple solution to this problem is to accept the thickness and crustal velocities from previous studies and to infer that a midcrustal interface causes the large *Ps* conversion. A plane layered model which shows this hypothesis is plotted in Figure 9 (and Table 2) with the corresponding radial synthetic seismogram in Figure 8. *Ps* arrivals from the Moho are minimized by making the structure approximate a smooth gradient in that region. The large *Ps* amplitudes observed require a high *S* wave velocity contrast. This, in turn, implies a velocity inversion in the midcrust. The synthetic seismogram shown in Figure 8 for this kind of low-velocity zone (LVZ) structure approximates the arrival time and the double-peak character of the actual data.

Obviously, the plane layered model does not explain the anomalous particle motion of the *Ps* conversion. A series of ray theory calculations were performed to test the dipping interface model [Langston, 1977]. The tangential *Ps* data re-

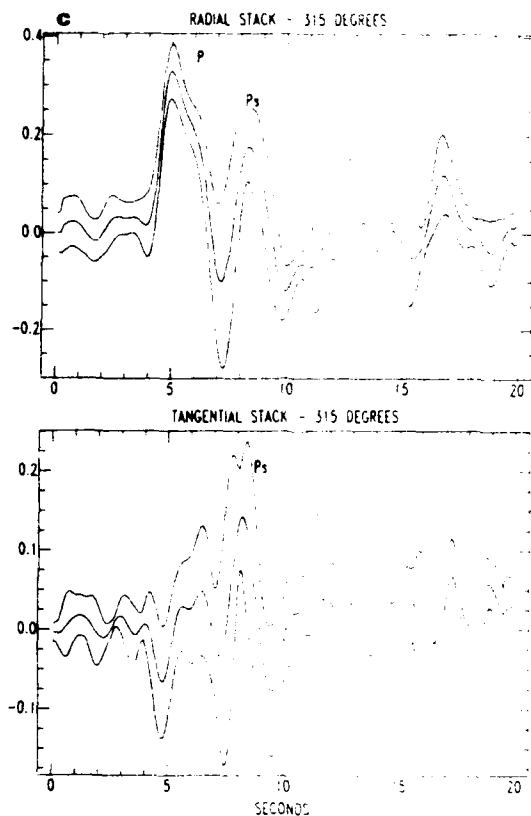


Fig. 3. (continued)

quire that the interface dip northward under the San Gabriel Mountains. Experience with such calculations indicates that there can be considerable trade-off between interface dip and velocity contrast [e.g., Langston, 1979]. Waves which approach a dipping interface from the down-dip direction will have an effective angle of incidence which is larger than waves approaching a horizontal interface. This will produce a larger conversion. Waves approaching from the updip direction will tend to have lower angles of incidence with less conversion.

A number of dipping interface models based on the Hadley and Kanamori crustal model of Table 2 were examined. The top of the 6.8 km/s layer was allowed to dip up to 40°. Two rays were traced through the model. These were direct *P* and the *P_s* conversion from the dipping interface. It was quickly seen that, although it may be possible to produce large *P_s* conversions for rays which approach the structure from the down-dip direction, models with dips greater than 10° consistently produced low-amplitude *P_s* conversions for rays traveling from the updip direction. Indeed, for *P* velocity contrasts of 6.2–6.8 km/s and 5.0–6.8 km/s (assuming a Poisson solid), dips of 30° resulted in *P_s* conversions which had opposite polarities relative to direct radial *P*, inconsistent with the data (Figure 4). Thus interface dip should be of the order of 10° or less. The *S* wave velocity contrast should also be greater than 1 km/s. The calculated *P_s*/*P* ratio for updip ray incidence is 0.19 for the 5.0–6.8 km/s interface with 10° dip. The observed *P_s*/*P* ratio for the 315° stack is 0.57 (Figure 4), which represent waves coming updip but at an angle from the northward dip direction. Calculated tangential amplitudes for the *P_s* conversion are comparable to the radial amplitudes and agree with the 45° polarization anomaly seen in the data.

STOCHASTIC STRUCTURE MODELING

Up to this point the data have been treated from a deterministic point of view. The data show that the first *P_s* conversion is indeed a major wave propagation effect, and it is reasonable to assume that other early arrivals will be due to direct interactions with discontinuities in the structure. However, the *P_s* conversion is simply the first of many large arrivals in the horizontal *P* wave coda. Are these later arrivals fundamentally different from early arrivals? What do these large arrivals imply about the heterogeneity of the structure under the station? In particular, since there is recent emphasis on modeling such data with formal inversion methods, can plane layered structure mimic the coda seen in the data and, if so, what are the implications?

First, I make the assumption that all arrivals seen after direct *P* in the data represent waves scattered in structure near the receiver. This assumption is probably poor for shallow earthquake sources simply because of known propagation effects like near-source surface reflections. Deep events, however, should be less affected by near-source scattering.

For deep teleseisms, tangential amplitudes in the coda are as large or larger than the vertical coda. Therefore if these coda waves are due to scattering (*P* to *P* or *S* to *P*) in structure near the source they must finally convert to *P* waves to arrive soon after the direct *P* at the receiver. If they are *P* waves, they must have azimuth anomalies greater than 45° since they are so large on the tangential component. This contradicts the near-source scattering hypothesis since the

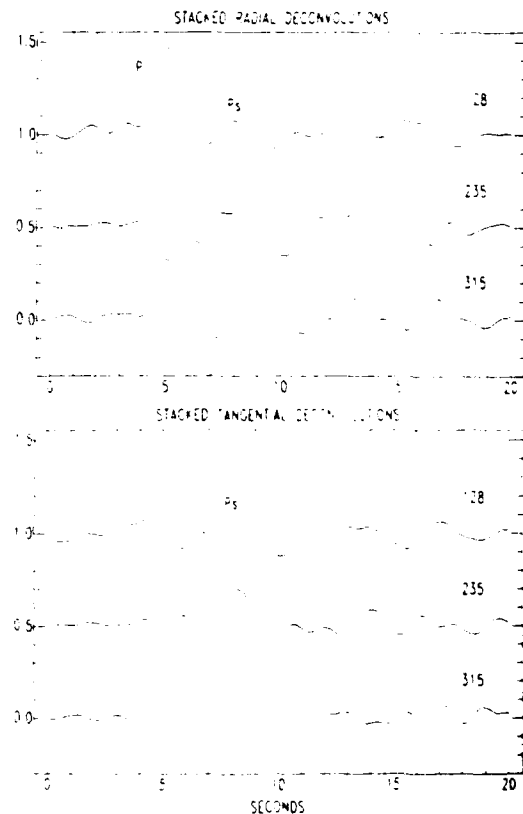


Fig. 4. Comparison of the stacked radial and tangential equalized wave forms for the three back azimuth groups. Note the azimuthal dependence of the *P_s* conversion on the radial components. The wave forms have been shifted in baseline for viewing purposes.

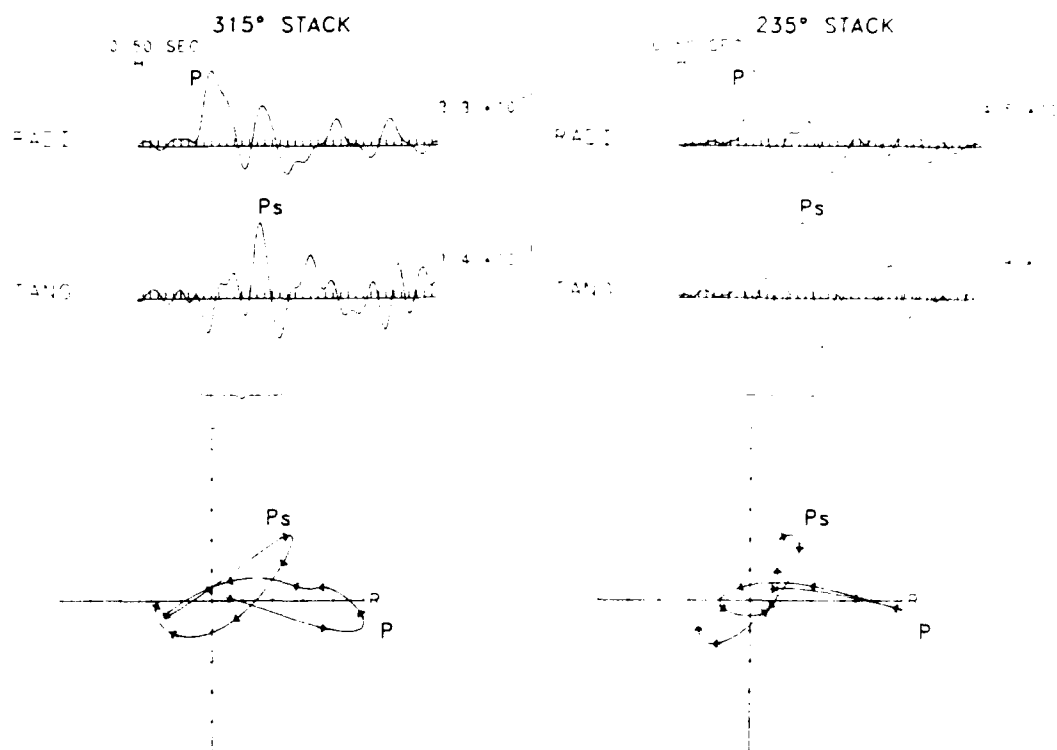


Fig. 5. Particle motion plots for the 315° and 235° equalized wave forms. The wave form data are displayed above the radial (R or RADI), tangential (T or TANG) particle motions. Arrows are shown on the particle motion plots every 0.5 s. Wave form data included within the brackets are plotted below. Maximum amplitude for each wave form is shown to right of the wave form. Note that the P waves in both cases are polarized in the expected ray direction but the inferred P_s conversions have a polarization anomaly of 45°.

scattered waves themselves must originate at teleseismic distances from the source. The conclusion is that large horizontal coda amplitudes relative to horizontal P must be due to scattering near the receiver (see also Cessaro and Butler [1987]).

Synthetic seismograms were computed for a series of receiver models with plane layered stochastic structure. The procedure used by Frankel and Clayton [1986] was adopted to generate a random velocity-depth function. A random series of

normally distributed velocity values $v(z)$ with zero mean and unit variance was generated from a pseudo random number generator. A 0.25 km sampling interval was assumed for a layer of thickness 30 or 60 km. The velocity function was Fourier-transformed to the wave number domain to obtain $v(k)$. An exponential correlation function $N(z) = e^{-z/a}$ was assumed for the medium where a is the correlation length. The wave number spectrum of $N(z)$, $\tilde{N}(k) = 2a/(1 + k^2a^2)$, was then

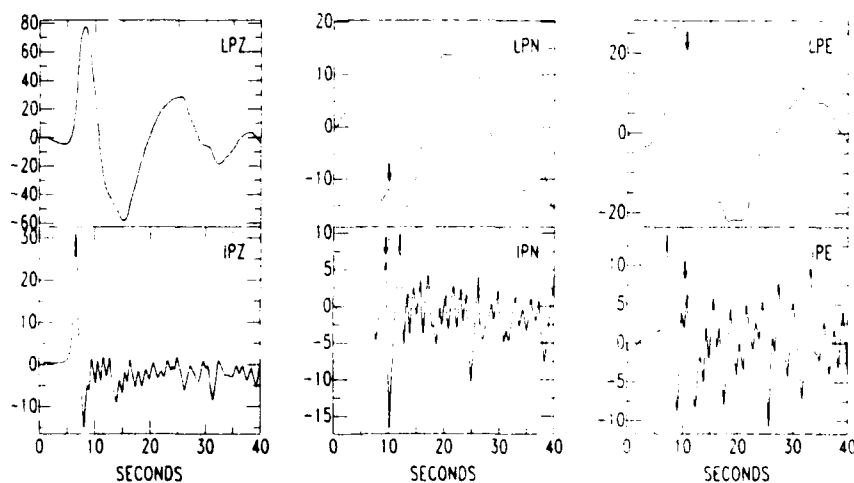


Fig. 6. Comparison of data from the November 29, 1974, event recorded on 30-90 (long period) (top) and 1-90 (intermediate period) (bottom) instrumentation at PAS. The arrows show the location of the P_s conversion discussed in the text for both data sets. Note particularly the extreme amplitude of the P_s conversion relative to the first P arrival on both IPN and LPN components.

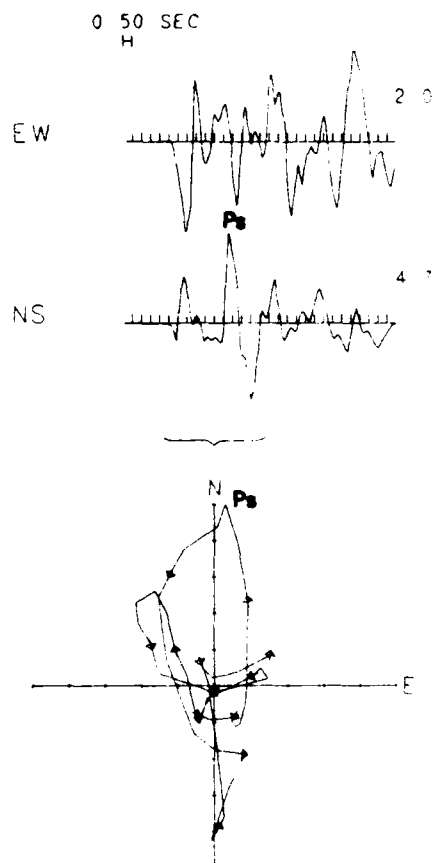


Fig. 7. Particle motion plot of the horizontal data for the January 23, 1976, event. Data included within the bracket are plotted below with arrows occurring every 0.5 s. The P_s conversion is polarized almost perfectly northward and indicates the direction of dip of the causative interface.

used to filter $u(z)$. The filtered velocity spectrum was inverse-transformed and scaled to a selected velocity variance and mean. Synthetic seismograms were computed using the Thompson-Haskell method [Haskell, 1962].

Calculations were performed with a Gaussian correlation function as well, but the exponential correlation function proved to create more scattered arrivals since its spectrum is richer in higher wave numbers. A correlation length a of 1 km was assumed. For 0.5-Hz waves considered in this study, the corresponding value of $k_z a$ is approximately equal to 1, where k_z is the vertical component of the wave number. S wave velocities were derived by assuming a Poisson solid, and density was held constant. Velocity parameters for the half-space below the random crustal layer were generally set to those of the lowermost crustal layer.

Two basic velocity models were considered in the one-dimensional simulations. The first consisted of a heterogeneous crustal layer 30 km thick with a mean velocity of 5.5 km/s and velocity standard deviation of 10%. The top pair of wave forms in Figure 10 are typical examples of the free surface displacements computed from a number of realizations of the stochastic parameters. Figure 9 shows the corresponding velocity-depth functions for the lower and upper pair of synthetics. The incident wave time function assumed was the time derivative of the Gaussian function discussed above in the

source equalization section. A quick glance at these synthetics and the data of Figure 2 show that synthetic coda levels are significantly lower than those observed and that the coda attenuates quickly with time.

It might be expected that a Moho with a large velocity contrast would trap more scattered energy in the crustal layer. The middle pair of synthetics shows this case for the model used to compute the upper synthetics but assuming a half-space P wave velocity of 8 km/s. Minor changes occur in the resulting synthetics. The largest change is to accentuate the Moho P_s conversion by about a factor of 2 (arrow). The coda is largely unaffected.

Increasing layer thickness tends to increase the duration of coda. Increasing the velocity standard deviation to 20% over a layer 60 km thick with a mean velocity of 6 km/s produces synthetic seismograms which start to mimic the data (bottom, Figure 10). Large P_s conversions and reverberations start to attain amplitudes comparable to the direct radial P wave, and coda duration superficially appears to agree with the observed data.

Thus it appears that one-dimensional velocity variations in excess of 20% over a significant thickness of the lithosphere are needed to match the receiver data at PAS. This would suggest that a series of layers which vary in velocity from about 8.4 to 3.6 km/s from the surface into the mantle over a scale of about 1 km are present, which is geologically unreasonable.

Alternatively, it is possible that there is significant body wave to surface wave scattering in near-surface layers [Dainty et al., 1974; Aki and Chouet, 1975; Dainty and Toksoz, 1977]. This might be expected on the basis of the heterogeneous geology alone. It is also clear that two- and three-dimensional structures are required in the area to produce the large tangential particle motions observed in the data. Numerical experiments with two-dimensional elastic finite difference methods show that, for an equal amplitude scattered field, velocity variations in two dimensions are about half that needed for velocity variations in one dimension [McLaughlin et al., 1985].

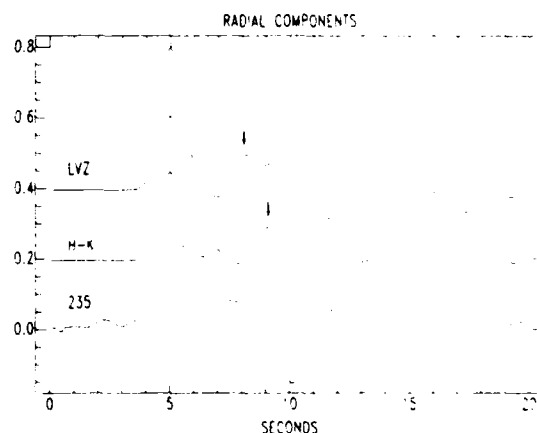


Fig. 8. Comparison of synthetic radial wave forms for the two models of Table 2 with the 235 radial wave form stack. The arrow for the H-K (Hadley-Kanamori model) wave form shows the location of the P_s conversion from the Moho. The arrow for the LVZ (low velocity zone model) wave form shows the location of the P_s conversion produced at the base of the crustal low-velocity zone. The base-lines of the synthetic wave forms have been shifted for viewing purposes.

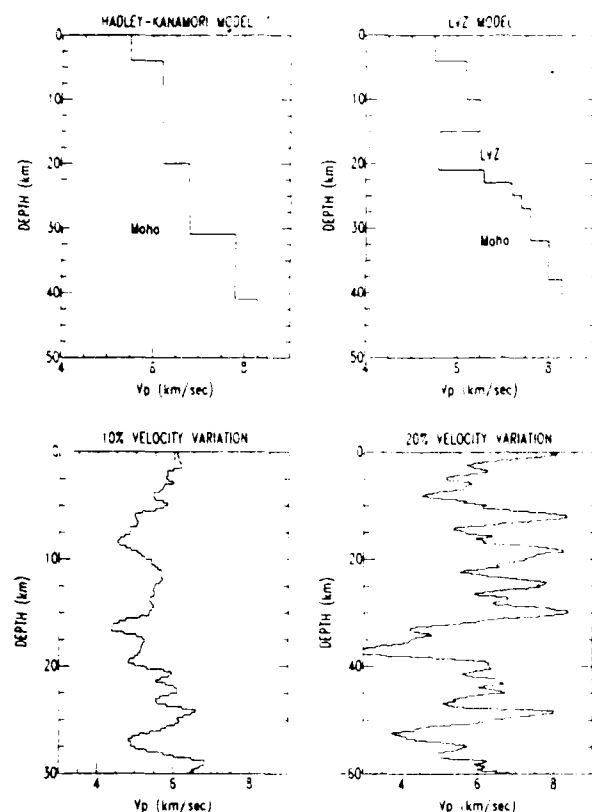


Fig. 9. Velocity depth functions for the Hadley-Kanamori model and the LVZ model used in constructing the synthetic seismograms of Figure 8. Also shown are the stochastic one-dimensional models used in the calculation of the synthetics displayed in Figure 10. Note that velocity and depth scales are different among the plots.

ENERGY FLUX MODELS FOR PLANE WAVE SCATTERING

Teleseismic *P* wave coda has been the subject of a number of studies [e.g., Aki, 1973; Dainty and Toksoz, 1977; McLaughlin et al., 1985; Levander and Hill, 1985; Frankel and Clayton, 1986; Cessaro and Butler, 1987]. These studies are closely related to general problems in coda generation due to lithospheric structure in local and regional data sets [e.g., Aki, 1969, 1980; Aki and Chouet, 1975; Dainty and Toksoz, 1977; Gao et al., 1983; Richards and Menke, 1983; Gupta and Blandford, 1983; Wu and Aki, 1985a, b; Cessaro and Butler, 1987; Frankel and Wennerberg, 1987; Vidale and Helmberger, 1988].

A number of techniques are available to parameterize the coda level and time decay based on the Born approximation of weak single scattering or of diffusion of coda energy for extreme scattering [e.g., Aki and Chouet, 1975; Aki, 1980; Dainty et al., 1974]. Recent work has concentrated on simulation studies using finite difference acoustic and elastic wave propagation methods [Levander and Hill, 1985; Frankel and Clayton, 1986] which implicitly include the entire scattered field. Levander and Hill [1985] examined scattering characteristics of a rough boundary between a surface layer and underlying half-space and showed that much of the scattered field is dominated by Rayleigh wave propagation. Frankel and Clayton [1986] and McLaughlin et al. [1985] examined *P*-SV propagation in two-dimensional random media to examine scattering of high-frequency ($f > 1$ Hz) seismic waves. Subse-

quently, Frankel and Wennerberg [1987] developed a simple theory based on previous finite difference simulations to parameterize coda levels, scattering attenuation, and intrinsic attenuation for two- and three-dimensional scalar wave fields.

The success of a number of receiver function studies in determining plane-layered crustal and upper mantle structure indicates that the scattered wave field may be thought of being composed of a "coherent" contribution from *Ps* conversions and reverberations from discrete interfaces and a "stochastic" contribution from smaller-scale heterogeneities. The coherent field can be seen over a large solid angle of ray paths. The stochastic field changes quickly with ray parameter and ray azimuth. Examples of the stochastic field are variation in tangential *P* wave first motions over the events of the 235 stack in Figure 3b as well as coda arrivals with long lapse times from the first arrival. The success of any deterministic receiver function study depends critically on the coherent field being dominant. However, the incoherent field, which is usually ignored in such studies, also contains statistical information on the degree of heterogeneity in the structure which may be very useful.

A heuristic approach will be used here to develop an operational theory appropriate to the three-component receiver data. The purpose of doing this is to empirically compare coda levels and decay between different receivers for classification purposes and to suggest avenues of research that will address the actual wave propagation problems. This heuristic approach will also be used to quantify the differences between one-dimensional structure coda development and coda observed in the data.

A useful method of parameterizing the *P* coda can be derived following Frankel and Wennerberg [1987]. They examined scalar two-dimensional finite difference simulations and suggested that scattered energy behind a cylindrical or spherical wave front distributes itself uniformly over the volume behind the wave front. Aki and Chouet [1975] arrived at the same conclusion when examining coda of regional earthquakes. This simple assumption yielded useful formulae for coda level and decay in cases of strong multiple scattering as well as the limiting case of weak single scattering.

Consider first a source of plane waves which radiates two oppositely propagating plane waves in a scattering whole

TABLE 2. Plane-Layered Crustal Models

Layer	V_p , km/s	V_s , km/s	Density, g/cm ³	Thickness, km
<i>Hadley and Kanamori Model</i>				
1	5.5	3.0	2.6	4.0
2	6.2	3.5	2.7	16.0
3	6.8	3.8	2.85	11.0
4	7.8	4.5	3.1	10.0
5	8.3	4.8	3.35	...
<i>Low-Velocity Zone Model</i>				
1	5.5	3.0	2.6	4.
2	6.2	3.5	2.7	6.
3	6.5	3.75	2.7	5.
4	5.6	3.23	2.7	6.
5	6.6	3.81	2.8	2.
6	7.2	4.16	2.9	2.
7	7.4	4.27	2.95	2.
8	7.6	4.30	3.0	5.
9	8.0	4.62	3.2	6.
10	8.3	4.8	3.35	...

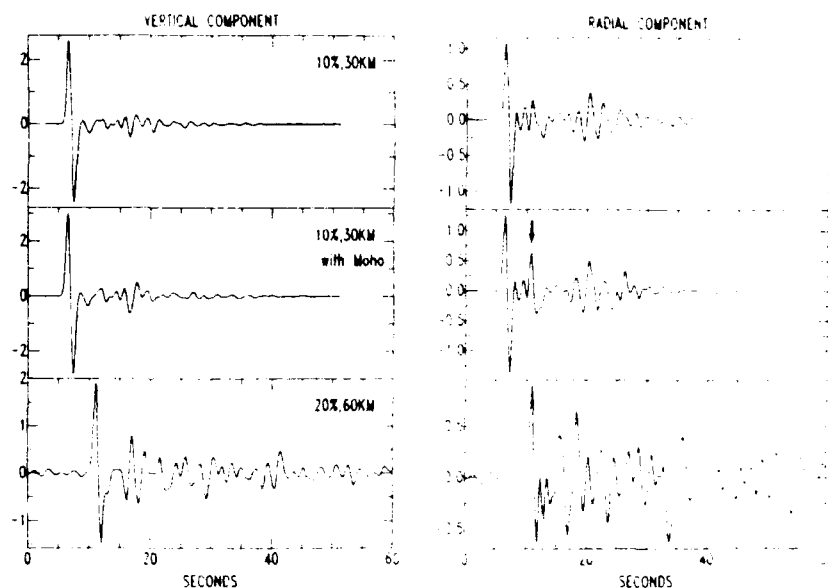


Fig. 10. Typical plane wave synthetic seismograms computed for three realizations of one-dimensional stochastic velocity structure. Vertical and radial displacement components are shown. The top traces are for a model containing a layer 30 km thick with an average velocity of 5.5 km/s and a standard deviation 10% of the average. The center pair of synthetics are for the same crustal model as the top pair but with the addition of a high velocity (8.0 km/s) half-space. The arrow points to the Moho P_s conversion on the radial component. The lower pair of synthetics were computed using a layer thickness of 69 km, average velocity of 6 km/s, and velocity standard deviation of 20%. P_s conversions and reverberations start to attain amplitudes seen in the PAS data.

space. The total instantaneous energy or power E_T is given by the sum of the direct wave power E_D and the coda power E_C :

$$E_T = E_D + E_C \quad (1)$$

Specify that

$$E_D = E_T e^{-\omega t Q} \quad (2)$$

where t is time, ω is circular frequency, and Q is the quality factor for attenuation due to wave scattering. Substitution of (2) into (1) gives

$$E_C = E_T (1 - e^{-\omega t Q}) \quad (3)$$

Coda amplitude A_c is related to the coda power density ξ_c through the principal assumption that the coda energy distributes itself uniformly behind the two propagating plane waves. First, we have

$$A_c = d(\xi_c)^{1/2} \quad (4)$$

where d is a scaling factor. For P and S plane waves $d = \rho^{-1/2}$ where ρ is density. If δS is the unit plane wave area, r the propagation distance from source to receiver, and α P wave velocity, then the coda power density is

$$\xi_c = \frac{E_c}{V} = \frac{E_c}{2r\delta S} = \frac{E_c}{2\alpha t\delta S} \quad (5)$$

where V is volume. Using (3), (4), and (5) we obtain

$$A_c = \frac{d(E_T)^{1/2} (1 - e^{-\omega t Q})^{1/2}}{(2\alpha t)^{1/2} (\delta S)^{1/2}} \quad (6)$$

E_T can be estimated using the observed direct wave amplitude and correcting it for attenuation through the scattering medium. Thus

$$E_T = 2E_D e^{+\omega t Q} \quad (7)$$

where E_D is the observed direct wave power and $t_0 = r/\alpha$. The factor of 2 comes from the fact that two plane waves are propagating in the medium and contribute to the scattered field. Plane wave propagation theory is used to obtain the estimate of direct wave power. First, consider the integral of the square of the ground velocity $4(t)$

$$I_D = \int_{t_1}^{t_2} 4^2(t) dt \quad (8)$$

Times t_1 and t_2 bound the direct wave arrival and are estimated from the data. The direct wave power is therefore

$$d^2 E_D = \alpha I_D \delta S \quad (9)$$

Substitution of (9) into (7) and of (7) into (6) gives

$$A_c = (I_D)^{1/2} t^{1/2} e^{+\omega t Q/4} (1 - e^{-\omega t Q})^{1/2} \quad (10)$$

As Frankel and Wennerberg [1987] show, the effect of attenuation due to scattering determines the initial level of the coda scattered from the direct wave, but coda decay with time is mainly controlled by the time-dependent increase in volume behind the wave front. In this plane wave case the $t^{1/2}$ dependence is due to the linearly increasing volume between the two oppositely propagating plane waves.

Relation (1) is useful for describing the coda for a plane wave propagating in a thick layer where coda lapse times (wave arrive time relative to the direct wave) are less than the arrival time of waves which interact with the lower boundary of the layer, assuming the observation point is at the surface. This corresponds to lapse times of less than 5 s for receivers on typical continental crust. A more appropriate model for receiver function coda is scattering in a heterogeneous layer overlying a homogeneous, isotropic half-space. In this situation a vertically propagating plane wave sweeps through the layer once on its way to the receiver, reflects from the free

surface, and sweeps through yet another time on its way back to the half-space. Energy is scattered from the plane wave into coda energy.

A variation of this problem was studied by Dainty *et al.* [1974] and Dainty and Toksoz [1977], where they assumed that scattering in the layer followed solutions to the diffusion equation. Also, assuming that all energy within the layer was scattered energy, they obtained the following analytic solution for the scattered energy field at the free surface $m(t)$ (assuming no intrinsic attenuation):

$$m(t) = \frac{4}{h} \sum_{n=1}^{\infty} \frac{a_n \cos a_n}{2a_n + \sin 2a_n} \exp\left(-\frac{t\xi_n a_n^2}{4h^2}\right) \quad (11)$$

where h is layer thickness and ξ_n is the vertical diffusivity of energy through the boundary of the layer into the half-space. The coefficients a_n are found as solutions of the following equation:

$$a_n \tan a_n = 4hv/\xi_n \quad (12)$$

where v is the seismic velocity of the half-space.

The dominant term of (11) for long lapse times and a high vertical diffusion rate can be shown to be for $n = 1$. Thus for cases where diffusion of scattered energy occurs quickly, coda energy decays like

$$m(t) \propto e^{-\gamma t} \quad (13)$$

where $\gamma = \xi_1 a_1^2 / 4h^2$. This behavior can be incorporated into a hybrid model containing aspects of plane wave propagation in a layer with assumption of homogeneity of the scattered field within the layer.

Consider a horizontal scattering layer of thickness h overlying a homogeneous and isotropic half-space. A vertically propagating plane wave is incident from below, passes through the layer, reflects from the free surface, and passes back through the layer into the half-space. The total power in the system can be written as

$$E_T = E_D + E_C + E_0 \quad (14)$$

where a new term E_0 has been introduced to describe the amount of instantaneous energy which diffuses out the bottom of the layer at the expense of the coda instantaneous energy E_C . On the basis of the behavior of (11) above I assume that

$$dE_0/dt = \gamma E_C \quad (15)$$

which by simple integration yields

$$E_0 = E_C(e^{\gamma t} - 1) \quad (16)$$

where it is specified that $E_0 = 0$ at $t = 0$. As before, the power in the direct wave after interacting with the layer is

$$E_D = E_T e^{-\omega 2t\epsilon Q_1} \quad (17)$$

where the factor of 2 in the exponent comes from the wave passing twice through the layer. Obviously, (14) is appropriate for short-duration direct waves and times greater than $2t_d$.

Substituting (17) and (16) into (14) gives

$$E_C = E_T(1 - e^{-\omega 2t\epsilon Q_1})e^{-\gamma t} \quad (18)$$

Also, recognizing that the volume swept by the plane wave is now $h \delta S$, the coda power density becomes

$$\xi_C = E_C \pi t_d \delta S \quad (19)$$

As before, the total instantaneous energy available to the system can be estimated from the observed direct wave power E_D by

$$E_T = E_D e^{+\omega t\epsilon Q_1} \quad (20)$$

and using (9) gives

$$A_C = (I_D^{-1/2} t_d^{-1/2}) e^{+\omega t\epsilon 2Q_1} (1 - e^{-\omega 2t\epsilon Q_1})^{1/2} e^{-\gamma t/2} \quad (21)$$

Note that this form for coda amplitude looks superficially the same as that in (10) except for the exponential factor of time in the numerator of (21). Indeed, the time decay of the coda is controlled entirely by this factor. If $\gamma = 0$ is assumed so that no coda energy can diffuse out of the layer, then the coda level is constant for all time, consistent with the plane wave assumption of a packet of energy being homogeneously dispersed throughout the layer. Thus the decay of the coda field is functionally equivalent to the leading term for the formal solution of (11) and (13), particularly considering that energy is proportional to the square of amplitude.

Anelastic attenuation can be included in relations (10) and (21) as the factor

$$e^{+\omega t\epsilon 2Q_1} e^{-\omega t\epsilon 2Q_1}$$

where Q_1 is the intrinsic attenuation of the medium. The first exponential in this factor is the correction factor to determine total energy from the direct wave and the second exponential gives the attenuation of coda amplitude. Note that the effect of coda energy diffusing out of the layer given in (21) is exactly the same as intrinsic attenuation. It would be expected that it would be very difficult or impossible to separate the two effects in practice using the teleseismic coda data.

An implicit assumption in developing (10) or (21) is that the scattered field is of the same wave type as the primary. These equations are appropriate for, say, the scattered pressure field from an incident P wave. Even for simple one-dimensional layered structures, much of the scattered field is composed of P -to- S conversions. For two- and three-dimensional structures there is evidence that much of the scattered field seen at the surface is composed of low group velocity surface waves [Dainty *et al.*, 1974; Aki and Chouet, 1975; Levander and Hill, 1985]. Thus there is a procedural problem of relating observed coda wave amplitude to energy since the wave type contained in the coda must be known beforehand. In principle, it is possible to directly infer the energy contained in a wave field if strain observations are available. However, three-component displacement data cannot be used without assumptions on wave type.

Recognizing these limitations, equations (10) and (21) are used as guides to the analysis of the three-component data. These equations will be useful in parameterizing relative levels of coda and coda decay between isolated receivers but are clearly deficient in addressing all of the scattering mechanisms which are probably important in teleseismic coda development.

Some operational aspects of examining coda decay are patterned after previous studies [e.g., Richards and Menke, 1983; Frankel and Wennerberg, 1987]. Observed three-component data for a single event are first narrow-band-pass-filtered with a Butterworth recursive filter in the forward and backward directions. The two-pole filter used had corner frequencies of 0.25 and 1 Hz so the following results are appropriate for 0.5 Hz waves. Once the data were filtered the intensity of the direct P wave at 0.5 Hz was estimated by squaring the signal.

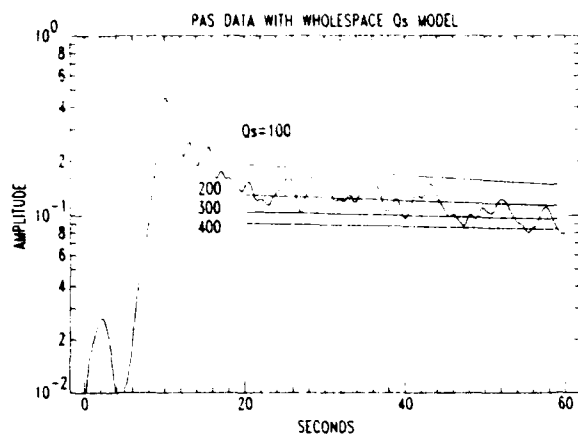


Fig. 11. Envelope stack of the three-component data of four earthquakes (see Table 1) recorded at PAS. The envelope is shifted 10 s for display purposes. Lines show predicted coda levels for assumption of scattering Q_s of 100, 200, 300, and 400 using the whole space energy flux model (equation (10)). Scattering Q_s at PAS is approximately 200 to 300, but the coda appears to decay slightly faster than predicted by the model.

choosing t_1 and t_2 (equation (8)) from the duration of large motions on the vertical component, and integrating over this time interval. The power of the direct wave was estimated using all three components of motion over the time interval inferred from the vertical component. The integral of the squared velocity used for equations (10) or (21) was the square root of the sum of the squares of the integrals from each component of ground motion. Each component was then scaled by dividing the square root of this total squared velocity integral. The envelope of each component was then computed by forming the analytic signal [Farnbach, 1975] and taking its modulus. The total coda time series for one event was then found by summing the squares of the envelopes of the three components at each time point and taking the square root of the sum. Resulting coda envelopes for separate events were then averaged to obtain a better estimate of coda level.

Figure 11 shows the results of this process using four deep earthquakes recorded at PAS (Table 1). Deep events were chosen to avoid contamination by near-source scattering effects. The observed levels of coda are very high. Indeed, an examination of the raw data (e.g., Figure 2) shows that much of the coda comes from the horizontal components. Theoretical curves computed using equation (10) are superimposed on the coda decay curve in Figure 11 and show that an apparent scattering Q_s of 200 to 300 is required. The coda time decay appears to be very slow and is roughly consistent with $t^{-1.2}$ found in this model of scattering.

Figure 12 demonstrates, however, that the simple one-dimensional simulations are not consistent with coda decay following equation (10). The coda curve for the "20%" model was constructed by stacking 10 vertical and horizontal component realizations of models which had a velocity standard deviation of 20% and a layer thickness of 60 km. The "10%" curve was obtained by stacking nine vertical and horizontal component realizations for models which had a velocity standard deviation of 10% and a layer thickness of 30 km. The observed coda decay is linear on the logarithm plot and falls off much faster than implied by (10). The linear fall-off is consistent with the scattering layer-over-half-space model

where coda energy diffuses out of the layer into the half-space governed by equation (15). The one-dimensional simulations included no effect of anelastic attenuation.

Figure 12 also shows least squares linear fits to the coda decay to obtain Q_s and γ in equation (21). The slope of the log-coda curve yields γ , and the zero time intercept can be used to solve directly for Q_s . The standard deviation of the least squares fit was also used to estimate allowable Q_s variation by adding and subtracting the standard deviation from the zero intercept time to find a lower and upper bound of Q_s , respectively. These values are displayed in Table 3. Coda from the simulations show that the diffusing layer model correctly predicts the form of coda decay although the model does not formally treat the scattering mechanism of P to S conversions within the layer. The decay rate is very sensitive to the velocity standard deviation, but Q_s estimates are surprisingly the same, within the error of determination.

It is interesting to compare results for PAS with those from another station to get an appreciation for the level of scattering implied by the data. Three deep events recorded on the broadband DWWSSN system at State College, Pennsylvania (SCP) were analyzed in the same way. Event parameters can be found in Table 4, and the data are displayed in Figure 13. The Benioff 1-90 and intermediate-period DWWSSN systems are sufficiently similar for the purposes of this comparison, particularly since the same band-pass filter was used on the data.

Figure 14 compares the coda decay curves for PAS and SCP. Structure under SCP is seen to be simpler than that at PAS [Langston and Isaacs, 1981; Ammon, personal communication, 1988] and gives rise to lower amplitude P_s conversions as well as coda. Coda decay for SCP is twice as fast as that observed for PAS (Table 3). Q_s is found to be lower for PAS with use of equation (21), giving a value of 239 compared to 582 for SCP.

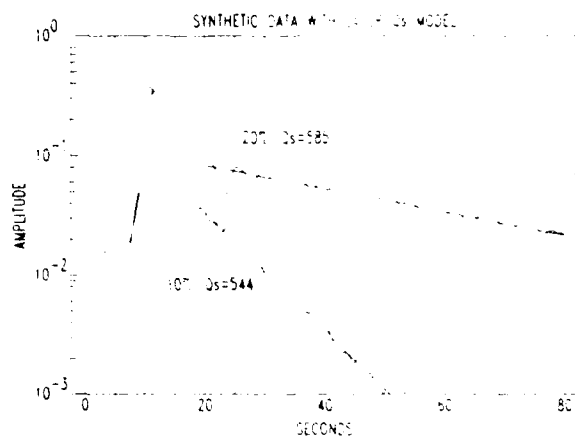


Fig. 12. Coda envelope stacks for the one-dimensional simulation. The "10%" envelope is the stack of 18 vertical and radial synthetic seismograms produced by nine realizations of the 30-km-thick layer model with average velocity of 5.5 km/s and velocity standard deviation of 10%. The "20%" envelope is the stack of 20 vertical and radial synthetic seismograms produced by 10 realizations of the 60 km thick layer model with average velocity of 6 km/s and velocity standard deviation of 20%. The straight lines are least squares fits of the coda. Q_s values are those inferred from the zero lapse time intercept of the linear fits (see text). Note that coda decay in the one-dimensional simulations agree with the assumption that coda energy follows a diffusion law for leaking into the half-space. Coda decay is controlled entirely by this process in the one-dimensional simulations.

TABLE 3. Q , and γ Determinations for Coda Stacks

Coda Stack	Least Squares Fit			Q	γ	High Q	Low Q
	Intercept	Slope	Standard Deviation				
10% simulation	-0.970	-0.050	0.079	544	0.229	784	380
20% simulation	-0.985	-0.0098	0.057	584	0.045	761	450
PAS data	-0.789	-0.0047	0.075	239	0.022	337	169
SCP data	-0.984	-0.0092	0.105	582	0.043	944	359

Scattering Q determinations were found using equation (21) for a 30-km-thick scattering layer with an average P velocity of 6 km/s.

DISCUSSION

The scattering layer-over-half-space model reproduces the principal behavior of the one-dimensional structure simulations (Figure 12) and is consistent with coda decay in the PAS and SCP data. The simple assumptions of homogeneity of the coda field and diffusion of energy into the half-space seem to describe the basic mechanisms of coda formation and is consistent with previous observations of the behavior of data and two-dimensional simulation studies.

Aki and Chouet [1975] estimated the diffusivity of the lithosphere in Japan and California using a diffusion model of coda formation applied to local earthquake data. They found high diffusion rates having the effect of homogenizing the coda field behind the wave front. Frankel and Wennerberg [1987] took these ideas further by examining the coda field in finite difference simulations and constructing a simple energy flux theory to explain the formation of coda. Although the assumptions of homogeneous coda and diffusive energy flow across the layer boundary are reasonable, the actual mechanisms of coda formation are not directly addressed in an equation like (21), which leads to the problem of estimating coda energy from an unknown wave field.

Much of the coda in the one-dimensional simulations is a product of P to S conversions and reverberations. The energy scattered into S waves is obviously a function of ray parameter. As the direct wave incidence angle increases, more P to S conversions will occur. This can be verified directly by calculation but can be seen in the behavior of the conversion coefficient at a boundary. Thus it can be expected that coda fall-off and levels will change for waves of different incidence angle if one-dimensional structure is appropriate. P to S scattering in two-dimensional structures is more complex [Frankel and Clayton, 1986; McLaughlin et al., 1985] but appears to become less sensitive to incidence angle. P and S to Rayleigh scattering is probably a major component of the coda field at relatively low frequencies (< 1 Hz) [Aki and Chouet, 1975]. These scattering mechanisms may control the coda formation in the data presented here. In terms of the application of equation (21) the problem amounts to estimating d , the scaling factor

relating energy density to wave amplitude in equation (4). Even for one-dimensional structure, d depends on incidence angle and includes the free surface receiver functions [e.g., Helmberger, 1968]. It is of some interest to examine the energy partitioning in the coda of the simulations and, making some simple assumptions, the partitioning seen in the data.

As an approximation, consider the coda power being composed of S wave E_c and P wave E_{c_p} powers

$$E_c = E_c + E_{c_p} \quad (22)$$

Also define the energy partitioning coefficient by

$$\Gamma = \frac{E_c}{E_{c_p}} \quad (23)$$

For plane wave propagation

$$\begin{aligned} E_c &= \rho \beta I_s \\ E_{c_p} &= \rho \alpha I_p \end{aligned} \quad (24)$$

where I_s and I_p are the estimated integrals of squared velocity for S wave and P wave motions, respectively. The S wave velocity is given by β . For one-dimensional structure models and for incident P waves of small incidence angle, S waves occur primarily on the horizontal component and P on the vertical. The respective wave integrals can therefore be directly estimated using (8) by performing the integration over the filtered and squared wave form from the end of the direct wave arrival to some reference time in the coda. This was done for the wave forms obtained from the 10% and 20% one-dimensional simulation models. Both models give similar results where, for the ray parameter considered (0.06 s/km) in constructing the synthetics, roughly 70% of the scattered energy occurs as S wave energy. (A value of 0.7 ± 0.3 was obtained for both simulations using the individual wave forms of each model realization.) Changing the ray parameter to 0.04 s/km, appropriate for source distances of 85 km, reduces the S wave energy to 50% and less for the synthetics. The free surface effect is assumed to be the same for both P and S for these low angles of incidence.

TABLE 4. Event Parameters for State College Data

Date	Origin Time, UT	Latitude, deg	Longitude, deg	M_s	Depth, km	Distance, deg	Back Azimuth, deg
Dec. 21, 1983	1214:18	28.2S	63.2W		602	70.0	166
Aug. 8, 1985	1635:58	6.1S	113.4E	5.7	596	144.0	341
Aug. 12, 1985	0436:43	7.0S	117.2E	5.6	599	143.8	334

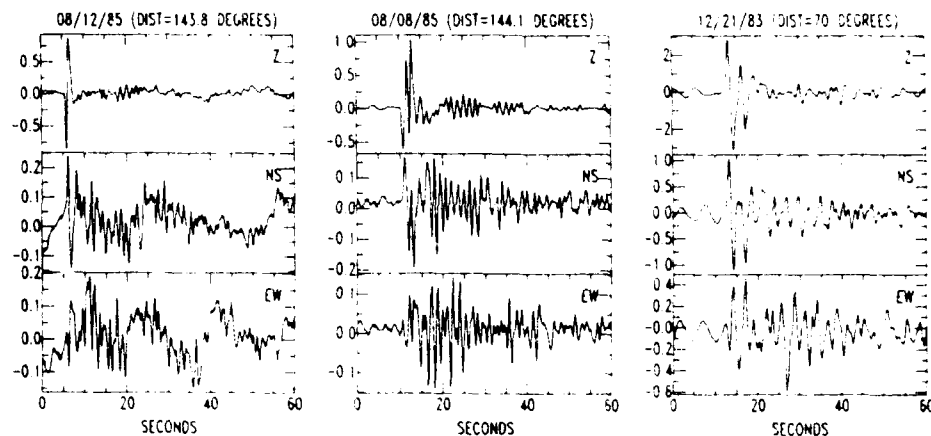


Fig. 13. Three-component data recorded at SCP on the DWSSN intermediate-period system (Table 4). Long-period noise seen on some horizontal wave forms (e.g., August 12, 1985) was largely removed by the band-pass filter used in this study.

Small differences in correcting the data for wave propagation effects are of little consequence to this discussion since wave types in the observed coda data are largely unknown. We treat the observed data in the same way where the S and P wave integrals are defined as

$$I_s = (I_{c_s}^2 + I_{c_t}^2)^{1/2} \quad (25)$$

$$I_p = I_{c_t}$$

where the subscripts Z , V , and E denote the component of ground motion. Assuming only S and P wave partitioning in the PAS data yields a partitioning coefficient of 1.7 ± 0.4 , a factor of 2-3 greater than expected compared to the one-dimensional simulations. This result is consistent with the coda being composed of low group velocity surface waves scattered from incident P and S waves. Instantaneous energy will be proportional to the group velocity so that assuming a higher S velocity in (25) will cause the energy to be overestimated. These observations are consistent with observations of the coda at arrays [Aki 1973, Aki and Chouet, 1975] and from theoretical wave propagation calculations [e.g., Levander and Hill, 1985]. Powell and Meltzer [1984] also found direct evidence for a high level of scattering under southern California in their study of coherency across the Caltech-U.S. Geological Survey large seismic array (SCARLET).

It thus appears that coda level and coda decay at PAS is inconsistent with plausible one dimensional Earth models. The observed data show slow coda decay, implying a relatively long dwell time of coda energy in the crust as well as high amplitudes. The high amplitudes are consistent with the coda field being primarily composed of scattered surface waves. Even the coda decay seen at SCP implies unreasonable one-dimensional structure, since the data imply virtually the same attenuation and decay as the 20% velocity model (Table 3).

These aspects of the receiver function data can be routinely quantified in other data sets to motivate an interpretation of structure under a receiver. If the receiver function coda data show tendencies that are inconsistent with simple one-dimensional models, then inversion of selected phases at long lapse times (> 10 s) from the first arrival or inversion of the entire wave form becomes suspect. This result is not surprising when one simply looks at the anomalies contained within the

data, but the theoretical treatment presented here can help quantify both the gross characteristics of the observed data and the justification of a particular modeling strategy.

P_s - P arrival times suggest that a major discontinuity occurs in the midcrust under PAS. Although the polarity of radial and tangential P_s is consistent with the interface dipping northward under the San Gabriel Mountains, dip is of the order of 10° or less, and the S wave velocity contrast must be unusually large (> 1 km/s). Qualitatively, a major crustal low velocity zone can explain these observations, but the extremely large P_s - P amplitude ratios probably imply that other factors are affecting the wave form such as ray focusing [Lee, 1983, Lee and Langston, 1983a, b].

The northward dip of the interface suggests that it is a major structure associated with the southward overthrusting of the San Gabriel Mountains. If the amplitude of the conversion is due to large velocity contrasts, then a low velocity zone is required at midcrustal to deep crustal levels. It is interesting to note that this low velocity zone occurs just under the seismogenic zone of the region and may be the seismic signature

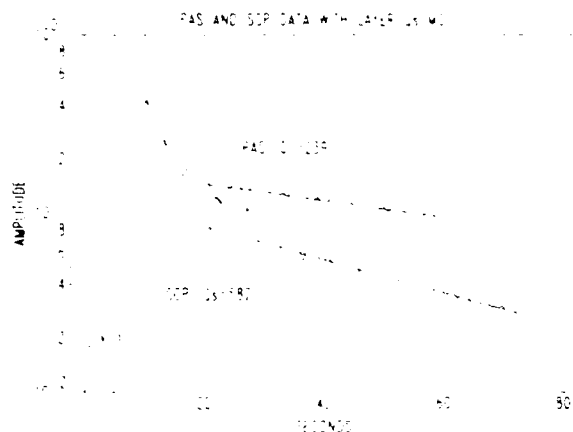


Fig. 14. Envelope stacks of the PAS and SCP data showing least squares fits of a line through coda with lapse times greater than 10 s (Q), inferred from each line; zero time intercept is also displayed. Coda excited at PAS attains higher levels and falls off more slowly than coda at SCP.

of the decoupling zone of upper crustal and lower crustal-upper mantle microplates [Humphreys, 1984; Webb and Kanamori, 1985].

The high velocity mantle anomaly under the Transverse Ranges inferred from past studies may have some effect in perturbing the incident P wave ray path. Rays will tend to be bent toward the vertical and toward the interior of the anomaly. However, the expected perturbation will only be a few degrees. The observed scattering effects induced by crustal heterogeneity dominate the character of the horizontal components of the teleseismic wave forms.

CONCLUSIONS

The receiver function data set for PAS suggests that the scattering is occurring in a highly heterogeneous crust. Broad-band Benioff 1-90 data from teleseisms show anomalous tangential particle motions and a high-amplitude coda which decays slowly. Initial portions of the radial and tangential receiver functions show a coherent inferred P_s conversion which displays a polarization anomaly of 45° for most data. Using the amplitude, polarity, and timing of this phase seen in stacks of the data and from a direct observation in an incident $PKIKP$ phase, a high S wave velocity contrast (>1 km/s) interface is inferred at approximately 20 km depth. The interface dips less than 10° to the north and appears to be a major structure associated with southward overthrusting of the San Gabriel Mountains.

Observed coda level and decay was examined using two methods. One was direct simulation of one-dimensional stochastic structures. Plane wave synthetic seismograms were computed for random plane-layered models with an exponential correlation function and with 10% and 20% standard deviations in velocity. The PAS data showed larger scattering effects than the simulations, indicating that geologically unreasonable one-dimensional models are required to explain the coda data. The one-dimensional models also are obviously deficient in explaining the degree of off-azimuth scattering seen in the data.

The other method consisted of examining coda behavior using an energy flux model developed for a scalar plane wave incident on a scattering layer over a homogeneous half-space. A scattering layer model was considered since it is likely that major velocity perturbations are largely confined to the crust. Two fundamental assumptions were made to develop the model and were based on previous empirical observations of the behavior of earthquake coda and numerical experiments. It was assumed that the coda field distributes itself homogeneously within the layer and that coda energy diffuses across the layer-half-space boundary. Coda decay is seen to be controlled entirely by the diffusion constant of energy flow across the layer boundary. Synthetic seismograms from the one-dimensional simulations show that the simple energy flux model explains the form of coda decay. One implication of this model is that the diffusion effect is indistinguishable from anelastic attenuation. Thus it is likely that teleseismic coda data cannot be used to estimate local anelastic attenuation.

PAS and SCP data from selected deep earthquakes were analyzed using this model and it was found that PAS had a lower scattering Q_c (~ 239) compared to SCP (~ 582) and that the coda decay for SCP was twice as fast as that for PAS. The absolute values of scattering Q_c obtained with the model are subject to assumptions on the types of waves contained within the wave field and probably represent lower bounds to the

actual Q values. The comparison between the two stations shows that scattering is lower in a tectonically quiescent area with less variable geology as expected.

An analysis of energy in the horizontal and vertical components of the one-dimensional synthetics and the PAS data suggests that much of the energy contained in the observed coda is from scattered surface waves.

APPENDIX

Nominal instrument constants for the Benioff 1-90 system are pendulum period of 1 s, galvanometer period of 90 s, damping constants of 1 for both the seismometer and galvanometer, a coupling constant of 0.05, and magnification of 3000 (H. Kanamori, personal communication, 1987). A calibration of the system was started in 1962 but was never totally completed. Calibration of the vertical component showed a peak magnification of 2700, 10% under nominal specifications. Experience with the system suggests that instrument constants are good to about 30%. Because calibration of the instruments can affect the results of rotation of the data and the source equalization, it is of some interest to examine the results of errors in the instrument constants.

Assuming that the receiver response is ideal and consists of motions confined to the sagittal plane containing the ray, vector rotation of the horizontal displacement components to obtain radial and tangential ground motions yields

$$\begin{aligned} u_R(t) &= R(t) \cdot [i_n(t) \cos^2 \theta + i_e(t) \sin^2 \theta] \\ u_T(t) &= R(t) \cdot [i_n(t) - i_e(t)] \sin 2\theta / 2 \end{aligned} \quad (A1)$$

where the subscripts R and T denote radial and tangential motions, respectively, and the subscripts n and e denote north-south and east-west motions, respectively. The θ is the back azimuth angle to the source from the receiver. The respective instrument responses are given by $i_n(t)$ and $i_e(t)$, and $R(t)$ is a common radial response for plane layered structure.

The largest errors in rotation occur when $\theta = 45^\circ$. Tangential motion, in this case, is caused by differences in the instrument response of the two components. Clearly, if small differences occur in the response, then the radial motions will be little affected, since the net response will be the average of the two. Magnification errors will primarily show up in the tangential component. In the worst case considered here, tangential motions will be approximately 30% of the radial component, if magnification is only known to 30%, and should look identical to the radial component in wave shape. The data for PAS (Figure 2) show extreme differences in wave shape between the horizontal components, which cannot be due to magnification errors.

The equations for electromagnetic seismographs [Hagiwara, 1958] were used to estimate the difference in instrument responses if 30% variations in the instrument constants are assumed. Figure A1 displays the results for amplitude spectra. Changes of 30% in the galvanometer period and damping and the seismometer period and damping were assumed relative to the nominal response. Theoretical responses were calculated in the frequency domain and inverse Fourier-transformed to obtain impulse responses. Using equation (A1) as a guide, the perturbed responses were then subtracted from the nominal response and then Fourier-transformed to obtain the amplitude spectrum. Thus the four curves below the nominal 1-90 response seen in Figure A1 are the amplitude spectra of the

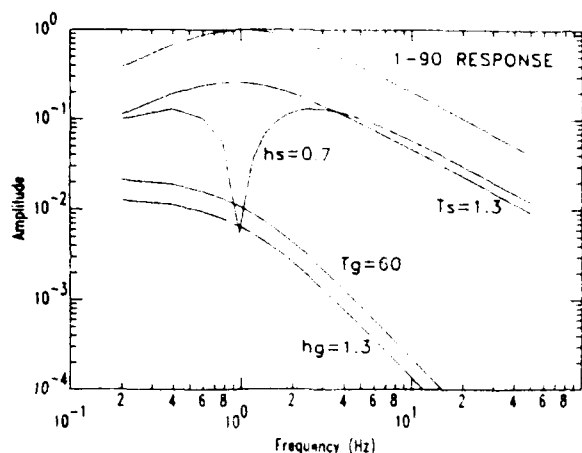


Fig. A1. Amplitude spectra of the nominal Benioff 1-90 response (top) and response differences (lower curves) assuming 30% variation in damping and free periods of the seismometer and galvanometer of the system. Parameters h_s , h_g , T_s , and T_g are the seismometer damping, galvanometer damping, seismometer period (in seconds), and galvanometer period, respectively. See text for explanation.

differentiated impulse responses. They can be considered numerical derivatives of the instrument response if divided by 0.3.

A change in the galvanometer period or damping results in a response 2-3 orders of magnitude lower than the nominal response in the band, centered about 1 Hz (Figure A1). Thus it is not likely that errors in these parameters will be of any consequence in the data. Changes of 30% in seismometer period produces a tangential impulse response about a factor of 4 lower than the nominal response and looks nearly identical to the nominal response. A change in seismometer period appears as a change in magnification. The tangential wave form would differ by only a constant compared to the radial wave form. A change in seismometer damping, however, has the greatest change in the shape of the spectrum. A 90° phase shift is evident at 1 Hz which, for band-limited data, would make the tangential motion appear Hilbert-transformed compared to radial motion. Fortunately, this response is 1-2 orders of magnitude lower than the nominal response. In summary, plausible changes in the instrument constants for the 1-90 system cannot explain the anomalous particle motions seen in the data.

Magnification errors cannot be discounted. However, an empirical test was made by comparing the ratio of north-south, east-west, and vertical amplitudes of the first P pulse observed in the 1-90 data with that seen in the 30-90 data. P wave data for the December 28, 1973, March 23, 1974, and November 29, 1974, events were used. Considering that the passbands of the two instruments are different, amplitude ratios of the different ground motion components between instruments were within 20% of each other.

Finally, the data can be used in the test proposed by Langston [1979] to demonstrate the major off-azimuth arrivals occur on both horizontal components for events with different back azimuths. Figure A2 shows the first 10 s of the P wave forms for the February 1, 1973, and December 28, 1973, events (also see Figure 2). Polarities have been adjusted to make the wave form comparison clearer, and the P waves have been aligned in time. The arrow in the middle pair of plots shows the location of the large P_s conversion studied in the main body of the paper. It clearly occurs on the north-south com-

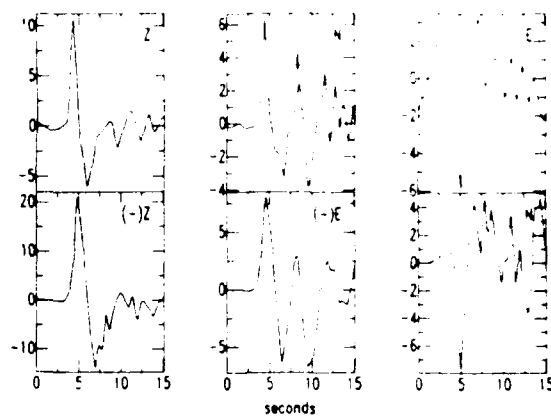


Fig. A2. Comparison of Benioff 1-90 three-component data from the February 1, 1973, event (top) and the December 28, 1973, event (bottom). Polarities have been reversed for the vertical (Z) and east-west (E) components of the December 28, 1973, event for comparison purposes. The vertical components are simple, showing a single impulsive P wave. The arrow shows the location of the major P_s conversion considered in this study. It occurs primarily on the N component for the February 1, 1973, event and on the E component for the December 28, 1973, event. Likewise, it is not obvious on the other respective horizontal components (right side), showing that both horizontal instruments respond similarly to the same wave propagation effect.

ponent for the February 1, 1973, event and on the east-west component of the December 28, 1973, event. Likewise, the corresponding east-west and north-south components (right pair of wave forms) show similar wave forms between events without the major arrival. This comparison shows that both horizontal instruments behaved in a similar fashion for the same wave propagation effect.

Acknowledgments. This research progressed from a study of the same data by J. J. Lee. He is gratefully acknowledged in collecting much of the PAS data and contributing as a colleague to the understanding and limitations of dynamic ray tracing to the receiver function problem. The personnel at the Seismological Laboratory at Caltech are also acknowledged for their help in collecting the data for this study. Hiroo Kanamori provided information on instrument calibration and is gratefully acknowledged. Hye-Sun Kim helped digitize much of the data seen here and Terry Ott also helped with data processing. I would also like to thank Chuck Ammon for deconvolving the SCP waveforms and contributing his comments on the paper. John Louie and Roy Greenfield also provided useful comments and interesting discussions on these topics. F. Lee Humphreys and Peter Malin reviewed the manuscript and made a number of useful suggestions for its improvement. Early parts of this research were supported by the National Science Foundation under grant EAR-8013704. This research was also sponsored by the Defense Advanced Research Projects Agency through the Air Force Geophysics Laboratory under contract F19628-87-K-0024.

REFERENCES

- Aki, K., Analysis of seismic coda of local earthquakes as scattered waves, *J. Geophys. Res.*, **74**, 615-631, 1969.
- Aki, K., Scattering of P waves under the Montana LISA, *J. Geophys. Res.*, **78**, 1334-1346, 1973.
- Aki, K., Scattering and attenuation of shear waves in the lithosphere, *J. Geophys. Res.*, **85**, 6496-6504, 1980.
- Aki, K., and B. Chouet, Origin of coda waves: Source, attenuation, and scattering effects, *J. Geophys. Res.*, **80**, 3322-3342, 1975.
- Burdick, L. J., and C. A. Langston, Modeling crustal structure through the use of converted phases in the teleseismic body waveforms, *Bull. Seismol. Soc. Am.*, **67**, 677-692, 1977.
- Cessaro, R. K., and R. Butler, Observations of transverse energy for P waves recorded on a deep-ocean borehole seismometer located in the northwest Pacific, *Bull. Seismol. Soc. Am.*, **77**, 2163-2180, 1987.

- Dainty, A. M., and M. N. Toksoz, Elastic wave propagation in a highly scattering medium—A diffusion approach, *J. Geophys.*, **43**, 375–388, 1977.
- Dainty, A. M., M. N. Toksoz, K. R. Anderson, P. J. Pines, Y. Nakamura, and G. Latham, Seismic scattering and shallow structure of the Moon in Oceanus Procellarum, *Moon*, **9**, 11–29, 1974.
- Farnbach, J. S., The complex envelope in seismic signal analysis, *Bull. Seismol. Soc. Am.*, **65**, 951–962, 1975.
- Frankel, A., and R. W. Clayton, Finite difference simulations of seismic scattering: Implications for the propagation of short-period seismic waves in the crust and models of crustal heterogeneity, *J. Geophys. Res.*, **91**, 6465–6489, 1986.
- Frankel, A., and L. Wennerberg, Energy-flux model of seismic coda: Separation of scattering and intrinsic attenuation, *Bull. Seismol. Soc. Am.*, **77**, 1223–1251, 1987.
- Gao, L. S., L. C. Lee, N. N. Biswas, and K. Aki, Comparison of the effects between single and multiple scattering on coda waves for local earthquakes, *Bull. Seismol. Soc. Am.*, **73**, 377–389, 1983.
- Gupta, I. N., and R. R. Blandford, A mechanism for generation of short-period transverse motion from explosions, *Bull. Seismol. Soc. Am.*, **73**, 571–591, 1983.
- Hadley, D., and H. Kanamori, Seismic structure of the Transverse Ranges, California, *Bull. Geol. Soc. Am.*, **88**, 1469–1478, 1977.
- Hagiwara, T., A note on the theory of the electromagnetic seismograph, *Bull. Earthquake Res. Inst. Univ. Tokyo*, **36**, 139–164, 1958.
- Haskell, N. A., Crustal reflection of plane P and SV waves, *J. Geophys. Res.*, **67**, 4751–4767, 1962.
- Hearn, T. M., and R. W. Clayton, Lateral velocity variations in southern California. I. Results for the upper crust from Pg waves, *Bull. Seismol. Soc. Am.*, **76**, 495–509, 1986a.
- Hearn, T. M., and R. W. Clayton, Lateral velocity variations in southern California. II. Results for the lower crust from Pn waves, *Bull. Seismol. Soc. Am.*, **76**, 511–520, 1986b.
- Hebert, L., and C. A. Langston, Crustal thickness estimate at AAE (Addis-Ababa, Ethiopia) and NAI (Nairobi, Kenya) using teleseismic P-wave conversions, *Tectonophysics*, **111**, 299–327, 1985.
- Helmberger, D. V., The crust-mantle transition in the Bering Sea, *Bull. Seismol. Soc. Am.*, **58**, 179–214, 1968.
- Humphreys, E., R. W. Clayton, and B. Hager, A tomographic image of mantle structure beneath southern California, *Geophys. Res. Lett.*, **11**, 625–627, 1984.
- Langston, C. A., The effect of planar dipping structure on source and receiver responses for constant ray parameter, *Bull. Seismol. Soc. Am.*, **67**, 1029–1050, 1977.
- Langston, C. A., Structure under Mount Rainier, Washington, inferred from teleseismic body waves, *J. Geophys. Res.*, **84**, 4749–4762, 1979.
- Langston, C. A., and C. M. Isaacs, A crustal thickness constraint for central Pennsylvania, *Earthquake Notes*, **52**, 13–22, 1981.
- Lee, J.-J., A three-dimensional ray method and its application to the study of wave propagation in crustal structure with curved layers, Ph.D. thesis, Pa. State Univ., University Park, 1983.
- Lee, J.-J., and C. A. Langston, Three-dimensional ray tracing and the method of principal curvature for geometric spreading, *Bull. Seismol. Soc. Am.*, **73**, 765–780, 1983a.
- Lee, J.-J., and C. A. Langston, Wave propagation in a three-dimensional circular basin, *Bull. Seismol. Soc. Am.*, **73**, 1637–1653, 1983b.
- Levander, A. R., and N. R. Hill, P-SV resonances in irregular low-velocity surface layers, *Bull. Seismol. Soc. Am.*, **75**, 847–864, 1985.
- McLaughlin, K. L., L. M. Anderson, and Z. A. Der, Investigation of scattering and attenuation of seismic waves using two-dimensional finite difference calculations, in *Multiple Scattering of Waves in Random Media and Random Rough Surfaces*, edited by V. V. Varadan and V. K. Varadan, pp. 795–822, Pennsylvania State University, University Park, Pa., 1985.
- Owens, T. J., Determination of crustal and upper mantle structure from analysis of broadband teleseismic P waveforms, Ph. D. thesis, Univ. of Utah, Salt Lake City, 1984.
- Owens, T. J., G. Zandt, and S. R. Taylor, Seismic evidence for an ancient rift beneath the Cumberland Plateau, TN: A detailed analysis of broadband teleseismic P wave forms, *J. Geophys. Res.*, **89**, 7783–7795, 1984.
- Owens, T. J., S. R. Taylor, and G. Zandt, Crustal structure at regional seismic test network stations determined from inversion of broadband teleseismic P waveforms, *Bull. Seismol. Soc. Am.*, **77**, 631–662, 1987.
- Powell, C. A., and A. S. Meltzer, Scattering of P-waves beneath SCARLET in southern California, *Geophys. Res. Lett.*, **11**, 481–484, 1984.
- Richards, P. G., and W. Menke, The apparent attenuation of a scattering medium, *Bull. Seismol. Soc. Am.*, **73**, 1005–1021, 1983.
- Vidale, J. E., and D. V. Helmberger, Elastic finite-difference modeling of the 1971 San Fernando, California, earthquake, *Bull. Seismol. Soc. Am.*, **78**, 122–141, 1988.
- Webb, T. H., and H. Kanamori, Earthquake focal mechanisms in the eastern Transverse Ranges and San Emigdio Mountains, southern California, and evidence for a regional decollement, *Bull. Seismol. Soc. Am.*, **75**, 737–757, 1985.
- Wu, R. S., and K. Aki, Scattering characteristics of elastic waves by an elastic heterogeneity, *Geophysics*, **50**, 582–595, 1985a.
- Wu, R. S., and K. Aki, Elastic wave scattering by a random medium and the small-scale inhomogeneities in the lithosphere, *J. Geophys. Res.*, **90**, 10,261–10,273, 1985b.
- Yerkes, R. F., T. H. McCulloh, J. E. Schoellhamer, and J. G. Vedder, Geology of the Los Angeles Basin area, California—An Introduction, *U.S. Geol. Surv. Prof. Pap.*, **420-A**, 1–47, 1965.

C. A. Langston, Department of Geosciences, Pennsylvania State University, University Park, PA 16802.

(Received May 4, 1988;
revised October 28, 1988;
accepted October 29, 1988.)

Scattering of Long-Period Rayleigh Waves
in Western North America
and the
Interpretation of Coda Q Measurements

by

Charles A. Langston

September 27, 1988

Revised November 30, 1988

Department of Geosciences
440 Deike Building
Pennsylvania State University
University Park, PA 16802

Abstract

The codas of long-period Rayleigh waves recorded at WWSSN and Canadian network stations in Western North America from eight underground explosions at NTS are examined in an effort to separate scattering and anelastic attenuation effects. Coda behavior of 0.1 and 0.2 hz Rayleigh waves follows coda characteristics seen in studies of short-period S waves. Coda decay rate is seen to be a stable observation over most stations in Western North America and is consistent with the hypothesis that backscattered surface waves from heterogeneities contained within the western half of the continent form the Rayleigh wave coda. The basic data observables of coda level and decay are interpreted using several plausible models. The single scattering model yields a coda Q consistent with previously determined Rayleigh anelastic attenuation coefficients. Separation of anelastic and scattering Q is possible using an energy flux model and shows that scattering Q is one to two orders of magnitude higher than anelastic Q. However, an energy flux model which incorporates a layer of scatterers over a homogeneous halfspace shows that all Rayleigh wave attenuation can be explained purely by scattering effects which include Rayleigh to body wave conversion. Coda can be fit equally well by these mutually incompatible models. It is not likely that the mechanisms of scattering or anelastic attenuation can be addressed by coda observations of a single homogeneous data set.

Introduction

Recent interest in characterizing lateral heterogeneity in the lithosphere has led to increasing study of coda waves which are a direct result of this heterogeneity. The working model developed by Aki(1969;1973;1980a;1980b) and Aki and Chouet(1975) that the S wave coda consists of backscattered S waves and is characterized by a single scattering Born approximation has found wide use in data interpretation of local seismograms (see the review article by Herraiz and Espinosa, 1987). This simple model explains much of the character of observed coda. What is not so evident, however, and is a point of some controversy, is the interpretation one makes of the coda Q , Q_c , parameter. Strictly speaking, Q_c is the attenuation effect due to scattering of the elastic wave by elastic heterogeneity. Empirically, Aki and Chouet(1975) and Aki(1980b) have suggested that Q_c is more closely related to anelastic Q . This interpretation was quantified by Frankel and Wennerberg(1987) and Wu(1985) who developed energy flux models which include anelasticity and multiple scattering of scalar waves. In Frankel and Wennerberg's model, scattering is manifest principally in coda amplitude levels while anelasticity dominates the coda decay with time.

In this paper, a coda data set consisting of long-period Rayleigh waves recorded within western North America is examined using techniques normally applied to high-frequency S wave codas. A primary motivation for this unusual approach was to examine the stability and empirical characteristics of coda amplitude decay of the fundamental mode Rayleigh wave for possible use in source magnitude and yield estimates.

Rayleigh wave periods of 20, 10 and 5 seconds are examined over coda lapse times of 1000 seconds (from source origin time). At these long lapse times and for Rayleigh wave group velocities of approximately 2.5 km/sec, scattered waves comprising the coda can originate from heterogeneities distributed over western North America and the eastern Pacific Ocean. This data set yields information on large scale heterogeneity in the continental crust.

Rayleigh coda will be examined using three different coda theories. The standard single-scattering model of Aki(1969) will be used to obtain Q_c and to compare it with previous determinations of anelastic Q made from spectral amplitude decay measurements of fundamental mode Rayleigh waves in western North America (Mitchell, 1975). The separation of anelastic Q and scattering Q will be attempted using the energy flux model of Frankel and Wennerberg(1987). Their model incorporates the effects of multiple scattering and conservation of wave energy and may represent a more realistic wave propagation situation compared to the single-scattering model. A third model based on the energy flux model but incorporating the effect of surface wave-to-body wave conversions from scattering in a heterogeneous layer over a homogeneous halfspace is also used to determine if this plausible scattering mechanism can explain the data. This last model was developed by Langston(1988) to explain P wave coda generated by teleseismic P waves scattering under a receiver. It was found that the three-component coda of teleseismic receiver functions recorded at Pasadena, California, had characteristics not explainable by the single scattering model and was also consistent with body wave-

to-surface wave conversion. The assertion is made that the reciprocal problem of surface wave-to-body wave conversion is equally important in the scattering of fundamental mode surface waves.

The results of this study show that it is possible to fit the coda data equally well with each theory. The stable aspect of the coda, coda decay with time, can be interpreted several different ways which may or may not include anelasticity. This result alone has important implications in the interpretation of coda at shorter periods. It suggests that homogeneous coda data sets cannot be used to discriminate between coda mechanisms and, based on the assumptions inherent in the models considered here, that the gross distribution of scatterers is as important to coda generation as is the density of scatterers.

Rayleigh Wave Data

Figure 1 shows the location of NTS and the station distribution used in this study. Long-period digital Rayleigh wave data were obtained from the Center for Seismic Studies, Arlington, Virginia, for a series of underground nuclear explosions at NTS. The data were previously digitized at a sampling rate of 1 sample/sec and were available from the Center's waveform database. Both WWSSN and Canadian network stations were used. Table 1 lists event parameters for the underground explosions and Table 2 lists station parameters with available events recorded by each station. Station data were chosen on the basis of good signal-to-noise characteristics and location within western North America.

Figure 2 shows the long-period vertical component for the

9/06/79 explosion recorded at COR. The raw data show a long duration coda arriving after the Airy phase, which is the largest arrival on the seismogram. Narrow band-pass filters of the data at center frequencies of 0.05, 0.1 and 0.2 hz show the development of coda. Three-pole, zero-phase, recursive Butterworth filters were used in all analyses of this paper. Corner frequencies for each of the respective bandpasses were 0.04/0.0667, 0.08/0.12, and 0.167/0.25 hz.

Note that coda is best developed for the 0.2 hz bandpass in Figure 2 and that there seems to be significant coda even for 0.05 hz Rayleigh waves. Figure 3 shows the LPZ component at LUB with similar bandpass filtered seismograms. In this case, noise dominates the coda for the 0.05 hz bandpass. It is also seen that the 0.2 hz bandpass contains much more energy before the peak of the envelope, compared to COR, which is likely to be from body waves and higher mode surface waves. This kind of contamination will affect the interpretation of coda and is discussed below. It was found that most stations had high levels of noise at 0.05 hz compared to coda after the vertical component Rayleigh arrival. Thus, 0.1 and 0.2 hz waves were principally analyzed.

Scattering Theories and Data Analysis

Coda amplitude is modeled in the time domain by fitting theoretical curves to the bandpass filtered data traces. Assuming that the coda is comprised of scattered Rayleigh waves, the single scattering model of Aki(1969) is

$$A_c(\omega, t) = \frac{C e^{-\omega t/2Q_c}}{\sqrt{t}} \quad (1)$$

where, $A_c(\omega, t)$ is the envelope of coda amplitude, Q_c the coda Q parameter, ω is circular frequency, and t the time from event origin time. C is a constant which contains the source spectrum and density of scatterers.

An energy flux model for Rayleigh wave scattering can be constructed following Frankel and Wennerberg(1987). Assuming radiation from a point source in a scattering halfspace, Rayleigh wave energy will propagate outward with the group velocity in an expanding cylindrical wavefront of radius r . The total energy is given by

$$E_T = E_D + E_c \quad (2)$$

where E_D the direct Rayleigh wave energy and E_c coda wave energy. Following Frankel and Wennerberg's(1987) development for a cylindrical wave, coda amplitude is given by

$$A_c(\omega, t) = \frac{d \sqrt{E_T}}{\sqrt{\pi \delta z} U t} (1 - e^{-\omega t/Q_s})^{\frac{1}{2}} e^{-\omega t/2Q_I} \quad (3)$$

where d is a scale factor relating Rayleigh wave energy density to amplitude, U is the group velocity, Q_s is the Q of the scattering medium, Q_I is the anelastic or intrinsic Q of the medium, and δz is the average depth of Rayleigh penetration at the cylindrical wavefront.

The total energy, E_T , is found by correcting the amplitude of

the direct Rayleigh wave for scattering and anelastic attenuation suffered in transit. If E_D' is the observed direct wave energy, then

$$E_T = E_D' e^{\omega t_d/Q_S} e^{\omega t_d/Q_I} \quad (4)$$

The direct Rayleigh wave arrival time is $t_d = r/U$. Furthermore

$$d^2 E_D' = U I_D 2\pi r \delta z \quad (5)$$

where,

$$I_D = \int_{t_1}^{t_2} v^2(t) dt \quad (6)$$

and $v(t)$ is particle velocity. In practice, a choice of t_1 and t_2 must be made to estimate where the main Rayleigh pulse occurs.

Using relations (4) and (5) to obtain E_T and substituting back into (3) gives

$$A_c(\omega, t) = \frac{\sqrt{2} I_D t_d}{t} e^{\frac{\omega t_d}{2} \{Q_S^{-1} + Q_I^{-1}\}} (1 - e^{\omega t/Q_S})^{\frac{1}{2}} e^{-\omega t/2Q_I} \quad (7)$$

The principal assumptions in this model are that scattered coda waves are homogeneously distributed behind the Rayleigh wave front and that there are no conversions from Rayleigh to other wave types. The functional form of (7) allows, in principle, the separation of Q_S and Q_I . Frankel and Wennerberg(1987) show that coda time decay is controlled mainly by Q_I but that coda levels

are weakly affected by Q_s .

Langston(1988) studied coda contained within teleseismic receiver functions for Pasadena station and concluded that yet another mechanism could affect the level and decay of coda in addition to scattering and anelastic attenuation. High levels and long duration of P wave coda implied that considerable scattering occurred in the crust and lithosphere under the station. Analysis of plane layered but random velocity structures situated over a homogeneous halfspace showed that theoretical P coda was strongly affected by this gross distribution of scatterers as well as their density. Coda was seen to decay quickly with time for models with low velocity variance compared to models with high velocity variance. Thus, a model with a large amount of wave scattering would give an implausible higher Q according to the single scattering approximation. The physical mechanism which controlled coda decay was body wave radiation into the halfspace. A simple diffusion law for energy propagation out of the scattering layer was sufficient to parameterize the effect for both synthetics and data.

Numerous theoretical studies (e.g., Munasinghe and Farnell, 1973; Martel et al, 1977; Vidale and Helmberger, 1988; McLaughlin and Jih, 1988) and several observational studies (Key 1967;1968; Greenfield, 1971; Aki and Chouet, 1975; Langston, 1988) have shown that heterogeneous structure gives rise to significant body wave-surface wave conversion and interaction. Intuitively, it is easy to envision the situation where significant parts of Rayleigh wave energy are converted to body waves which then radiate away from the surface to other distances. Indeed, recent calcu-

lations (McLaughlin and Jih, 1988) show that such a mechanism is very important in the attenuation of 1hz Rayleigh waves. The converted body waves which radiate away from the free surface will take energy from the primary Rayleigh wave as well as from the coda arriving afterwards. This radiation effect could mimic anelasticity as seen in Langston(1988).

Following Langston(1988) an energy flux model which incorporates radiative diffusion can be constructed for a scattering Rayleigh wave. Instead of equation (2), the total energy flux for such a case can be written as

$$E_T = E_D + E_C + E_R \quad (8)$$

where the new energy term E_R represents scattered energy from the coda and the direct Rayleigh wave which diffuses into the half-space from the layer of scatterers. Since the total energy of the system is constant,

$$\frac{dE_D}{dt} + \frac{dE_C}{dt} + \frac{dE_R}{dt} = 0 \quad (9)$$

Assuming that the rate of energy which leaks out of a layer δz in thickness is proportional to amount of coda and direct wave energy within the layer gives

$$\frac{dE_R}{dt} = \gamma (E_C + E_D) \quad (10)$$

such that at $t=0$, $E_R=0$. The proportionality constant is γ , the energy diffusivity.

scattering attenuation, equation (12), the radiative diffusion effect represents one of the mechanisms inherent in producing attenuation due to scattering. The other mechanism involves scattering of direct wave energy into the coda field before coda energy leaks into the halfspace. Clearly, equation (14) only makes physical sense when $Q_S^{-1} \geq Q_R^{-1}$. Otherwise, the radiative diffusion mechanism would take more energy out of the direct wave than is available and would violate the conservation of energy equation (8).

The observed data at each station were normalized following (6). Figure 4 shows the computational sequence for the 9/27/78 event at ALQ. First the vertical data are bandpass filtered to obtain a trace proportional to velocity. The trace is then squared and integrated. Time t_1 was always taken as the origin of the trace and t_2 chosen as that representing the main envelope of the filtered Rayleigh pulse. As seen in Figure 4, the error in this estimate is of the order of 10% since the squared coda amplitude formed a minor part of the signal in all cases. The square root of I_D was then divided into the trace point by point.

Individual coda envelopes were then computed from the normalized, filtered traces by calculating the amplitude of the analytic signal (Farnbach, 1975). The envelopes were then averaged together at each station to smooth fluctuations in the coda.

The logarithm of equations (1), (7) and (14) were then fit to the logarithm of the averaged envelope data using a least-squares algorithm. Analytic partial derivatives of $\log(C)$, Q_C^{-1} , Q_S^{-1} , Q_I^{-1} , and Q_R^{-1} were determined and used to construct the normal equations. The inversion then iteratively solved for these atte-

uation coefficients except in the case of equation (1) which was linear and with Q_c^{-1} and $\log(C)$ obtainable in one iteration.

Inversions using equation (7) were insensitive to starting model and uniformly converged in all cases within three iterations. However, inversions for Q_R^{-1} and Q_S^{-1} using equation (14) were sensitive to starting model. If the starting model was too far from the true model (based on synthetic tests), then parameter perturbations occasionally caused Q_R^{-1} to be greater than Q_S^{-1} in violation of energy conservation. A strategy was used in which Q_R^{-1} was estimated from the slope of the log coda envelope and then a small difference in the two attenuations was assumed for a joint inversion. Convergence in three iterations for each case was again obtained using this strategy. Reasonably close but different starting models had little effect on convergence.

The variances of the attenuation coefficients were found by multiplying the variance of the data fit with the covariance matrix of the least-squares system of equations (e.g., see Aki and Richards, 1980, page 688).

The amount of coda fit with these equations varied according to the data length of the available seismograms at each station and the noise level. It was found that the signal-to-noise level was poor for 20 sec (0.05 hz) coda waves where the noise was defined as the trace before the P wave arrival (see Figure 3). Development of coda for 0.2 and 0.1 hz Rayleigh waves appeared to be stable approximately 100 sec after the Rayleigh arrival. The maximum lapse time was always defined by the shortest signal length available from the digital waveform data base.

Figure 5 displays the coda fits for 0.1 hz Rayleigh coda.

Figure 6 shows fits for 0.2 hz coda. Since each coda theory fit the data equally well only the fit for the single scattering model is shown. Figures 7 through 11 show the inferred Q parameters for each model and frequency.

Discussion

Codas for both 0.1 and 0.2 hz Rayleigh waves are seen to decay linearly on the log-amplitude plots of Figure 5 and 6. Thus, these waves are similar in character to coda seen in local seismograms (Aki, 1969; 1980a; Aki and Chouet, 1975; Rautian and Khalturin, 1978; Rautian et al 1978). The 0.2 hz coda likely contains scattered energy of other seismic phases such as the S wave and higher mode Rayleigh waves. This is evident in Figure 6 where large pre-Rayleigh arrivals can be seen in data from the more distant stations before the peak of the amplitude envelope. This contamination is bothersome and will affect the Q determinations in an unknown way. However, the linear coda decay will simply be treated as an empirical observation. The non-unique interpretation of its meaning will be illustrated by the three model fits.

The single scattering model (Figure 7) yields Q_c for both frequencies that are comparable. Note the stability of the determination for most stations falling between 100 and 250. This simple result quantifies the observation that the log-coda slope appears to be approximately the same for any station in western North America. This observation is consistent with the interpretation that coda consists of waves scattered over the western half of the continent. Nevertheless there may indica-

Substitution of (10) into (9) and solving the differential equation for $E_D + E_c$ gives

$$E_D + E_c = E_T e^{-\gamma t} \quad (11)$$

since at $t=0$ there is no coda energy flux, E_c and the direct wave contains all of the energy of the system. If the effect of scattering attenuation is defined in the conventional way (e.g., Frankel and Wennerberg, 1987) as

$$E_D = E_T e^{-\omega t/Q_S} \quad (12)$$

and (12) is substituted into (11), the coda energy flux is given by

$$E_c = E_T [1 - e^{-\omega t(Q_S^{-1} - Q_R^{-1})}] e^{-\omega t/Q_R} \quad (13)$$

where the "radiative Q", Q_R is defined by

$$\gamma = \omega/Q_R .$$

Following the energy flux development above with this new term and ignoring anelasticity gives the coda amplitude

$$A_c(\omega, t) = \frac{\sqrt{2} I_D^d}{t} e^{\omega t_d/2Q_S} [1 - e^{-\omega t(Q_S^{-1} - Q_R^{-1})}]^{\frac{1}{2}} e^{-\omega t/2Q_R} . \quad (14)$$

Comparing (14) with (7), it can be noted that the radiative diffusion of converted Rayleigh-to-body waves in the coda mimics the effect of anelasticity. Because of the definition used for

tions that receiver effects are present particularly for ALQ and SES at 0.1 hz.

Mitchell (1975) studied distance-amplitude relationships for fundamental mode Rayleigh waves from two explosions in Colorado. His attenuation coefficients were greater for western North America compared to the east. If an average group velocity of 2.88 km/sec is taken to represent both 0.1 and 0.2 hz waves and the upper bound of Mitchell's estimates for attenuation coefficients is used, values of about 500 and 135 are obtained for anelastic Q measured at 0.1 and 0.2 hz, respectively. However, Hwang and Mitchell(1987) discuss Q models for western North America based on more recent measurements made by Chen(1985). Chen's attenuation coefficients for 0.1 and 0.2 hz Rayleigh waves yield average Q 's of about 140 for both wave frequencies. These empirical values agree quite well with Q_c (Figure 7) determined from Rayleigh coda. This suggests that the same attenuation processes act on direct Rayleigh waves as well as on scattered Rayleigh waves in the coda. A case can be made that anelastic attenuation dominates both coda and direct waves, if it can be determined that contributions from scattering effects are small.

Separation of Q_s and Q_I is possible with the energy flux model, equation (7). At 0.1 hz (Figure 8), Q_s is seen to be one to two orders of magnitude greater than Q_I . Values for Q_I are comparable to Q_c (Figure 7) which demonstrates the sensitivity of Q_I to the slope of the log-coda curve. Q_s is primarily obtained from the zero lapse time intercept in the inversion. Q_s will be sensitive to the way the direct Rayleigh wave is normalized. Any propagation effects which affect the direct wave can bias the Q_s

estimate. Focussing or defocussing of the direct wave by multipathing is a plausible and likely mechanism for variation in this parameter with position in western North America (Frankel and Wennerberg, 1987). Indeed, the marked low value of Q_S at PNT is consistent with observations made by Mitchell (1975) on low amplitude Rayleigh waves observed in the Canadian Cordillera.

The difference between Q_S and Q_I at 0.2 hz is somewhat less (Figure 9) than that at 0.1 hz but is still about one order of magnitude. Lower values of Q_S at 0.2 hz may imply larger scattering effects for higher frequency Rayleigh waves. These inferred values may also imply larger contributions of other scattered waves in the Rayleigh coda. Q_S will tend to decrease if the likely contamination of body and higher mode surface waves becomes significant. Note that Q_I for 0.1 and 0.2 hz waves are again similar.

Interpretation of the same data set with the radiative diffusion model points out the non-uniqueness of coda interpretation and the importance of scattering mechanism and scatterer distribution in creating apparent anelastic effects. There is no effect of anelasticity parameterized within the model. Considering the functional similarity of equations (7) and (14), it is not surprising that the "radiative" Q , Q_R , is nearly the same as Q_I in all cases (Figures 10 and 11) for each station. Both Q_R and Q_S are measures of the scattering efficiency of the medium but are influenced profoundly by the scatterer geometry. It is interesting to note that in both cases (Figures 10 and 11) both Q 's are nearly the same. The interpretation could be made that the rate of energy scattered out of the Rayleigh wave is about equal

to the rate at which it gets radiated into the mantle as body waves. Although coda is produced by scattering, most scattered energy flows out of the system into the mantle.

Although most stations displayed significant noise for coda in the 0.05 hz bandpass, signals at MSO and PNT were adequate for inversion. Table 3 shows the inferred Q values from each type of inversion. Q values for MSO determined from all three theories were comparable to those found for 0.1 hz coda.

Those for PNT, however, show very anomalous behavior. The direct Rayleigh wave at PNT was generally lower in amplitude compared to other stations at similar distance and had relatively higher coda levels. Q_C , Q_I , and Q_R all yielded very low values near 30. Q_S for the energy flux and radiative diffusion models were also very low. This anomalous behavior can be explained if structure near the stations or along the path serves to defocus the direct wave arrival. Defocussing will cause a small observed direct Rayleigh wave. Since the trace is normalized to the inferred direct wave, coda will be artificially enhanced causing apparent low Q's.

There have been numerous studies of coda waves (Herraiz and Espinosa, 1987) many of which make empirical correlations of Q_C with tectonic province or other measures of anelasticity. There can be no doubt that coda ultimately comes from waves scattered from heterogeneity in the lithosphere. However, it is clear from this study that the interpretation of coda mechanism is still problematical and tied to theory assumptions. Observations of coda in a homogeneous data set (e.g., S coda from shallow events or surface waves from explosions) may be interpreted in several

plausible ways. These results and those of Langston(1988) suggest that experiments be designed to constrain the gross geometry of scatterers in addition to measuring coda and direct wave decay characteristics. It might be fruitful to base data interpretations on accurate numerical models of elastic wave scattering where waves of differing type sample the same structure (e.g., Frankel and Clayton, 1986). For example, the combined observations of teleseismic body waves, local earthquake S waves, and regional surface waves in a particular region may be incorporated into a self-consistent structure and attenuation model. These speculations aside, there is the need to accurately address the wave scattering mechanisms which come to play in shaping the seismic coda.

Conclusions

Coda for 0.1 and 0.2 hz Rayleigh waves propagating from NTS to western North American seismic stations display exponential decay with time in a similar fashion to short-period S wave coda from local earthquakes. The exponential decay is similar for most stations and implies coda Q's of 100-250 for both frequencies. This behavior is consistent with coda waves being produced from heterogeneity distributed across the western half of North America.

Inversion of stacked coda envelopes using three fundamentally different theories yields equally good fits to the data. If the single scattering model is assumed, coda Q is consistent with previously determined anelastic Q for the region. Separation of scattering Q and anelastic Q using Frankel and Wennerberg's(1987)

energy flux formalism again produces consistent anelastic Q and a scattering Q one to two orders of magnitude larger than anelastic Q. A third theory which incorporates the radiation of scattered surface-to-body wave conversions into a halfspace underlying a scattering layer can also adequately explain coda level and decay without recourse to anelasticity.

Although coda and direct Rayleigh wave behavior is consistent with the presence of significant anelasticity in the crust of western North America, there is no diagnostic test that can be made with existing theory on this homogeneous data set to discriminate between scattering and anelastic effects. The radiative diffusion model constructed on the basis of teleseismic P wave receiver functions and modified for the Rayleigh wave data suggests that the overall geometry of scatterers within the lithosphere may be as important to the behavior of the coda as the scatterer density.

Acknowledgements

This research was sponsored by the Defense Advanced Research Projects Agency through the Air Force Geophysics Laboratory under contract #F19628-87-K-0024 and by the Arms Control and Disarmament Agency, Verification Bureau. Stimulating discussions on scattering theory with Chuck Ammon and Roy Greenfield are gratefully acknowledged and significantly contributed to the results of this study. Brian Mitchell contributed a useful review which improved the paper. Richard Baumstark at the Center for Seismic Studies provided the necessary help in obtaining the surface wave data.

References

- Aki, K.(1969). Analysis of seismic coda of local earthquakes as scattered waves, Jour. Geophys. Res., 74, 615-631.
- Aki, K.(1973). Scattering of P waves under the Montana LASA, Jour. Geophys. Res., 78, 1334-1346.
- Aki, K.(1980a). Scattering and attenuation of shear waves in the lithosphere, Jour. Geophys. Res., 85, 6496-6504.
- Aki, K.(1980b). Attenuation of shear waves in the lithosphere for frequencies from 0.05 to 25hz, Phys. Earth. Planet. Int., 21, 50-60.
- Aki, K., and B. Chouet(1975). Origin of coda waves: source, attenuation, and scattering effects, Jour. Geophys. Res., 80, 3322-3342.
- Aki, K., and P.G. Richards(1980). Quantitative seismology: Theory and Methods, W.H. Freeman and Company, San Francisco.
- Chen, J.J.(1985). Lateral variation of surface wave velocity and Q structure beneath North America, Ph.D. thesis, Saint Louis University.
- Farnbach, J.S.(1975). The complex envelope in seismic signal analysis, Bull. Seism. Soc. Am., 65, 951-962.
- Frankel, A., and Clayton, R.W.(1986). Finite difference simulations of seismic scattering: implications for the propagation of short-period seismic waves in the crust and models of crustal heterogeneity: Jour. Geophys. Res., 91, 6465-6489.
- Frankel, A., and L. Wennerberg(1987). Energy-flux model of seismic coda: separation of scattering and intrinsic attenuation, Bull. Seism. Soc. Am., 77, 1223-1251.
- Greenfield, R.J.(1971). Short-period P-wave generation by Rayl-

- eight-wave scattering at Novaya Zemlya, Jour. Geophys. Res., 76, 7988-8002.
- Herraiz, M., and A.F. Espinosa(1987). Coda waves: a review. PAGEOPH. 125, 499-577.
- Hwang, H.-J., and B.J. Mitchell(1987). Shear velocities, Q , and the frequency dependence of Q in stable and tectonically active regions from surface wave observations, Geophys. J. R. astr. Soc., 90, 575-613.
- Key, F.A.(1967). Signal-generated noise recorded at the Eskdalemuir seismometer array station, Bull. Seis. Soc. Am., 57, 27-37.
- Key, F.A.(1968). Some observations and analyses of signal generated noise, Geophys. J.R. astr. Soc., 15, 377-392.
- Langston, C.A.(1988). Scattering under Pasadena, California, Jour. Geophys. Res., in press.
- Martel, L., M. Munasinghe, and G.W. Farnell(1977). Transmission and reflection of Rayleigh wave through a step, Bull. Seis. Soc. Am., 67, 1277-1290.
- McLaughlin, K.L., and R.-S. Jih(1988). Finite-difference simulations of Rayleigh-wave scattering by shallow heterogeneity. Report AFGL-TR-87-0322, Air Force Geophysics Laboratory, Hanscom Air Force Base, MA, 108 pages. ADA194961
- Mitchell, B.J.(1975). Regional Rayleigh wave attenuation in North America, Jour. Geophys. Res., 80, 4904-4916.
- Munasinghe, M., and G.W. Farnell(1973). Finite difference analysis of Rayleigh wave scattering at vertical discontinuities. Jour. Geophys. Res., 78, 2454-2466.
- Rautian, T.G., and V.I. Khalturin(1978). The use of the coda for

determination of the earthquake source spectrum, Bull. Seis. Soc. Am., 68, 923-948.

Rautian, T.G., V.I. Khalturin, V.G. Martynov, and P. Molnar(1978). Preliminary analysis of the spectral content of P and S waves from local earthquakes in the Garm, Tadjikistan region, Bull. Seis. Soc. Am., 68, 949-971.

Vidale, J.E., and D.V. Helmberger(1988). Elastic finite-difference modeling of the 1971 San Fernando, California, earthquake, Bull. Seism. Soc. Am., 78, 122-141.

Wu, R.S.(1985). Multiple scattering and energy transfer of seismic waves - separation of scattering effect from intrinsic attenuation - I. Theoretical modelling, Geophys. J. R. astr. Soc., 82, 57-80.

Table 1 - NEIS Explosion Parameters

<u>Index</u>	<u>Event</u>	<u>Date</u>	<u>Origin Time</u>	<u>Latitude</u>	<u>Longitude</u>	<u>mb</u>
1	Sandreef	11/09/77	22:00:00.1	37.07N	116.05W	5.7
2	Panir	8/31/78	14:00:00.2	37.27	116.35	5.6
3	Rummy	9/27/78	17:20:00.0	37.07	116.01	5.7
4	Pepato	6/11/79	14:00:00.0	37.29	116.45	5.5
5	Hearts	9/06/79	15:00:00.1	37.08	116.05	5.8
6	Sheepshead	9/26/79	15:00:00.1	37.22	116.36	5.6
7	Kash	6/12/80	17:15:00.1	37.28	116.45	5.6
8	Tafi	7/25/80	19:05:00.1	37.25	116.47	5.5

Table 2 - Station Data and Event Distribution

<u>Station</u>	<u>Distance(km)</u>	<u>Azimuth($^{\circ}$)</u>	<u>Events</u>
ALQ	930	104	1, 3, 4, 6
COR	980	326	1, 5, 6, 7, 8
GOL	990	72	1, 3, 4, 5, 6
JCT	1710	112	5, 6, 7
LUB	1380	104	1, 5, 6, 7, 8
MSO	1060	10	1, 3, 4, 5, 6, 7
EDM	1770	7	1, 2, 3, 4, 5, 6
PNT	1340	350	all
SES	1500	15	1, 2, 3, 8

Table 3 - Inversion Results for 0.05 hz coda

Station	Energy Flux			Radiative	
	Q_C	Q_S	Q_I	Q_S	Q_R
MSO	222	2577	232	213	232
	(286/182)*	(2878/2334)	(301/189)	(272/175)	(300/189)
PNT	29	127	31	25	31
	(30/28)	(134/121)	(32/30)	(26/24)	(32/30)

* Numbers in parentheses denote high and low values of Q based on one standard deviation of error in the inverted attenuation.

Figure Captions

Figure 1: Map of western North America showing WWSSN and Canadian network stations used for the study of Rayleigh coda from nine underground nuclear explosions at NTS. Also shown are the great circle paths between NTS and the stations.

Figure 2: Long-period vertical component at COR (Corvallis, Oregon) showing the fundamental mode Rayleigh wave and coda for the 9/06/79 explosion. Below the top data trace are three different bandpass filtered traces showing the development of coda at frequencies of 0.05, 0.1 and 0.2 hz. Amplitudes for the filtered traces have been normalized according to the procedure discussed in the text.

Figure 3: Long-period vertical component at LUB (Lubbock, Texas) for the 9/26/79 explosion. Same scheme as Figure 2. Note the large amount of energy occurring before the peak of the 0.2 hz bandpass. These arrivals are associated with the shear wave and higher mode surface waves and likely contribute to the coda.

Figure 4: Example of the computational steps involved in normalizing each data trace. The top trace shows the long-period vertical component recorded at ALQ (Albuquerque, NM) for the 9/27/78 explosion. The data are bandpass filtered, squared, and then integrated. I_D is chosen from the integrated trace based on the duration of the fundamental mode wave packet seen in the squared trace. The arrow shows the pick of t_2 for equation (6). The error in normalization is less than 10% for all cases since the coda is much smaller than the peak amplitude of the fundamental mode Rayleigh wave.

Figure 5: Stacked coda envelopes (0.1 hz) for each station with the fit for the single scattering approximation model. Coda envelopes were shifted in amplitude in each graph by a factor of 10 for plotting purposes. Stations have been grouped by distance (see Table 2). The peak in each envelope corresponds to the direct Rayleigh arrival. Note that the envelope slopes are comparable for all stations.

Figure 6: Stacked coda envelopes (0.2 hz) with coda fits. Same scheme as Figure 5.

Figure 7: Inferred Q_c values for the single scattering model. Error bars show one standard deviation in the parameter estimate from the inversion algorithm. Triangles are for 0.1 hz coda. Circles are for 0.2 hz coda. Note the clustering of Q_c values between 100 and 200.

Figure 8: Q_I and Q_S determinations for 0.1 hz coda using the energy flux model, equation (7). Note the change in scale for Q_S . Scattering Q 's are one to two orders of magnitude greater than anelastic Q 's. Anelastic Q clusters around 100.

Figure 9: Q_I and Q_S determinations for 0.2 hz coda for the energy flux model. Results are similar to those at 0.1 hz.

Figure 10: Scattering Q , Q_S , and "radiative" Q , Q_R , for 0.1 hz coda inferred using equation (14). In this case, radiative diffusion of Rayleigh-to-body wave conversions out of the crustal waveguide mimics the effect of anelasticity.

Figure 11: Radiative diffusion model results for 0.2 hz coda. Same scheme as Figure 10. Note that Q_S and Q_R are nearly the same for all cases.

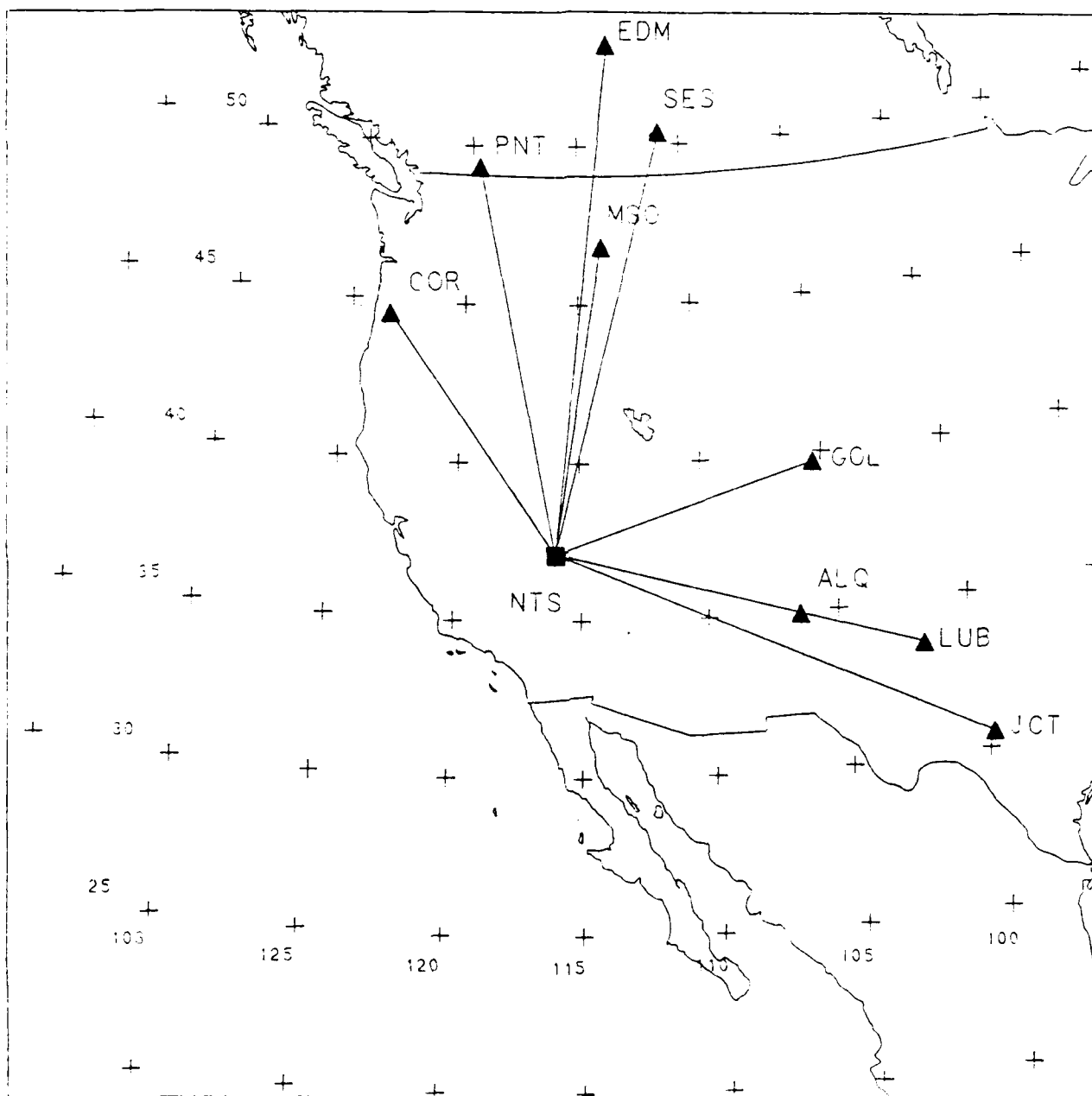


Figure 1

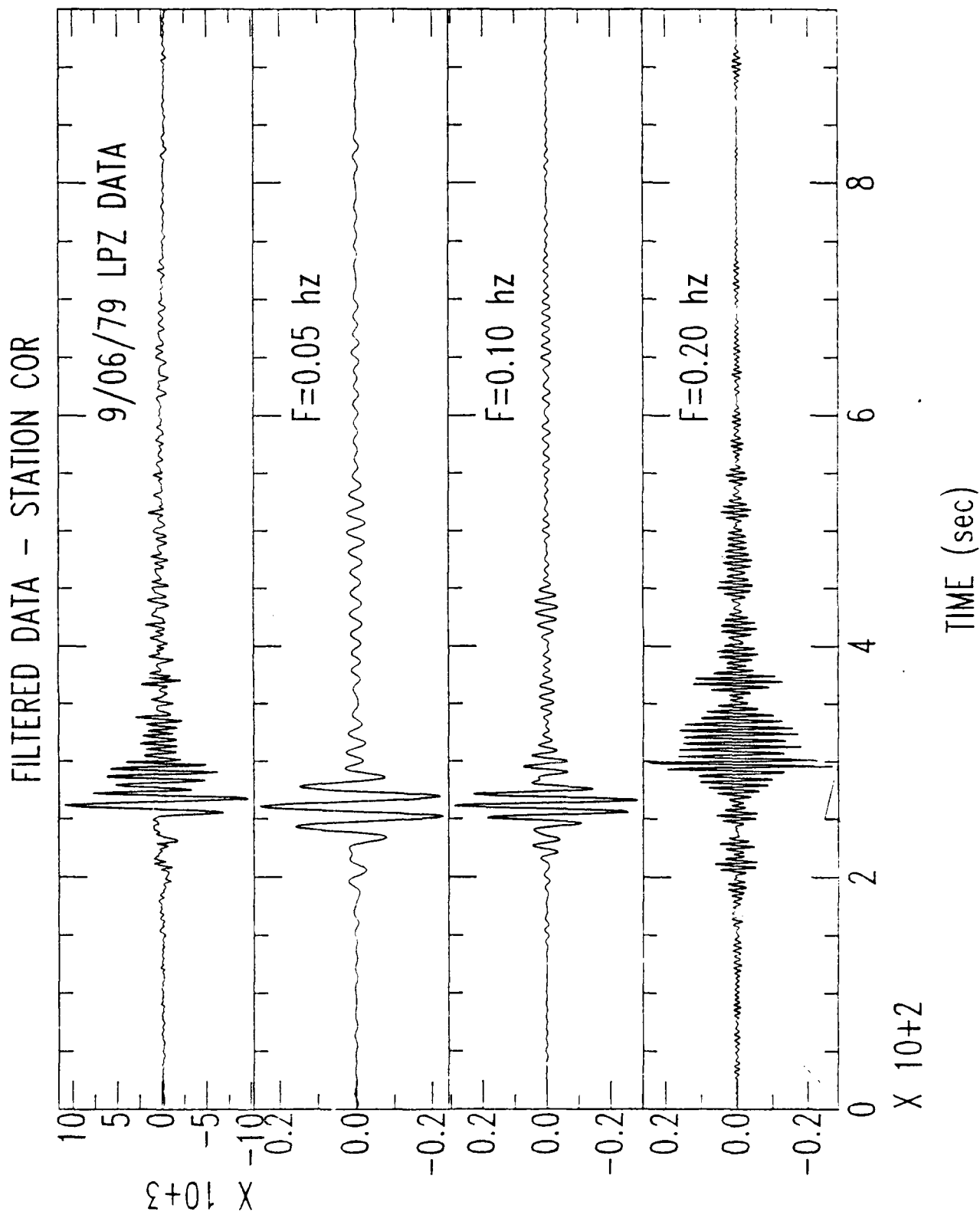


Figure 2

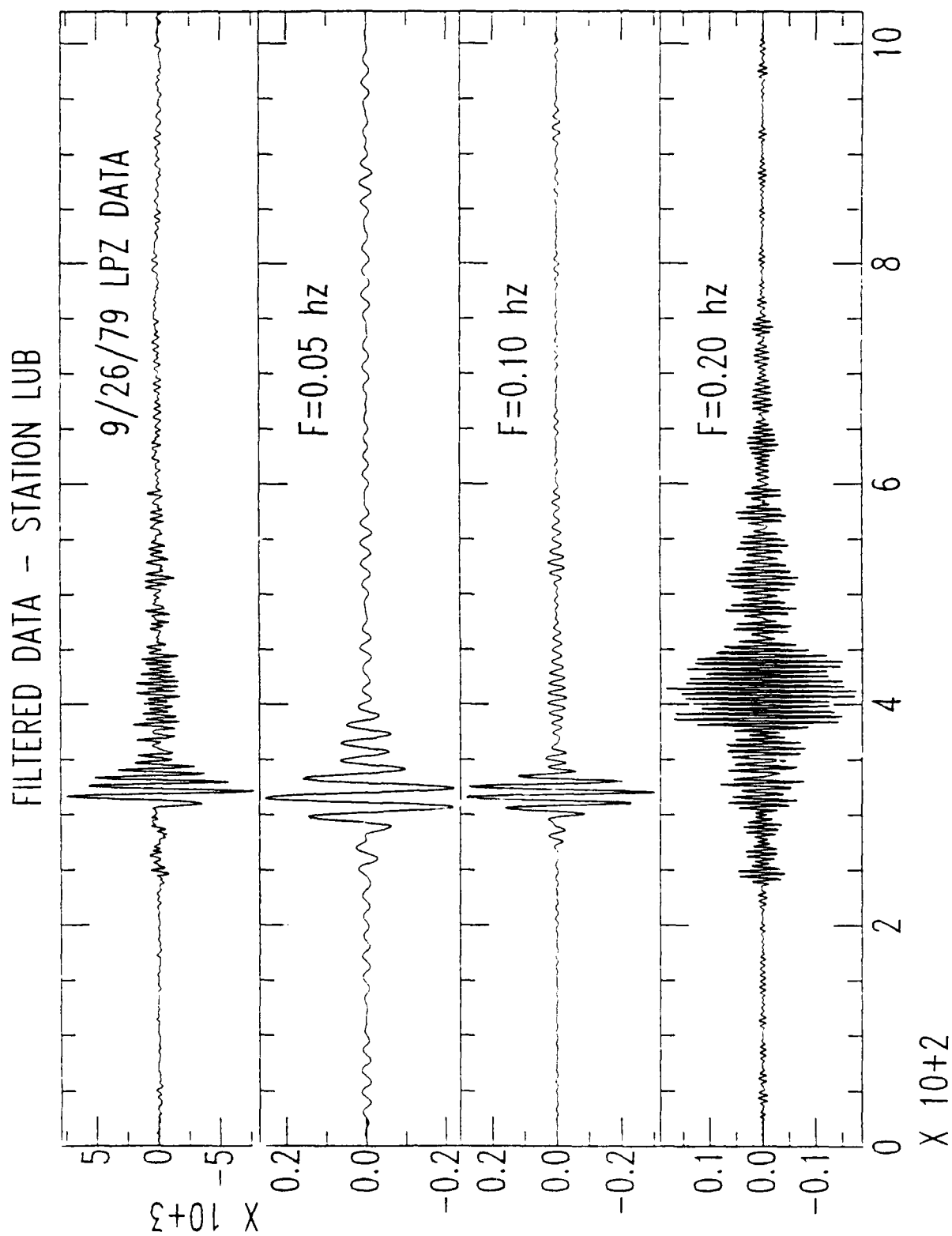


Figure 3

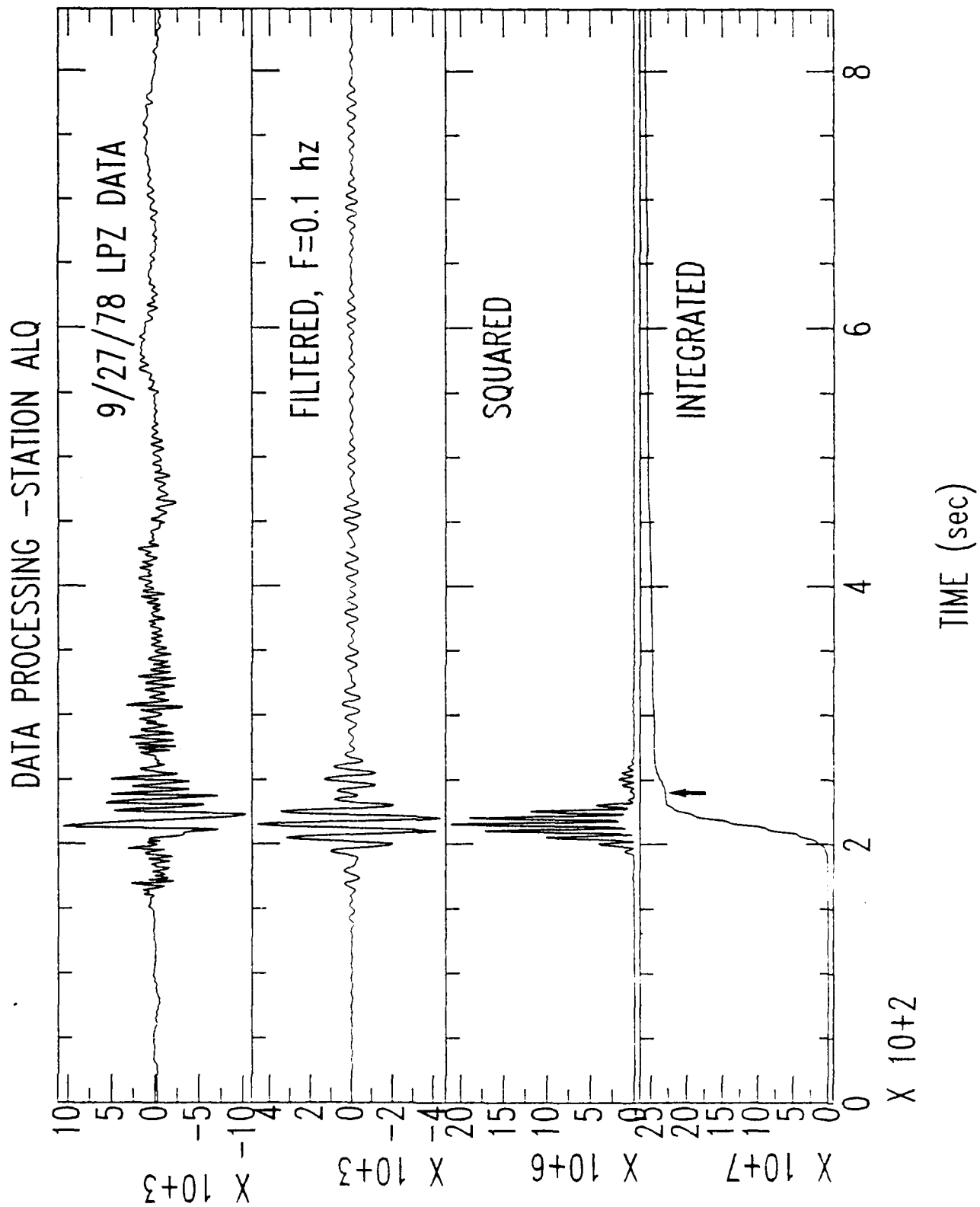


Figure 4

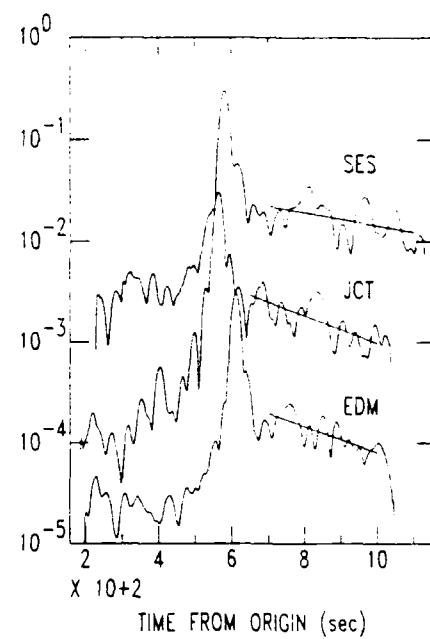
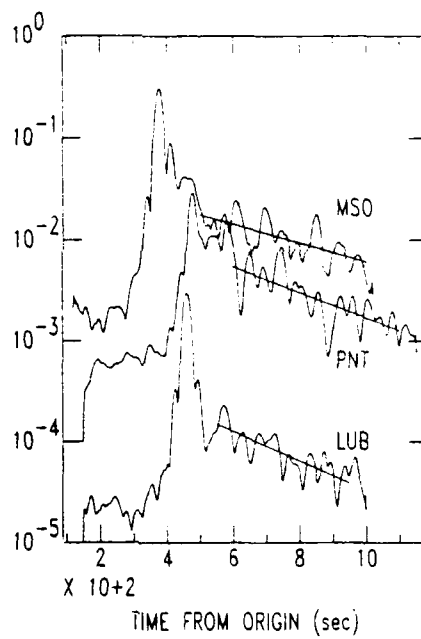
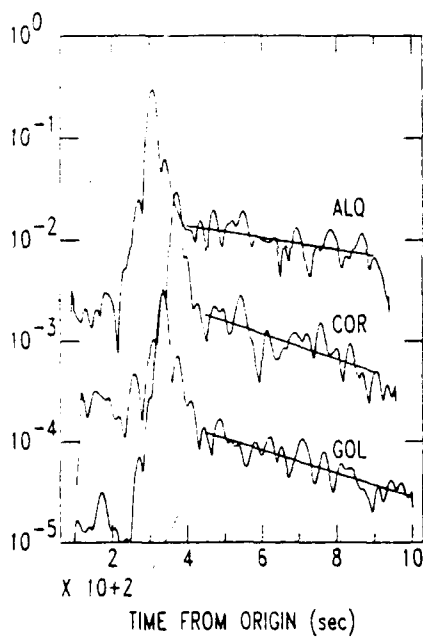


Figure 5

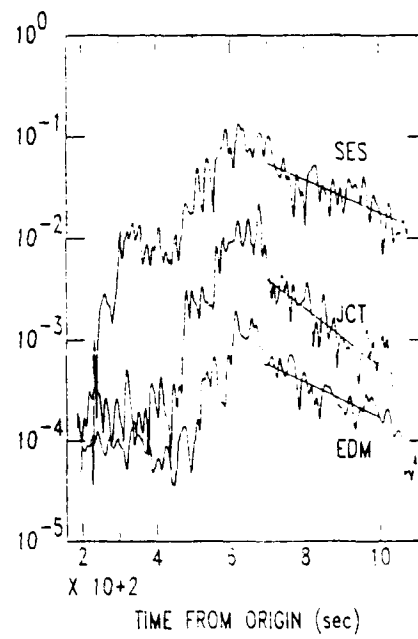
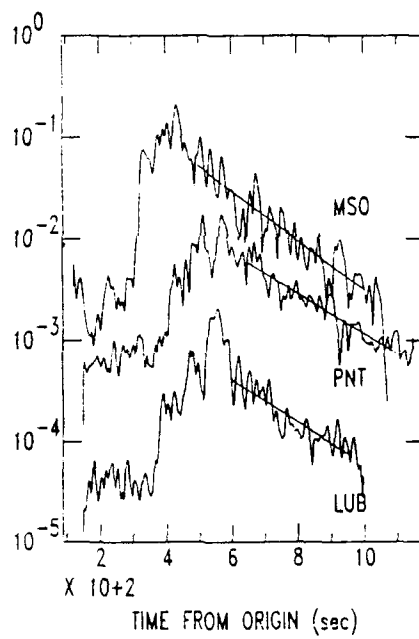
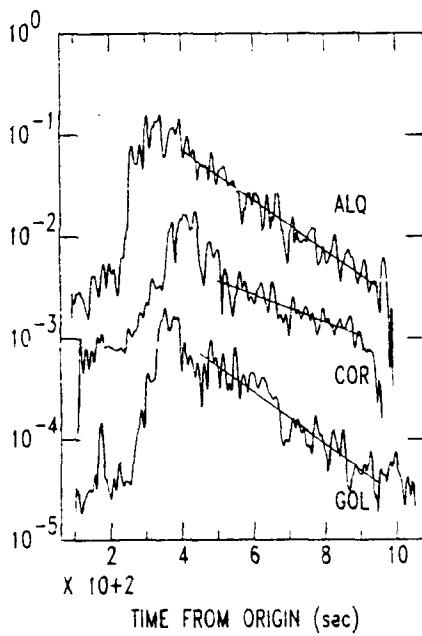


Figure 6

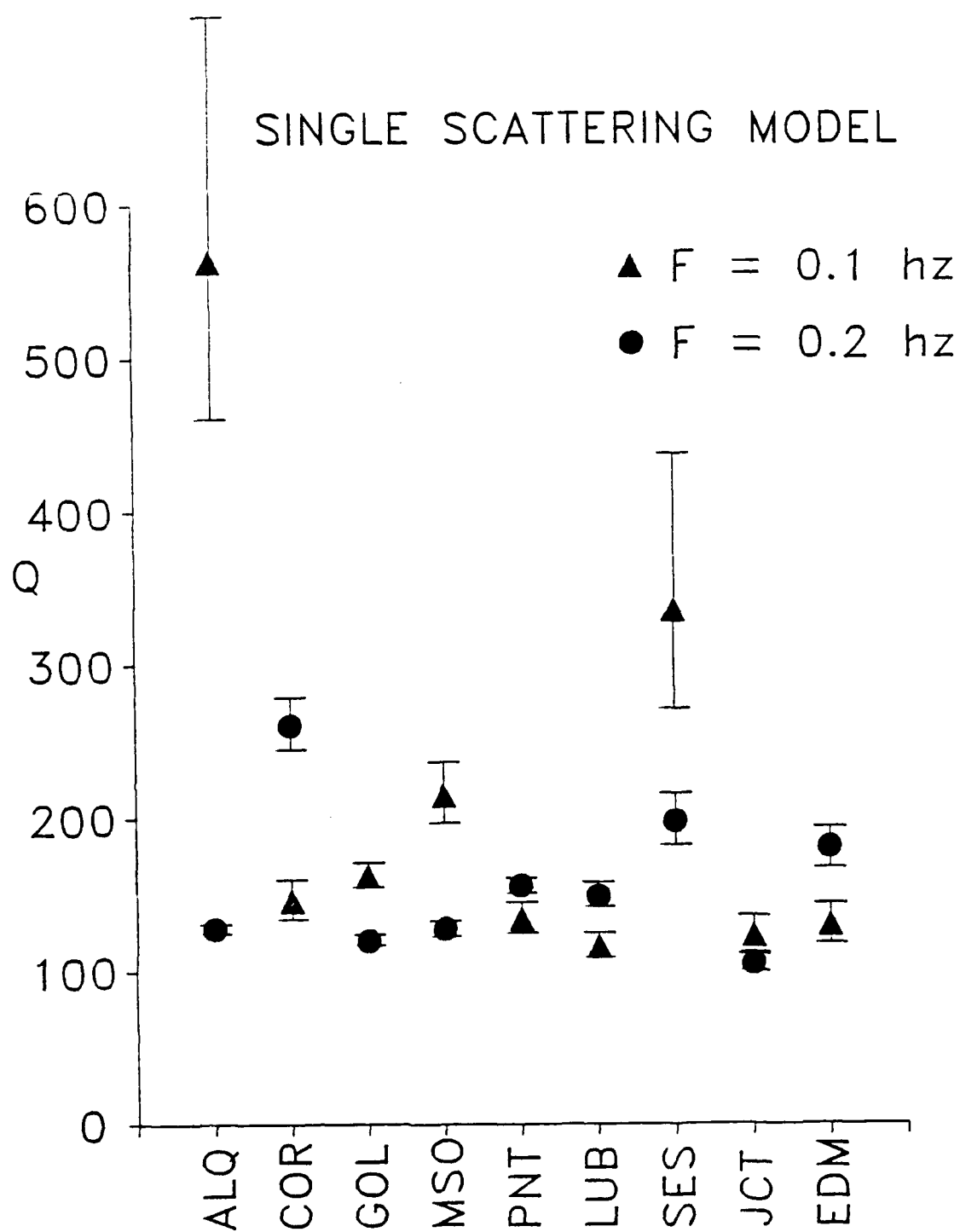


Figure 7

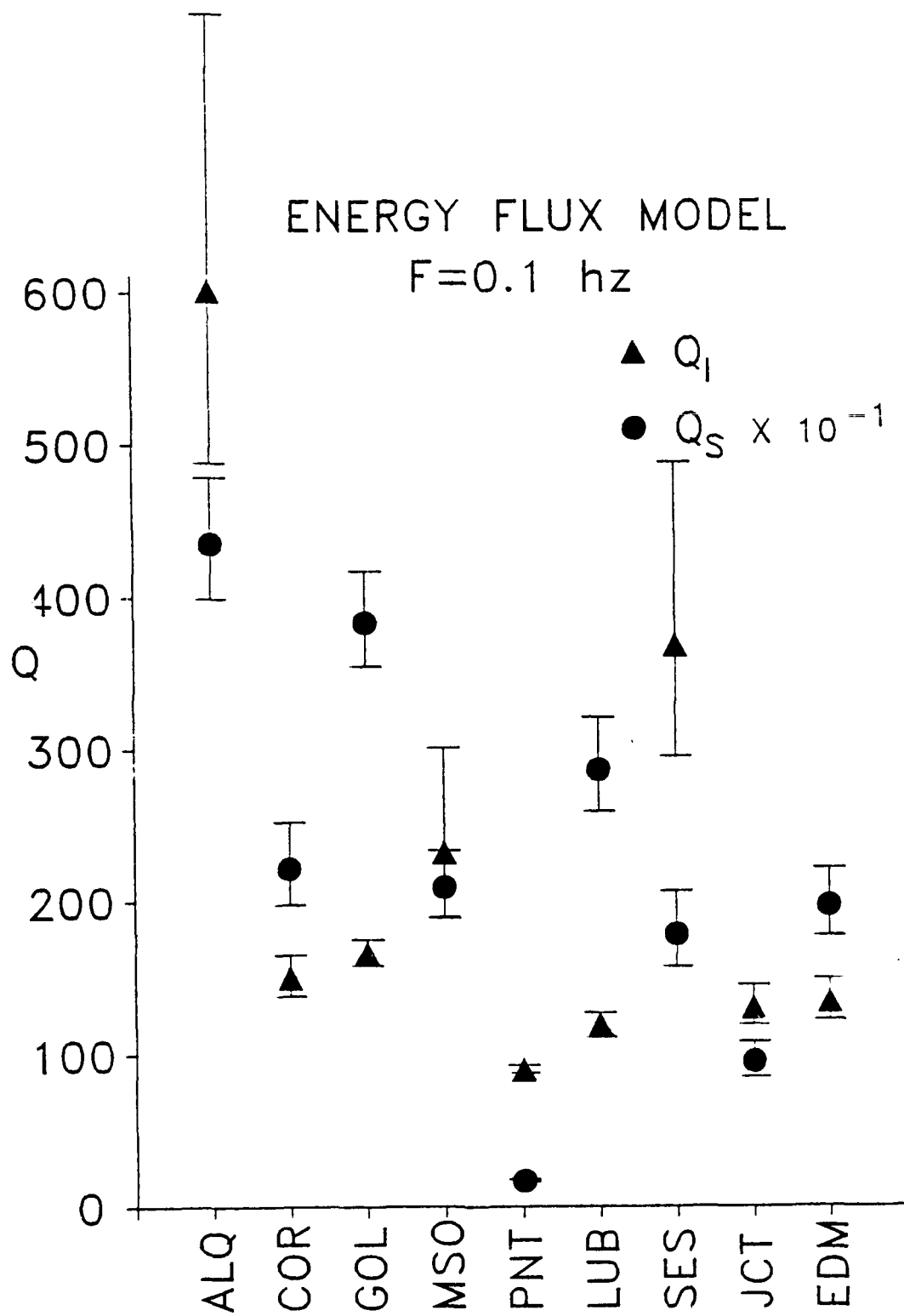


Figure 8

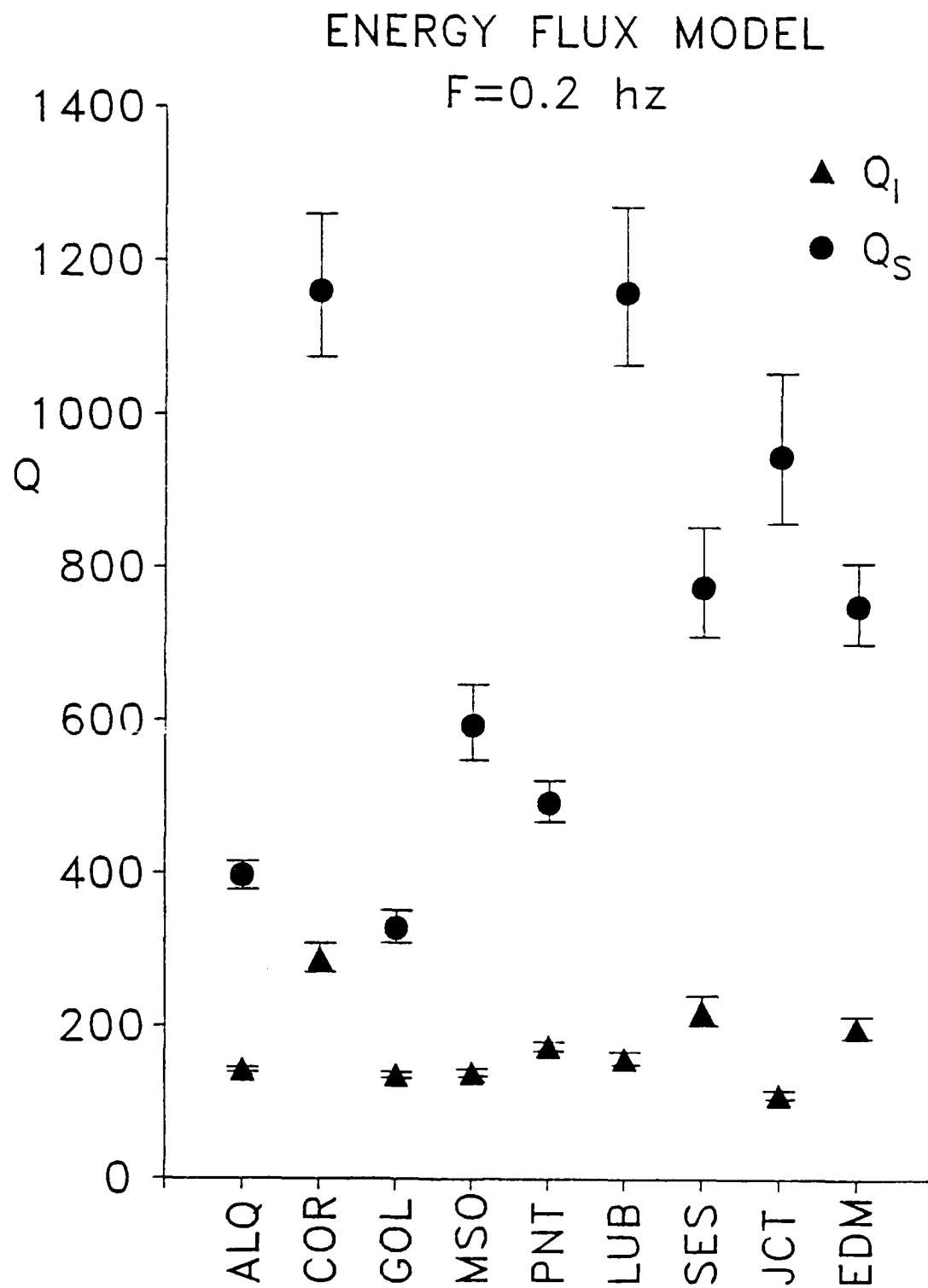


Figure 9

RADIATIVE DIFFUSION MODEL

$F=0.1 \text{ hz}$

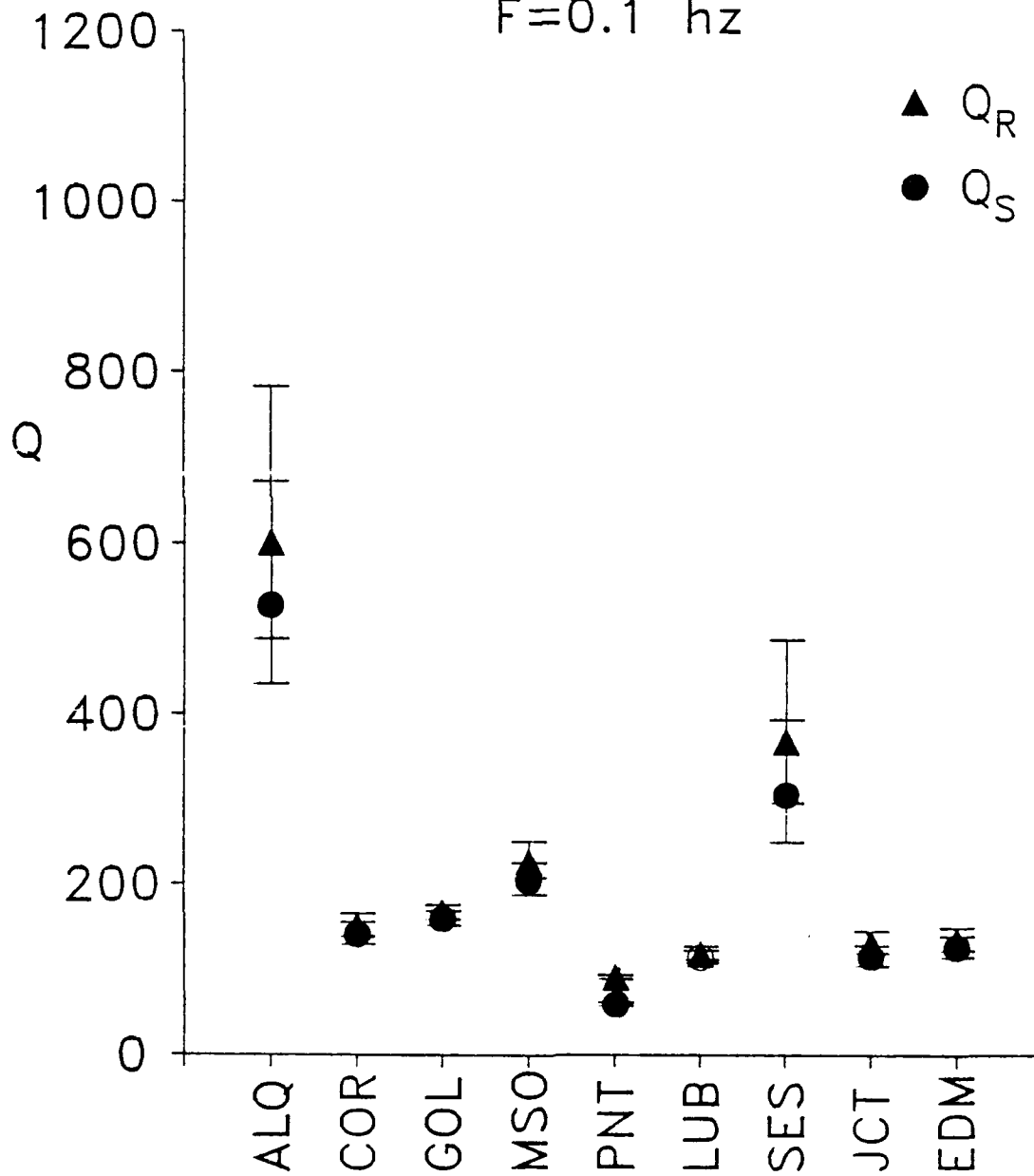


Figure 10

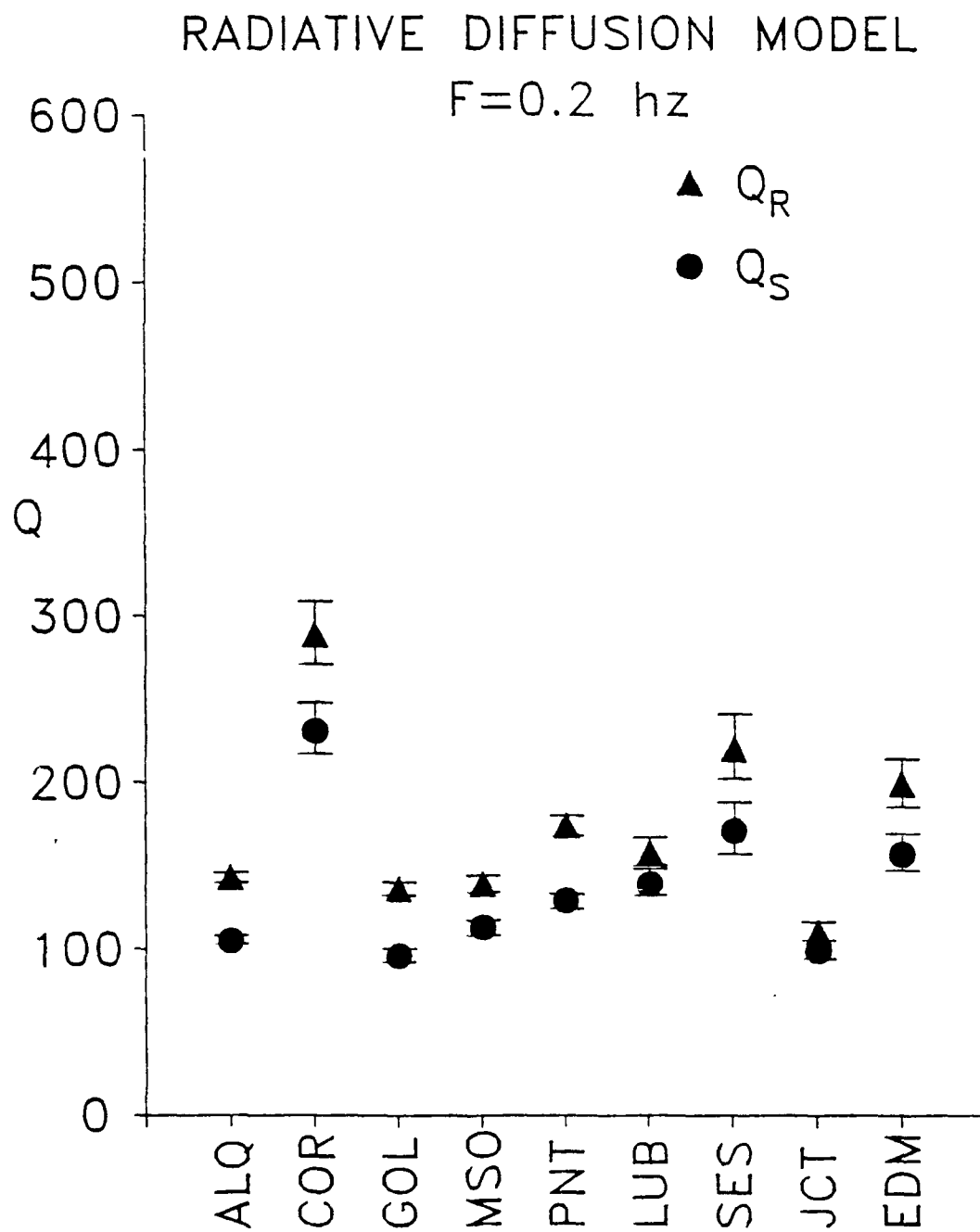


Figure 11

The Pennsylvania State University
The Graduate School
College of Earth and Mineral Sciences

Upper Mantle P-wave Velocity Structure Beneath Southern Africa
from P_{nl} Waves

A Paper in
Geophysics
by
Robert H. Clouser

Submitted in Partial Fulfillment
of the Requirements
for the Degree of
Master of Science
November 1988

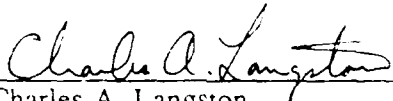
by Robert H. Clouser

I grant the Pennsylvania State University the nonexclusive right to use this work for the University's own purposes and to make single copies of the work available to the public on a not-for-profit basis if copies are otherwise unavailable.

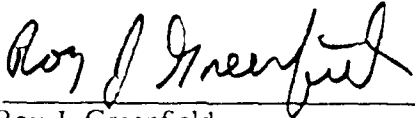
Robert H. Clouser

We approve the thesis of Robert H. Clouser.

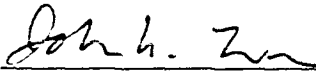
Date of signature:


Charles A. Langston,
Professor of Geophysics,
Thesis Advisor.

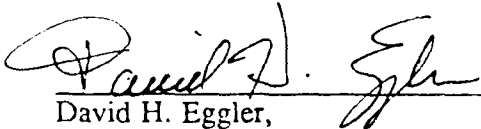
February 17, 1989


Roy J. Greenfield,
Professor of Geophysics.

Feb 20, 1989


John N. Louie, Assistant
Professor of Geophysics.

Feb. 21, 1989


David H. Eggler,
Professor of Petrology,
Chair of Graduate Program
in Geosciences.

Feb. 22, 1989

We approve the thesis of Robert H. Clouser.

Date of signature:

February 13, 1989

Charles A. Langston

Charles A. Langston
Professor of Geophysics.
Thesis Advisor.

Feb 13, 1989

Roy J. Greenfield

Roy J. Greenfield,
Professor of Geophysics.

February 14, 1989

John N. Louie

John N. Louie, Assistant
Professor of Geophysics.

ABSTRACT

P_{nl} waveforms from two moderate-sized earthquakes in Zambia are used to determine an upper mantle P-wave velocity model for southern Africa. The events are: 5/15/68, $m_b=5.7$, depth=28 km; and 12/2/68, $m_b=5.9$, depth=6 km. Focal parameters for these events are constrained by previous workers from teleseismic body wave inversion. Synthetic seismograms are generated for various mantle velocity models using a wavenumber integration method until an acceptable fit to the data is obtained. Quality of fit is measured primarily by the P_n/PL amplitude ratio. Source-station geometry also allows for the independent sampling of the upper mantle beneath the Kapvaal-Rhodesian craton and the mobile belt provinces. Synthetics from a three-layer crust over halfspace mantle model do not show prominent precursor arrivals seen in the data; these are interpreted to be P-waves turning in the upper mantle. The synthetics also give a too low P_n/PL amplitude ratio. Synthetics for models with a mantle P-wave velocity gradient of 0.00333/sec fit the cratonic path data very well. Since there is no indication of interaction with a low-velocity zone, this gives a minimum lithospheric thickness of 120 km. A slightly lower gradient is indicated for the mobile belt regions, with a minimum lithospheric thickness of 140 km. Though the data set is small, there is no evidence for a major low velocity zone beneath either province. Different velocity gradients between the two provinces implies different temperature structure, which supports the hypothesis that a deep, cool lithospheric root exists beneath the Kapvaal-Rhodesian craton.

CONTENTS

	Page
ABSTRACT	iii
LIST OF TABLES	v
LIST OF FIGURES	vi
ACKNOWLEDGEMENTS	vii
Sections	
1. Introduction	1
2. Geology and Tectonics of Southern Africa	3
3. Data and Analysis Method	6
4. Structure Modeling	12
5. Discussion	32
6. Conclusions	39
REFERENCES	42

LIST OF TABLES

Table	Page
I. Event Parameters	8
II. Crustal Model Parameters	13

LIST OF FIGURES

Figure	Page
1. Geologic province map of southern Africa	4
2. Events and station locations	7
3. Sample P_{nl} waveform	10
4. Vertical synthetics and data, Event 1, model LH01	15
5. Radial synthetics and data, Event 1, model LH01	16
6. Vertical synthetics and data, Event 2, model LH01	18
7. Gradient models SACM04 and SACM05	20
8. Ray parameter versus distance curves	21
9. Vertical synthetics and data, Event 1, SACM04	23
10. Radial synthetics and data, Event 1, SACM04	25
11. Vertical synthetics and data, Event 2, SACM04	26
12. Vertical synthetics and data, Event 1, SACM05	28
13. Radial synthetics and data, Event 1, SACM05	30
14. Vertical synthetics and data, Event 2, SACM05	31
15. Comparison of SACM04 and SACM05 with other models	38

ACKNOWLEDGEMENTS

I would like to thank Dr. Charles Langston for his patient help, guidance, and friendship during the time it took to complete this project. I would also like to thank Charles Ammon for his extremely helpful and pleasant discussions about seismology, or any topic for that matter, and for his supportive friendship. I would also like to thank Neal Nathman, Cynthia Miller, and Dan White for their friendship. Finally, I would like to thank the rest of the faculty, staff and students of the Geophysics program for making this department as friendly as it is.

This research was sponsored by the Defense Advanced Research Projects Agency through the Air Force Geophysical Laboratory under contract #F19628-87-K-0024.

INTRODUCTION

Determining seismic velocities in the uppermost mantle beneath southern Africa is important for constraining thermal, petrologic, and tectonic models of this region. Data from other areas indicate that upper mantle P-wave velocities and structure correlate with surface tectonic provinces and heat flow anomalies. For example, beneath stable shield regions, the upper mantle low-velocity zone (LVZ) is absent or weak, and P-wave velocity usually increases with depth (Brune and Dorman, 1963). The upper mantle in younger, active tectonic regions, like western North America, consists of a relatively thin "lid" (≈ 60 km thick) with a negative gradient or constant velocity, overlying a pronounced LVZ (Helmberger, 1972; Burdick and Helmberger, 1978). These variations arise from thermal effects related to the age of the most recent tectonism in the region, as well as lateral compositional heterogeneities in the upper mantle. Thus, data on upper mantle velocity structure yields information on thermal and petrologic properties and the depth extent of past tectonic events (Bott, 1982).

Efforts to determine the upper mantle and crustal structure in Africa have concentrated mainly on the East African rift. By comparison, work in southern Africa has been limited. Early studies, such as those done by Gane, et al. (1956), Hales and Sacks (1959), and Willmore, et al. (1952) examined crustal structure in the Transvaal using refraction experiments, but such attempts were generally limited to determining average crustal properties.

Studies of deeper structure have been performed using long-path surface wave

dispersion. Gumper and Pomeroy (1970) determined phase and group velocities over the length of the rift valley and central southern Africa. Though their study provides a useful crustal model for our synthetic computations, the upper mantle velocities are more representative of the rift system, or at best, an average between rifted and more stable regions. Bloch, et al. (1969) studied multi-mode surface wave dispersion in the same region of southern Africa examined in this study. Although his method is most sensitive to the shear wave velocity structure, we can compare our P-wave velocity model with their model.

Green (1978) determined an upper mantle P-wave velocity model for eastern and southern Africa by inverting P-wave travel times. However, the upper 250 km of his model is more representative of eastern Africa and the rift zone, because of the source-station distribution used. Only velocities below this depth can be compared with those from this study. Thus, little work has been done to directly determine the P-wave velocity structure above 250 km depth in southern Africa.

Several moderate sized earthquakes have occurred on the African continent since the initiation of the WWSSN network (Fairhead and Girdler, 1971). The objective of this study was to use some of these earthquakes to directly determine mantle P-wave velocity structure. We modeled P_n waves from two of these events located in Zambia, and recorded at southern African stations. Source parameters for these events have been well constrained by previous workers (Fairhead and Girdler, 1971; Wagner, 1986), so we can utilize the regional seismograms to obtain earth structure. Synthetics are calculated for various upper mantle models using a wavenumber integration algorithm, and compared to data to determine the upper mantle P-wave

velocity regime. Results are then compared with other models derived from different methods. We also examine the bearing that our derived velocity model has on the thermal state of the upper mantle in southern Africa.

GEOLOGY AND TECTONICS OF SOUTHERN AFRICA

Modern tectonism in Africa is confined mainly to the East African rift zone. Our study region lies south of this zone, though several lines of evidence indicate that the rifting is propagating southwestwards. Figure 1 is a geologic map of the study area, showing the mapped crustal provinces and their ages. The eastern portion of the area is dominated by the Precambrian Rhodesian and Kapvaal cratons, dated at greater than 2.7 Ga, separated by the slightly younger Limpopo mobile belt. These are thought to have acted as a tectonically undisturbed unit since the Archean. Surrounding this assemblage are the mostly younger platform sedimentary rocks of the mobile belts such as the Damara, Zambezi, Irumide, and Gariep belts. Kroner (1977) gives a thorough description of these African crustal provinces.

Several geophysical phenomena, generally regarded as evidence of rift propagation southwestwards, are notable in the region just north of our study area. Chapman and Pollack (1977) reported an anomalously high heat flow in western Zambia. Heat production measurements in the region indicate that near surface radioactivity can account for only half of the observed anomaly. They suggest that the excess heat comes from the asthenosphere, and that the lithosphere has been thinned to less than 60 km. Girdler (1975) described an extensive negative Bouguer anomaly over Africa. While most of the anomaly can be correlated with surface expressions of the

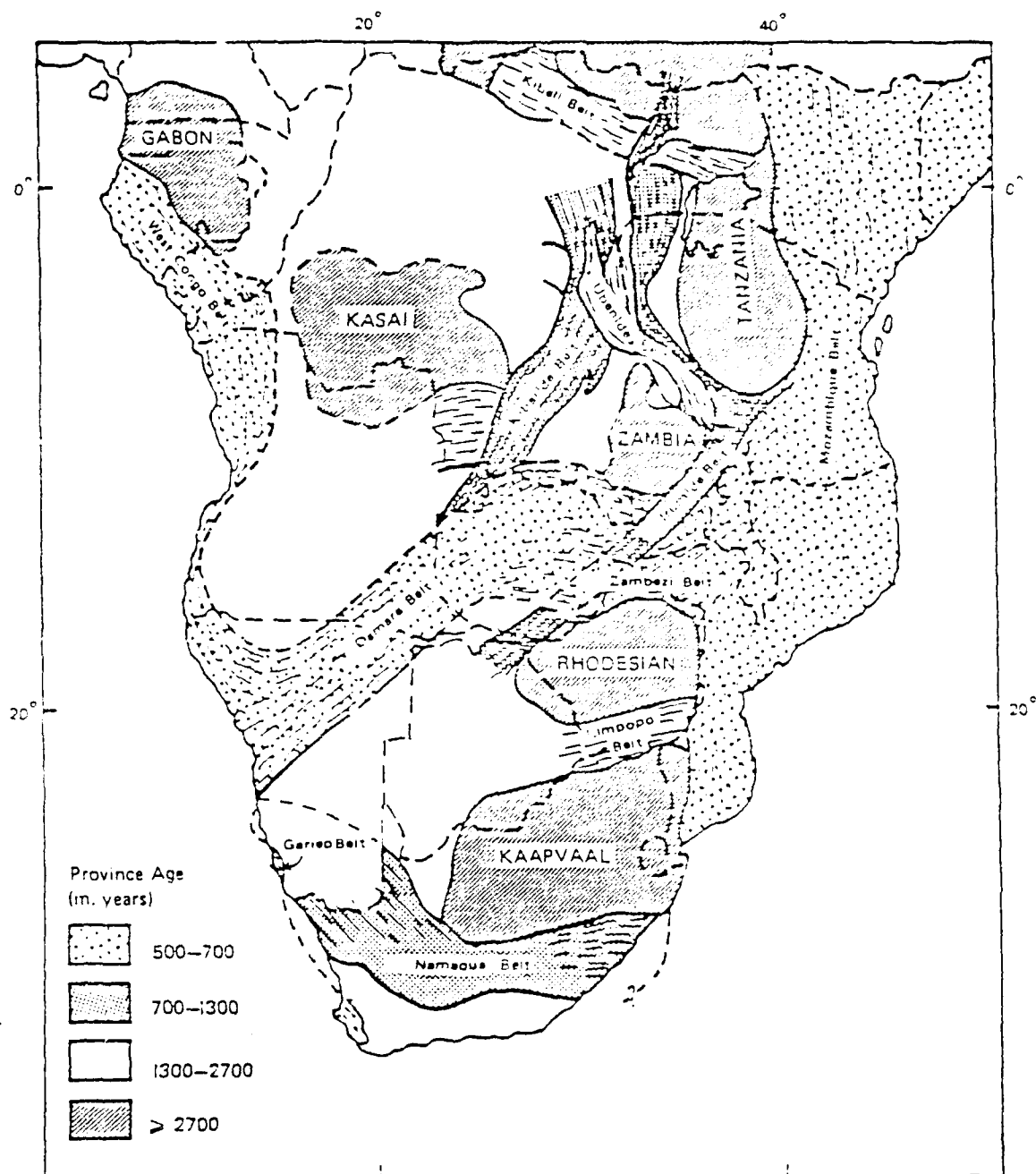


Figure 1. Geologic province map of southern and central Africa taken from Condie (1982). Events used in this study occurred in western Zambia. Note juxtaposition of old cratons and younger mobile belts. Our events occurred in western Zambia, along the Damara Fold Belt.

rift, an arm running east-west through northern Zambia and Angola can not. They attribute this to thinned lithosphere, with upwelling of hot, low density asthenosphere. de Beer, et al. (1975), noted an electrical conductivity anomaly in northern Botswana and Namibia, which they attribute to a highly fractured, conductive crust associated with incipient rifting, since part of the anomaly is continuous with surface expressions of the rift. In Botswana, Reeves and Hutchins (1975) detected a linear seismicity zone trending NE-SW. All these observations suggest instabilities in the lithosphere associated with rift propagation southwestwards.

Because of the lack of similar large-scale phenomena, thermal effects related to incipient rifting probably have little influence on mantle structure in southern Africa. However, one interesting observation in southern Africa, unrelated to rifting, further motivates this study. In addition to determining the upper mantle P-wave velocity structure, we hoped to detect possible differences in upper mantle structure beneath the cratons and mobile belts. This idea comes from a paper by Ballard and Pollack (1987), who described a difference in observed heat flow between the cratonic and mobile belt provinces. They cite reasons for this as: 1) differences in crustal heat production between the two provinces, and 2) diversion of heat into the mobile belts by a deep, cool lithospheric root beneath the craton. Their models indicate that at least 50% of the difference may be attributable to diversion of heat, with the root extending from 200 km to 400 km depth.

Such a deep, cool root may have a velocity structure different from that of the surrounding hotter sub-mobile belt mantle, and this may be detectable in seismic data. Pressure effects and composition being equal between the two regions,

velocities in the hotter upper mantle should be lower than in the cooler lithospheric root (Bott, 1982). For a homogeneous upper mantle, a temperature gradient of more than 8 to 9 K/km would offset the pressure effect, causing P-wave velocities to decrease (Anderson and Sammis, 1970). Thus, the velocity gradient determination can help constrain the mantle temperature gradient. Fortunately, the events and stations used in this study are well situated to address this question. A glance at Figure 2 shows that raypaths from the two Zambia events cross either mostly cratonic or mostly mobile belt provinces, allowing for independent sampling of the two regions. So our results could corroborate the deep cratonic root hypothesis.

DATA AND ANALYSIS METHOD

The objective of this study was to determine an upper mantle P-wave velocity structure for southern Africa. Our approach was to forward model regional P_{nl} waveforms recorded at several stations from two moderate-sized earthquakes in Zambia. Figure 2 shows the locations of the events, stations, and raypaths. The effects of lateral crustal heterogeneities on the PL waveform were ignored; these would cause focusing and defocusing, as well as scattering, of PL energy. Forward modeling of body waves has not previously been applied in this region. The advantage is that this technique samples upper mantle properties on a finer scale than surface wave methods.

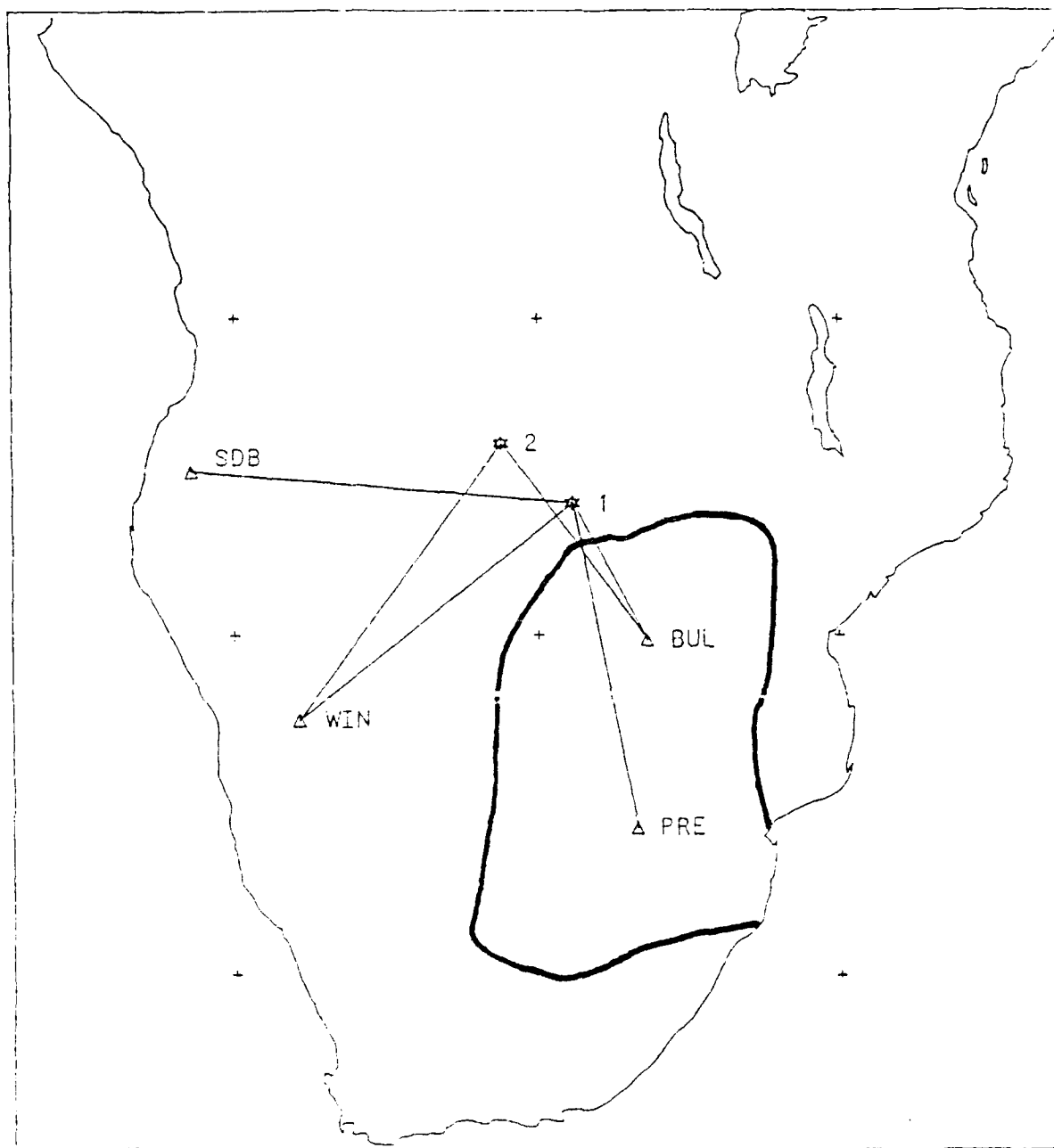


Figure 2. Events and stations used in the study. Shown are raypaths from each event to stations providing data for that event. Region enclosed by bold line is the Kapvaal-Rhodesian craton. Note that raypaths to BUL and PRE cross only craton; those to WIN and SDB cross only mobile belts. Tick marks are 10° apart.

TABLE I: Event Parameters

Event	Date	Strike	Dip	Rake	m_b	$M_o (\times 10^{24} \text{ dyne-cm})$	Depth (km)
1	5/15/68	49°	40° SE	263°	5.7	3.32	28
2	12/2/68	20°	40° SE	265°	5.9	4.38	6

Table I summarizes the source parameters for the two events used, as determined by Wagner (1986) from moment tensor inversion. Event 1 occurred in western Zambia on May 15, 1968. Inversion gave a nearly pure, high-angle normal fault mechanism at 28 km depth, with a large (17%) CLVD component, and a 5 sec source time function. A large earthquake this deep implies a high strain rate at depth lending support to the rift propagation hypothesis. Event 2 occurred 350 km northwest of Event 1. Inversion yielded a nearly pure normal mechanism, with a small CLVD component and 7 sec time function, at a depth of 6 km. All four stations (PRE, BUL, WIN, SDB) contributed data for Event 1, while only BUL and WIN provided data for Event 2.

A P_{nl} wave is defined as the long-period waveform recorded at regional distances (<1700 km or 15°) from crustal earthquakes, though it has been observed out to 25° in some regions. It includes the initial P pulse and lasts until the shear wave arrival time. P_{nl} has been studied by Wallace (1983), Shaw and Orcutt (1984), and Helmberger and Engen (1980). Figure 3 shows a sample P_{nl} waveform from an earthquake in Zambia (this study). The name P_{nl} , as coined by Helmberger and Engen (1980), implies that the waveform is a combination of two wave phenomena: a partially trapped crustal wavetrain (PL), and upper mantle phases (P_n).

The P_n portion of the waveform (not to be confused with the mantle head wave phase P_n) arrives first, and consists of P-wave interactions with the uppermost mantle, such as the similarly named mantle head wave, and upper mantle turning wave phases such as P , pP , and sP (if these phases exist). For a plane layered earth, these phases travel with horizontal phase velocities greater than or equal to the P-velocity at the top of the mantle. In Figure 3, the first three impulsive arrivals (open arrows) constitute P_n . Thus, because it is composed of P-waves that sample the uppermost mantle, this portion of P_n is the most important for this study.

PL is the long-period wavetrain that follows P_n in Figure 3. It was first identified by Somville (1930), and has since been studied by numerous workers (Oliver and Major, 1960; Oliver, 1964; Helmberger, 1972; Helmberger and Engen, 1980; Wallace, 1983; Shaw and Orcutt, 1984). It propagates as partially trapped P-SV reverberations in the crust, leaking SV energy into the mantle, a phenomenon termed "leaky mode" propagation, hence explaining why PL attenuates rapidly with distance. These reverberations have ray parameters greater than the P-wave slowness of the uppermost mantle. Particle motion for the PL wave is prograde elliptical. Shaw and Orcutt (1984) examined PL in great detail using wavenumber integration, revealing that it is most sensitive to crustal thickness and average crustal velocity, and that structure beneath the crust has very little effect on PL. This is important, since we can therefore examine mantle effects on P_n without significantly affecting PL.

The top and bottom of the data seismograms were digitized from 70mm film strips, averaged, and linearly interpolated to a 0.15 sec sampling interval. These were then rotated to their best azimuths to obtain radial and tangential components. In all

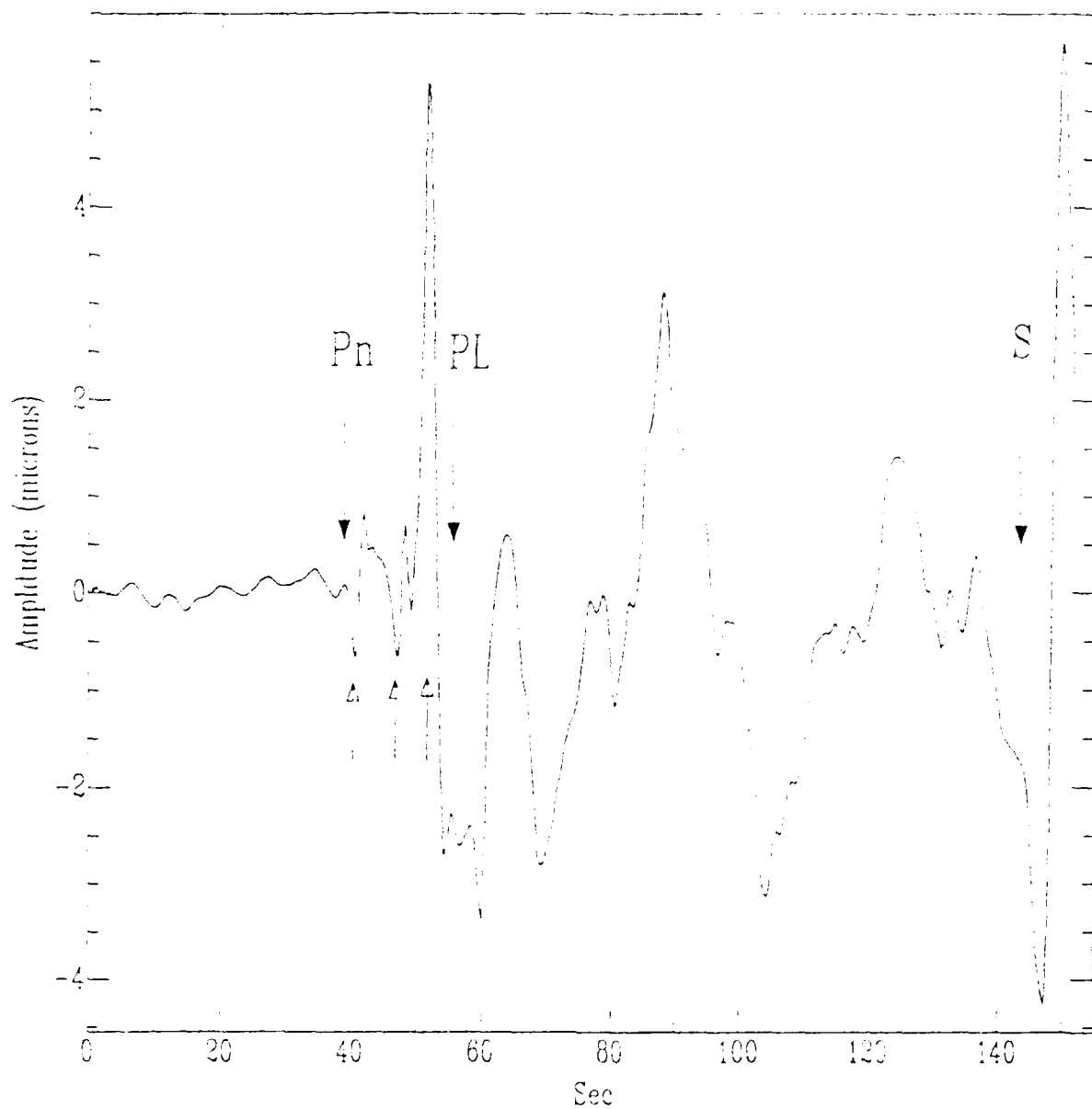


Figure 3. Sample P_n waveform (vertical component) from a crustal earthquake (28 km depth) in Zambia, recorded at PRE ($R=1100$ km). Onset of P_n , PL, and S is indicated. The three open-arrowed impulsive arrivals constitute P_n , and propagate in the uppermost mantle. PL is the long-period wavetrain following P_n and ending at the S arrival.

cases, the tangential motion was negligible, implying that little multi-pathing energy was present.

To generate synthetic seismograms we used the wavenumber integration routine from Barker (1984). This method stems from the solution in cylindrical coordinates of the Fourier transformed (Helmholtz) wave equation. The frequency domain solutions for the P-, SV-, and SH-wave potentials are:

$$\begin{aligned}\bar{\phi}(r, \theta, z; \omega) &= \sum_l A(l, \theta) \int_0^{\infty} \phi_l(z; k, \omega) J_l(kr) dk \\ \bar{\psi}(r, \theta, z; \omega) &= \sum_l A(l, \theta) \int_0^{\infty} \psi_l(z; k, \omega) J_l(kr) dk \\ \bar{\chi}(r, \theta, z; \omega) &= \sum_l A(l, \theta) \int_0^{\infty} \chi_l(z; k, \omega) J_l(kr) dk\end{aligned}$$

in which the azimuthally dependent terms $A(l, \theta)$ are the horizontal source radiation pattern, $J_l(kr)$ is the Bessel function of order l , k is the wavenumber ($= \omega/c$), ω is angular frequency, c is horizontal phase velocity, and (r, θ, z) are the cylindrical coordinates. Notice that since the integration is over real wavenumber, this method will theoretically produce a complete synthetic seismogram. In practice, however, the integration is truncated, so that the final response includes only waves over a wavenumber band of interest.

The vertically dependent functions ϕ_l , ψ_l , and χ_l in the integrand are computed using the Thomson-Haskell propagator matrix method (Thomson, 1950; Haskell, 1953) for a layered medium. A point dislocation source is included by incorporating

displacement-stress discontinuities at the source depth. Also included is the delta matrix formulation of Duncan (1965) and Thrower (1965) to avoid precision errors when subtracting exponentially growing terms for the P-SV case. Frequency-independent attenuation (Q^{-1}) is included by assuming complex layer velocities.

The integration over wavenumber is performed following Apsel (1979), where a quartic polynomial is fit to the integrand, and the integration performed analytically over that polynomial. Inclusion of complex velocities allows for integration over real wavenumber, since this moves the Rayleigh poles off the real wavenumber axis. The sampling can be coarse where the integrand varies slowly, and finer where it varies rapidly.

Finally, the frequency domain Green's functions for the principal dislocation sources are obtained. These are then multiplied with the source spectrum, a WWSSN long-period instrument response, combined to yield a synthetic spectrum, and inverse Fourier transformed into the time domain.

STRUCTURE MODELING

All models for which synthetics were calculated had the same crustal parameters, but different mantle structure. For the crustal model we chose model C3 from Pavlin (1981), which is a modified version of the Gumper and Pomeroy (1970) crustal model. Parameters of this crust are shown in Table II. In his inversion for source parameters of African earthquakes, Wagner (1986) used a variation of this model. His source crustal thickness was 36 km for the two events in this study, slightly less than our 38 km thick crust. For attenuation, an arbitrary Q_P and Q_S of

1000 and 500, respectively, were assigned to the crust.

TABLE II: Crustal Model

α (km/sec)	β (km/sec)	ρ (g/cc)	QP	QS	Thickness (km)
5.90	3.35	2.70	1000	500	7.0
6.15	3.55	2.80	1000	500	11.0
6.60	3.72	2.85	1000	500	20.0

The first model for which synthetics were calculated is called LH01. It has a half-space mantle with a constant P-wave velocity of 8.10 km/sec, and a mantle shear wave and density structure taken from Bloch, et al. (1969). Representative values for QP and QS of 500 and 200, respectively, were assigned to the upper mantle. Because of the lack of any mantle velocity gradient, the P_n portion of P_n will contain only head wave phases: i.e., waves which refract along the Moho. In all subsequent data and synthetic comparison figures, the data is the thinner trace, the station name, azimuth, and distance are given, and absolute amplitudes are shown in microns (data is the upper number). Both synthetics and data have been low-pass filtered using a Butterworth filter and corner frequency of 0.8 hz.

Of primary importance when comparing the synthetics and data is the relative amplitudes of the P_n and PL portions in the waveforms, which we represent as the ratio of the amplitude of the large arrival at 30 sec (referred to as $P_n A$) in the figures to the amplitude of the early PL oscillations. This ratio is referred to as the $P_n A / PL$ ratio. For a constant velocity mantle, the $P_n A / PL$ ratio in the synthetics is a minimum, since only head wave and crustal phases contribute to $P_n A$. The $P_n A / PL$

ratio will increase for models with a positive mantle gradient, because turning wave energy will contribute to P_nA . Hence, the P_nA/PL ratio is a measure of the upper mantle influence on P_n , without recourse to absolute amplitudes.

Figure 4 shows the vertical data and synthetics for Event 1 and model LH01. All waveforms have been aligned on the P_nA arrival at 30 sec. Data from BUL has long-period noise, so P_nA/PL amplitude ratio may be inaccurate. From calculations using generalized ray theory, the first arrival in these synthetics is the mantle head wave (P_n), and the second arrival (P_nA) is composed of similar head waves from depth phases like pP_mP and sP_mP . Notice that, particularly at BUL and PRE, the P_nA/PL ratio is underestimated in the synthetics. At WIN the misfit is not as great, but still obvious. The synthetic and data P_nA/PL ratio at SDB are very similar, in contrast to the other data. Based on the nature of P_nA , these misfits (except for SDB) indicate that there is mantle turning wave energy in the data, which is not included in the synthetics.

Also observe that the synthetics do not show either of the dilatational precursor arrivals seen at PRE (arrowed in Figs. 4 and 5). Furthermore, the synthetic P_nA-PL time is too small (i.e., P_nA arrives late), indicating that overall mantle velocities are too low. A positive velocity gradient could increase the P_nA/PL ratio by including turning wave energy in the synthetics, as well as producing discrete arrivals. Based on these criteria, we believe that a model with a positive mantle P-wave velocity gradient is required.

Figure 5 shows the radial components for Event 1 and model LH01. P_nA/PL

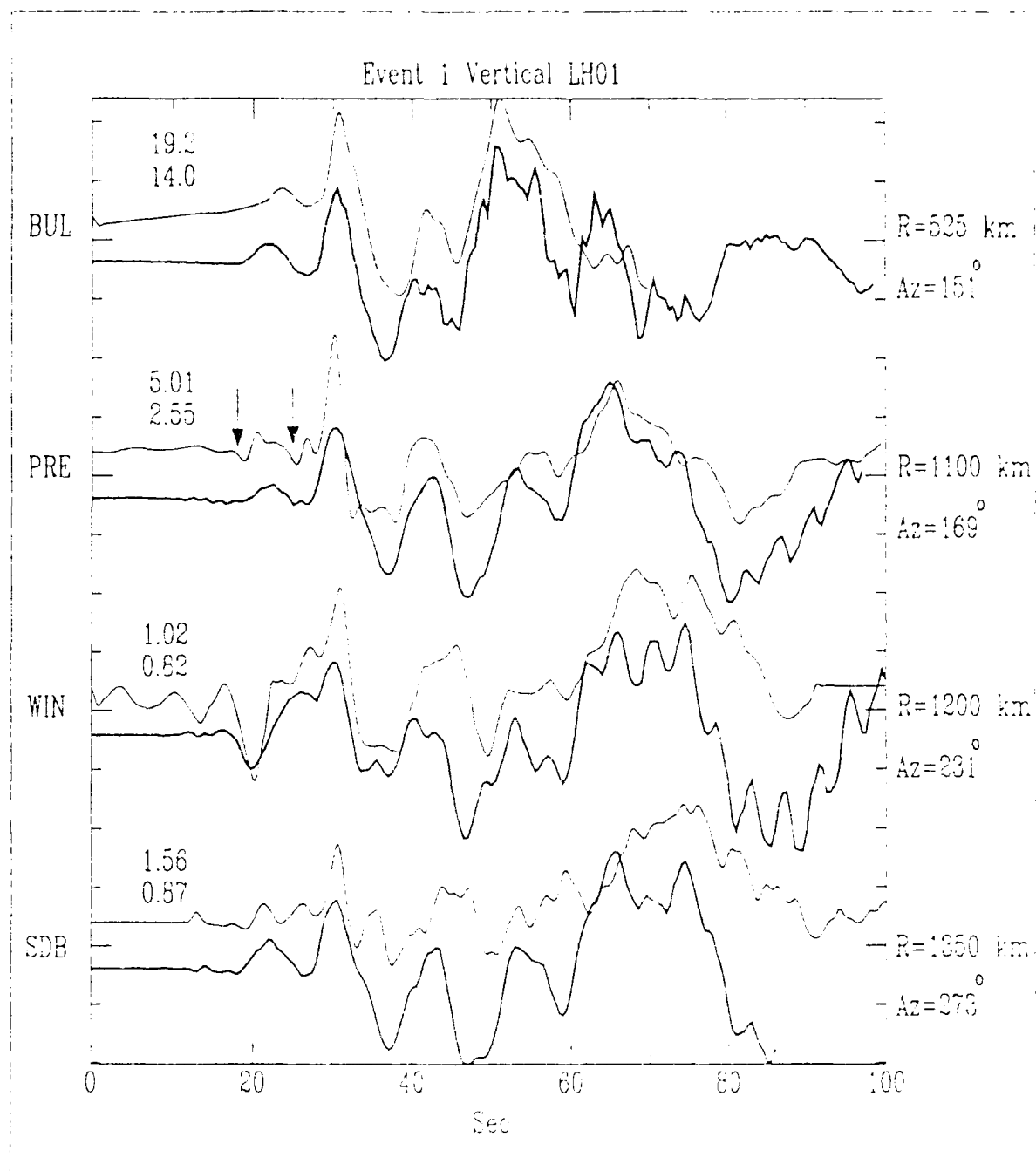


Figure 4. Vertical data (thin traces) and synthetics (thick) for Event 1, model LH01 (constant velocity mantle). Note long-period noise at BUL. Traces have been offset vertically to facilitate comparison, and aligned on the P_nA phase at 30 sec. Distance, azimuth, and absolute amplitudes (microns) are given. This format is followed in all subsequent figures. Notice the consistent P_nA/PL ratio at all stations except SDB. Precursor phases (arrowed) at PRE are not produced in the synthetic.

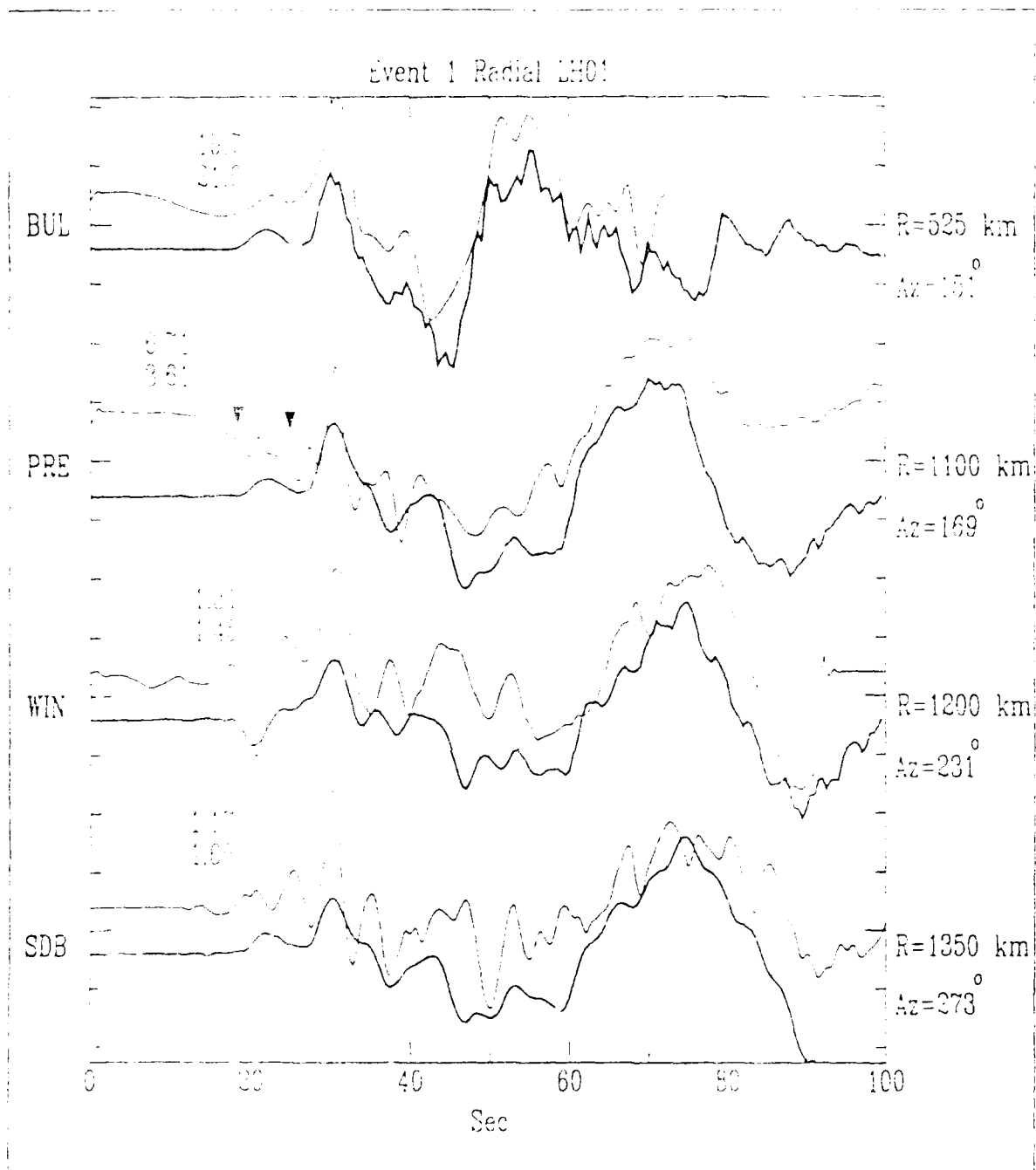


Figure 5. Radial data and synthetics for Event 1, model LH01. Long-period noise in the BUL and PRE data preclude meaningful $P_n A/PL$ ratio estimates, but the missing precursors seen in the PRE data indicate that a positive gradient is needed. WIN $P_n A/PL$ ratio also indicates that a positive mantle gradient is required. The $P_n A/PL$ ratio for both components of the SDB data is useless due to instrument problems.

ratios for BUL and PRE are unreliable because of the long-period noise. Therefore, one can not safely say that the synthetic $P_n A/PL$ ratio at these stations is too small. This is clearly the case at WIN and SDB, though. Furthermore, the precursor phases at PRE are missing in the synthetics. Thus, we arrive at the same conclusion as for the vertical components: neither the $P_n A/PL$ ratios nor the precursor phases at PRE can be modeled with a constant velocity mantle. This can only be accomplished by incorporating a positive mantle velocity gradient in the model.

In subsequent comparison figures, the radial components will not be discussed in detail, because the P_{nI} data behave as expected for P-SV waveforms. In general, P_n phases are larger on the vertical than on the radial, and the reverse is true for the early part of the PL wave (composed of shallowly incident energy).

However, the SDB data presents an anomalous $P_n A/PL$ ratio on the radial component. Here, $P_n A$ is much larger than PL, while the vertical $P_n A$ is much smaller than PL, a relation not seen in the other data. Because of the low signal-to-noise ratio and lack of calibration pulses on the original seismogram, we consider the SDB $P_n A/PL$ ratio unreliable. However, P_n will be useful later when comparing synthetics from different mantle gradient models.

Shown in Figure 6 are synthetics from model LH01 and data for Event 2. Radial components are not available for BUL due to horizontal instrument malfunction. As in the Event 1 comparisons, we see that the synthetic $P_n A/PL$ ratio is underestimated at BUL and WIN. The first arrival at WIN is much smaller than that seen in the data, and the interference between the first two arrivals in the data (arrowed in

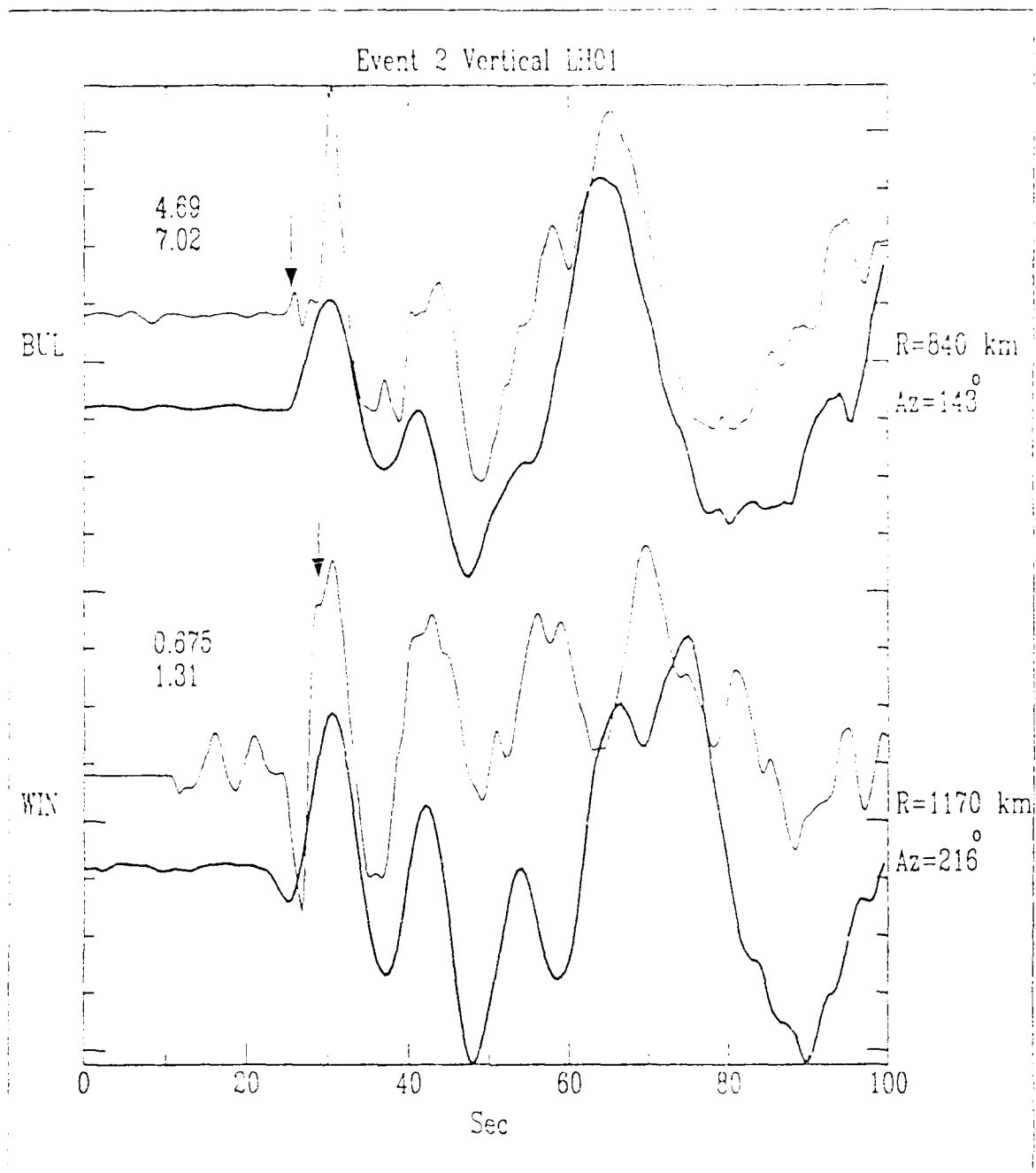


Figure 6. Vertical component data and synthetics for LH01 and Event 2. Note underestimated $P_n A/PL$ ratio at both stations, indicating the need for a positive mantle gradient. First arrival at BUL (arrowed) is not in the synthetics, and hence is thought to be a turning wave. Note shoulder at WIN (arrowed) from interference of first two arrivals.

Fig. 6) is not modeled. At BUL, notice that the first arrival (compressional, arrowed in Fig. 6) is missing in the synthetics, just as the precursor phases at PRE for Event 1 were missing, and we similarly infer this to be a turning P-wave. We again infer that a mantle gradient model would correct these misfits.

Figure 7 shows such a model, called SACM04 (and a higher gradient model, SACM05, to be discussed later). The crustal parameters are the same as those in LH01; the mantle now has an arbitrarily chosen linear P-wave velocity gradient of 0.00333/sec, with a Moho velocity of 8.10 km/sec, and a QP and QS as before. For the synthetic computations, this gradient was approximated by 10 km thick layers, each with a velocity increase of 0.0333 km/sec. The mantle density and shear velocity are the same as those in LH01, and P_n is insensitive to the mantle shear velocity. Shaw and Orcutt (1984), in a detailed analysis of PL propagation across Tibet, showed that PL is insensitive to mantle structure. Thus, P_n (or $P_n A$) can be used to estimate the gradient magnitude. Finally, the earth flattening transformation used in Helmberger (1973) was applied to the entire model.

The number of layers needed in the wavenumber integration to adequately model turning waves was found from direct P-wave bottoming depths at the closest station from ray parameter-distance curves. Such curves were determined for both events, and the curve for Event 1 is shown in Figure 8. For any station distance, the ray's slowness is the reciprocal of the velocity at its bottoming depth. For example, at 1350 km, the distance of SDB, the slowness is 0.1026 sec/km; this gives a velocity of 8.72 km/sec, and reference to SACM04 gives a bottoming depth of 160 km for P. Thus, if SACM04 was the best fit model for SDB, it would be representative of the

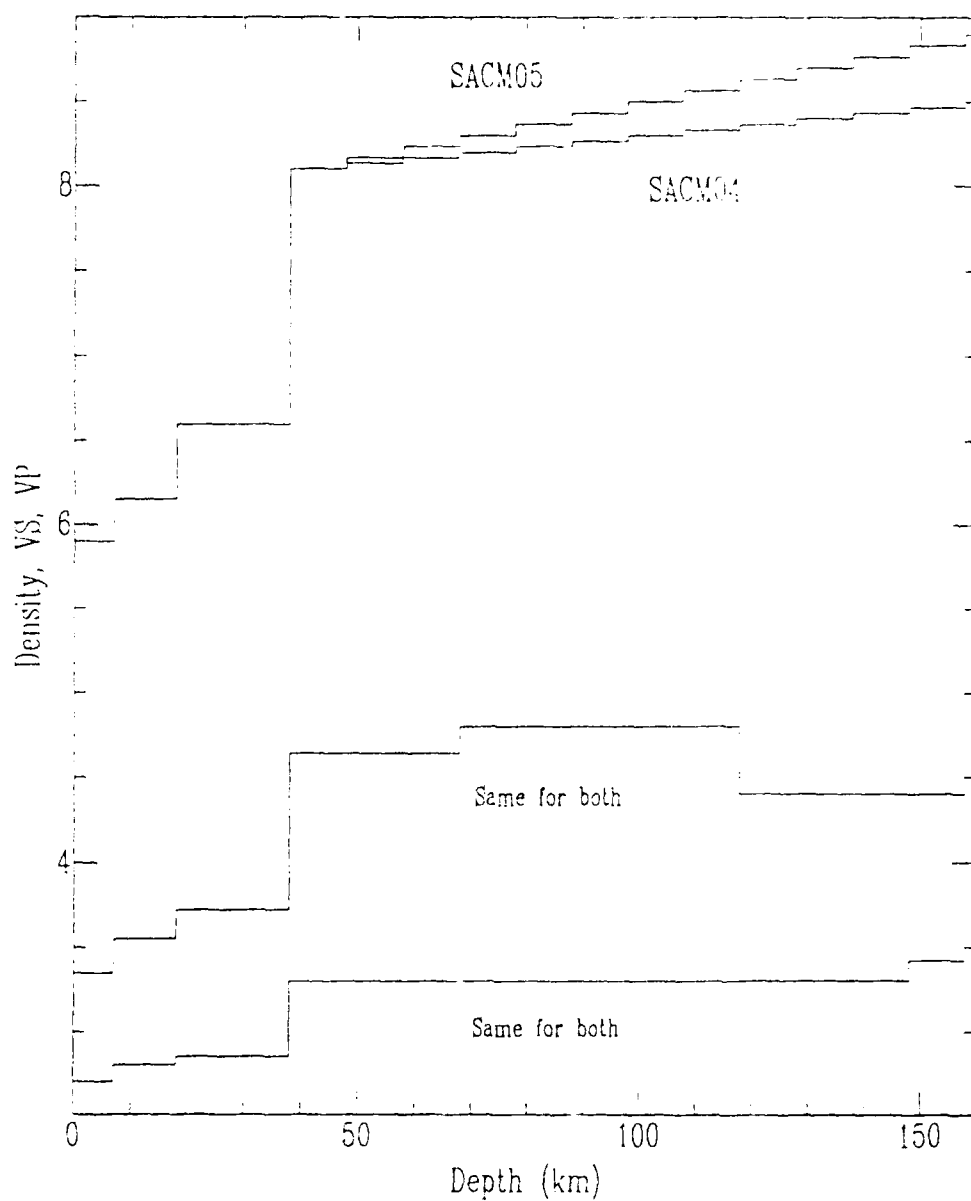


Figure 7. Models SACM04 and SACM05, for a spherically stratified earth. SACM04 has a mantle P-wave velocity gradient of 0.00333/sec; SACM05 has a gradient of 0.00666/sec, represented by 10 km thick layers. Crustal parameters are taken from model C3 of Pavlin (1981), and are a modification of those from Gumper and Pomroy (1970). Mantle shear velocity structure and density are taken from Bloch, et al. (1969).

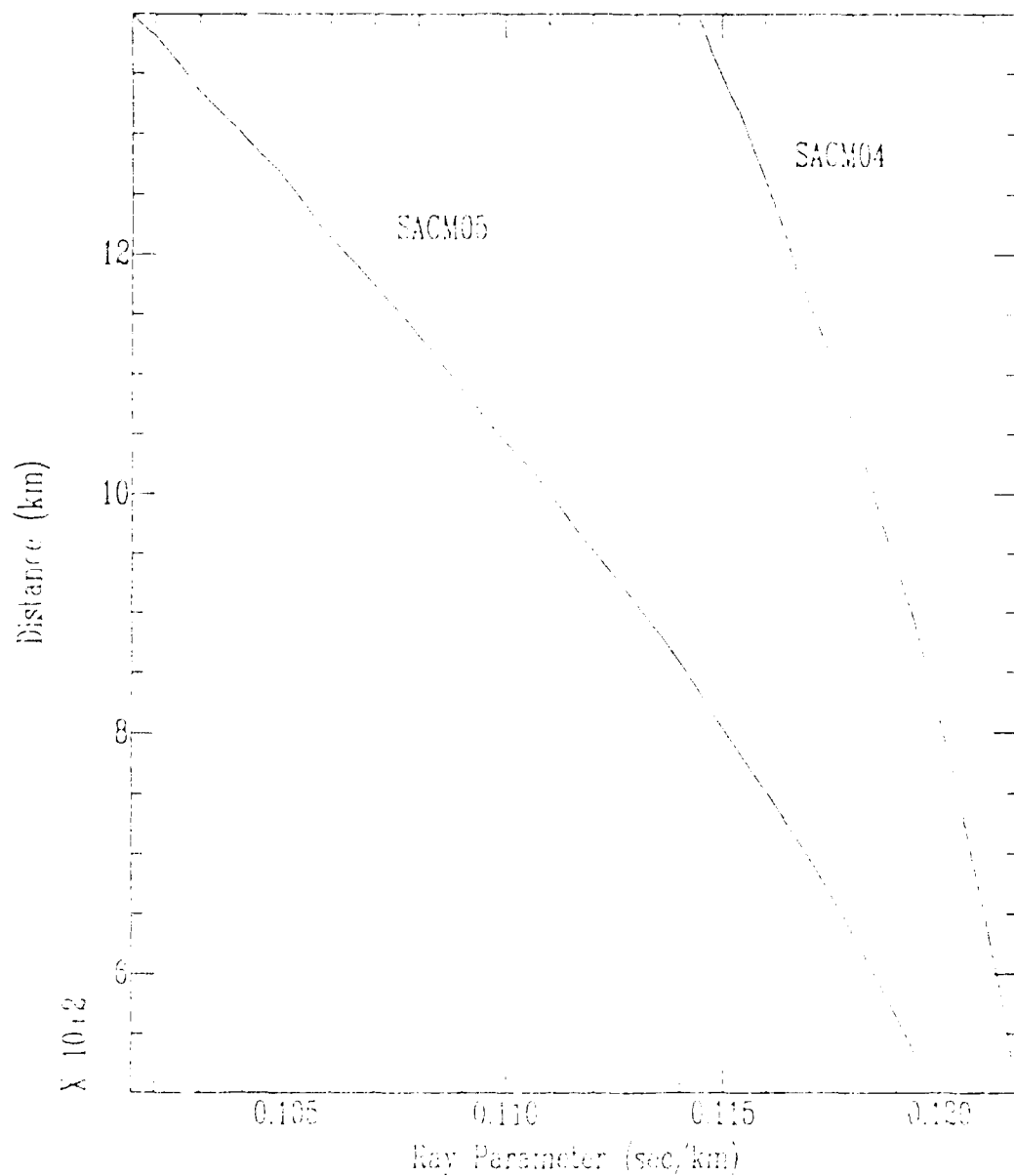


Figure 8. Ray parameter versus distance curves for the direct mantle P-wave for Event 1 and SACM04 and SACM05. These are used to determine ray bottoming depths, as explained in the text. Note that for a given distance from the source, the ray parameter for P is smaller for SACM05 than for SACM04. Hence P bottoms deeper in the higher gradient model for a given station.

average structure down to 160 km depth. If there is no evidence in the data of interaction with an LVZ, this also constrains the minimum lithospheric thickness, assuming that an LVZ marks the base of the lithosphere.

The vertical synthetics and data for SACM04 and Event 1 are shown in Figure 9. Recall that the mantle gradient should cause the P_nA/PL ratio to increase by contributing turning wave energy to the waveforms. Notice that the P_nA/PL ratio at BUL has increased only slightly. This station is too close for the gradient to have a large effect, and the data P_nA amplitude may be increased by low-frequency noise. At PRE, the first precursor phase is clearly visible in the synthetics, its polarity and amplitude being equivalent to that in the data. This confirms that the first precursor in the data is the direct mantle P-wave because it is the first arrival, and its polarity and amplitude are consistent with that of a synthetic P-wave with a take-off angle (from ray parameter-distance curves) in the dilatational quadrant of the focal sphere. Based on travel-times, the energy primarily responsible for boosting P_nA is sP. Due to its small free surface reflection coefficient for this slowness (≈ 0.1), and near-nodal initial amplitude, pP is not seen, and so we are left without an explanation for the second precursor phase. Explanations for this phase will be discussed later. However, we still conclude from the PRE data that SACM04 is a better estimate of the mantle structure beneath the craton than is LH01.

At WEN in Figure 9, notice that the synthetic P_nA/PL ratio is overestimated. The synthetic mantle P-wave (at 18 sec) at SDB is much larger than that in the data, which is near noise level. Together these imply that more turning wave energy is present in the synthetics than is actually in the data. Thus, judging from the vertical

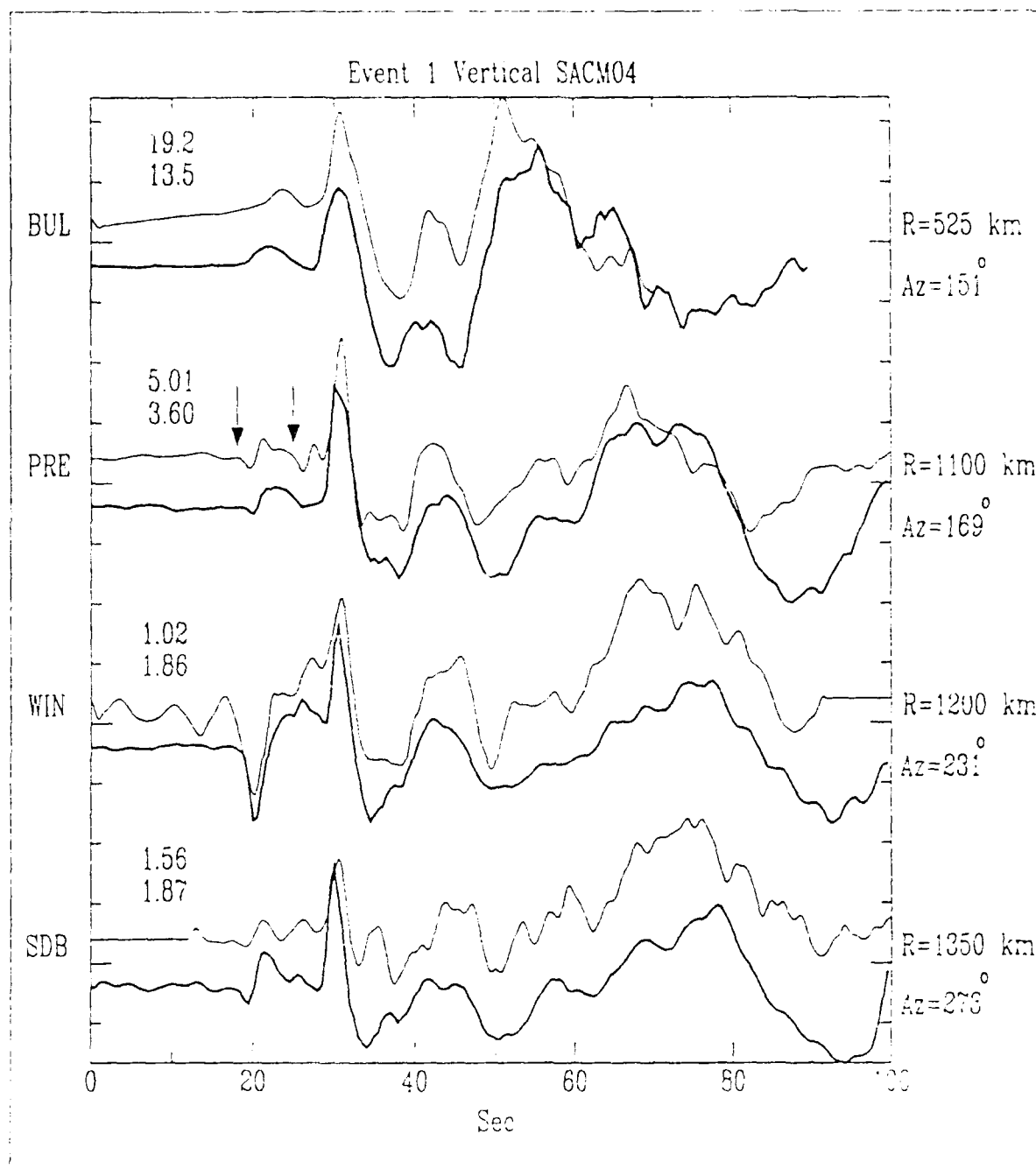


Figure 9. Vertical component data and synthetics for SACM04 and Event 1. PRE synthetics now contain the first precursor arrival-- the direct mantle P-wave. The second precursor arrival cannot be modeled. Synthetic $P_n A/PL$ ratio at BUL is too small; that at PRE is nearly correct; at WIN, it is too large. This implies that the SACM04 gradient is too high to represent the mobile belt upper mantle, while approximately correct, if not low, for the cratonic upper mantle.

components, the gradient in SACM04 is too high, although, as seen from the discussion for LH01 synthetics for WIN, a small gradient is required to model data from the mobile belt regions. Recall that paths to WIN and SDB lie along the mobile belts.

Radial components for SACM04 and Event 1 are given in Figure 10. The first precursor phase in the PRE data is clearly present in the synthetic, as it was on the vertical component, but the second precursor phase remains missing. At WIN the synthetic $P_n A/PL$ ratio is slightly overestimated. The initial P-wave arrival at SDB, predicted by the synthetics, is either not in the data, or too near noise level. These observations reiterate the conclusions drawn from the vertical components.

Figure 11 displays the vertical data and synthetics for model SACM04 and Event 2. Clearly, the fit has been improved using the gradient model. The shoulder produced by the interference between the first two arrivals at WIN (P and sP) is reproduced. We also notice that the synthetic $P_n A/PL$ ratio at both BUL and WIN has increased, though by too much at WIN and not enough at BUL. This indicates that SACM04 overestimates the actual gradient sampled by the WIN data, and underestimates that sampled by the BUL data.

The BUL synthetic predicts a dilatational first arrival (arrowed in Fig. 11), representing the mantle P-wave. This polarity is consistent with the take-off angle of P from the focal sphere in the model. Therefore, the precursor phase at BUL cannot be interpreted as a direct P-wave in our structure model. Furthermore, allowable changes in source parameters ($\pm 4^\circ$ in strike, dip, and rake) cannot produce such an arrival. Examination of short-period teleseismic records shows no evidence of a small magnitude foreshock, ruling out such an explanation. Speculation on the nature

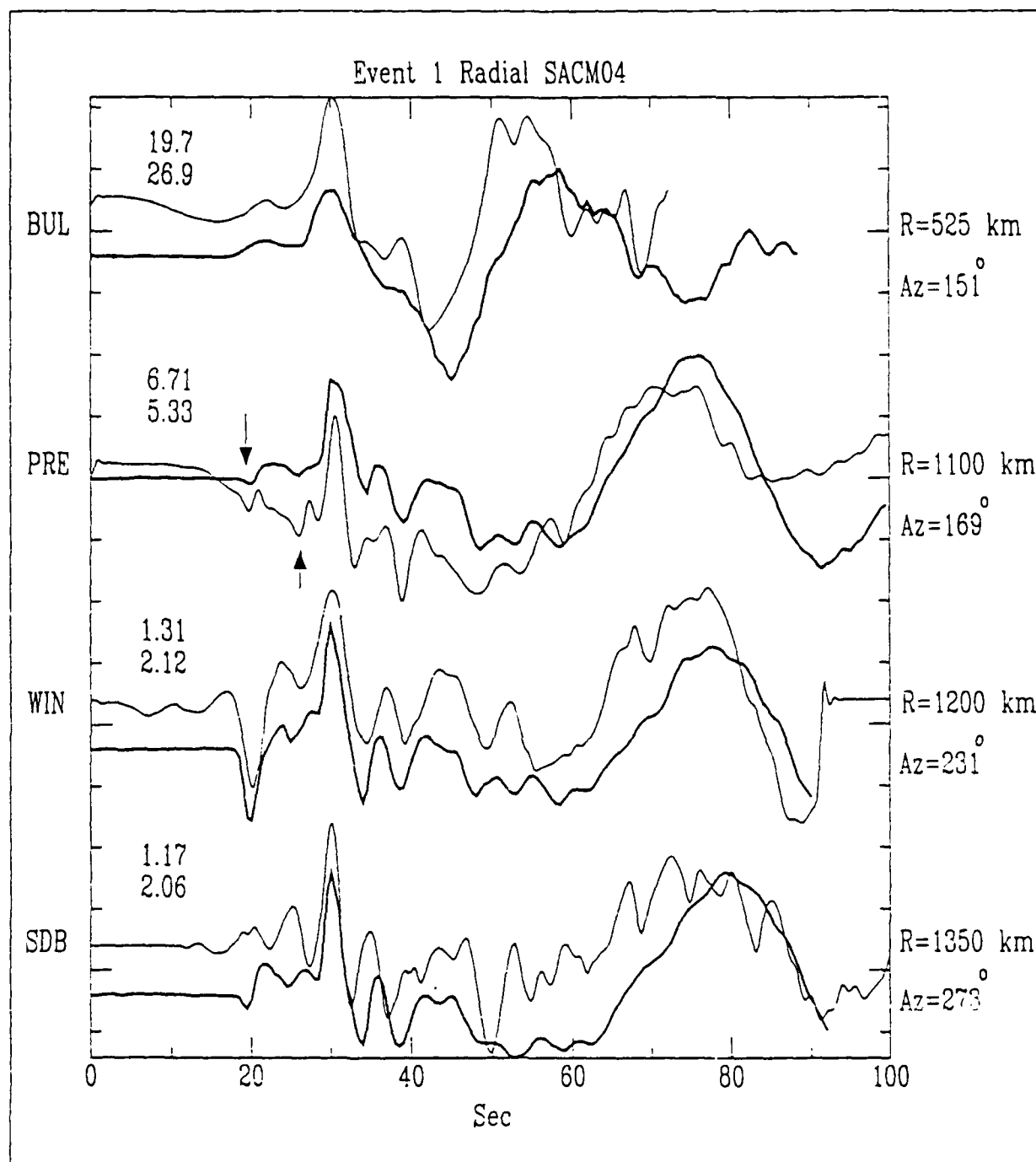


Figure 10. Radial component data and synthetics for SACM04 and Event 1. Long-period noise in the BUL and PRE data precludes accurate $P_n A / PL$ ratio estimates. However, the first precursor at PRE is present, though not the second. $P_n A / PL$ ratio at WIN is overestimated by the synthetic and the P-wave arrival at SDB (at 18 sec) predicted by the synthetic is missing, showing that this gradient is too high.

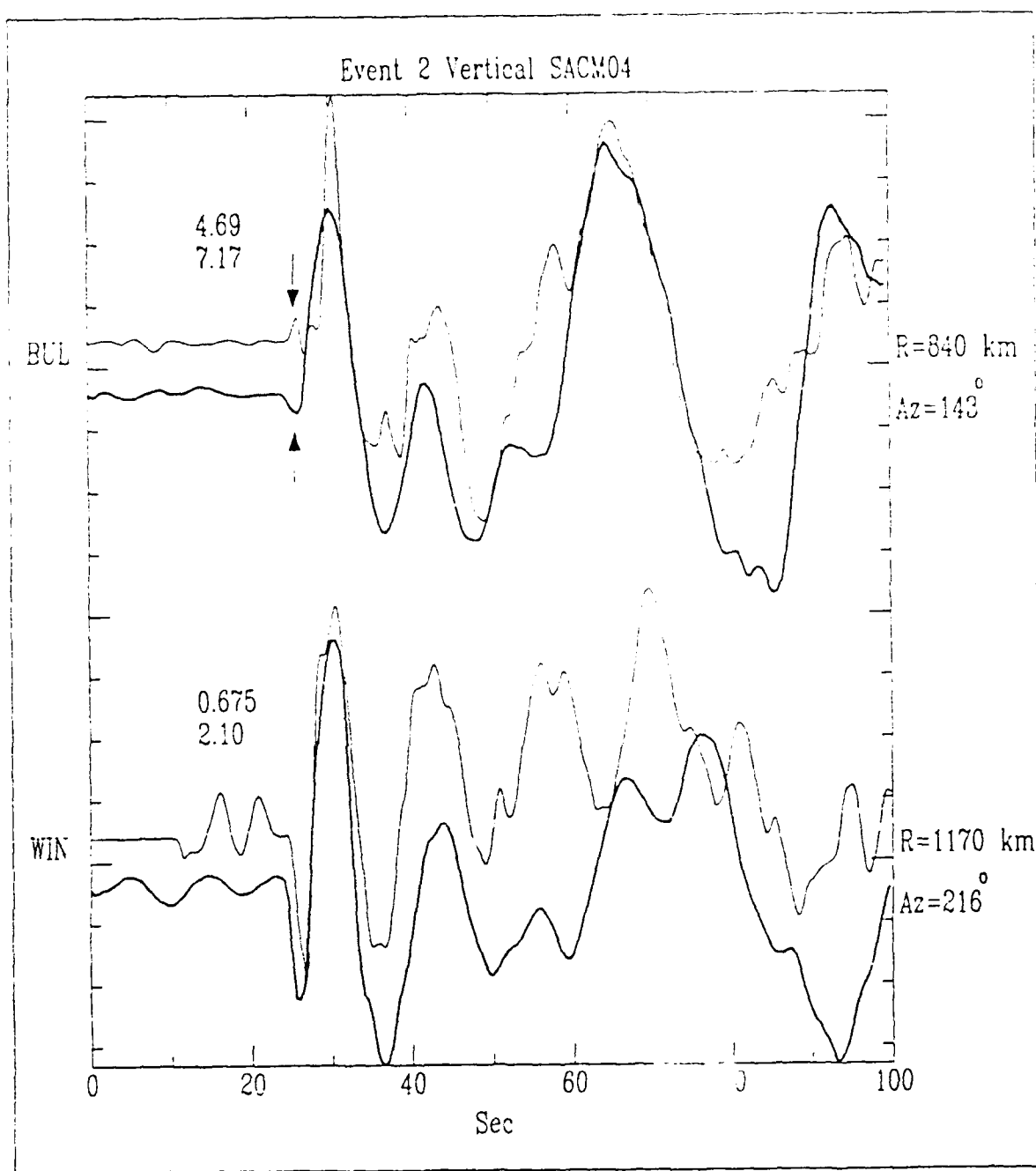


Figure 11. Vertical component data and synthetics for SACM04 and Event 2. $P_n A/PL$ ratio at BUL has increased, though not enough. The synthetic predicts a dilatational first arrival; a compressional arrival is seen in the data. This arrival cannot be explained by a mantle gradient. The $P_n A/PL$ ratio at WIN is overestimated slightly, and the shoulder is present in the unfiltered synthetic.

of this arrival will be diverted until later, but its occurrence does not affect our requirement for a mantle gradient.

In an attempt to further increase the P_nA/PL ratio at BUL for both events, and to see how well we could constrain the gradient magnitude, we computed synthetics for model SACM05, which has a gradient double the magnitude of that in SACM04. SACM05 is also shown in Figure 7. Mantle shear velocity, density, and attenuation is the same as in SACM04. For this higher gradient model, we expect the synthetic P and P_nA amplitudes to increase further relative to the PL wave at all stations.

Figure 12 displays the vertical data and synthetics from model SACM05 and Event 1. At BUL, the larger gradient has boosted P_nA slightly, so that the P_nA/PL ratio is close to the data ratio. However, at PRE the P_nA phase is now 2.5 times as large as the PL wave, a much larger ratio than in the data ($P_nA/PL=1.66$). Furthermore, the synthetic PL wave arrives late at all stations, because the P_nA-PL time is larger than in the data; i.e., P_nA arrives too early, implying too high mantle velocities. Thus, PRE indicates that this gradient is too large: SACM04 synthetics fit all but the BUL data better. The P_nA amplitude at BUL may be artificially increased by long-period noise (apparent in the first 20 secs), its true amplitude being less than that shown. Alternatively, an increase in the gradient at shallow depth in SACM04, where the energy arriving at BUL turns, might increase P_nA without requiring a higher overall gradient, which is precluded by the PRE data. The latter hypothesis was not modeled, though the Event 2 BUL data suggest that this explanation is correct.

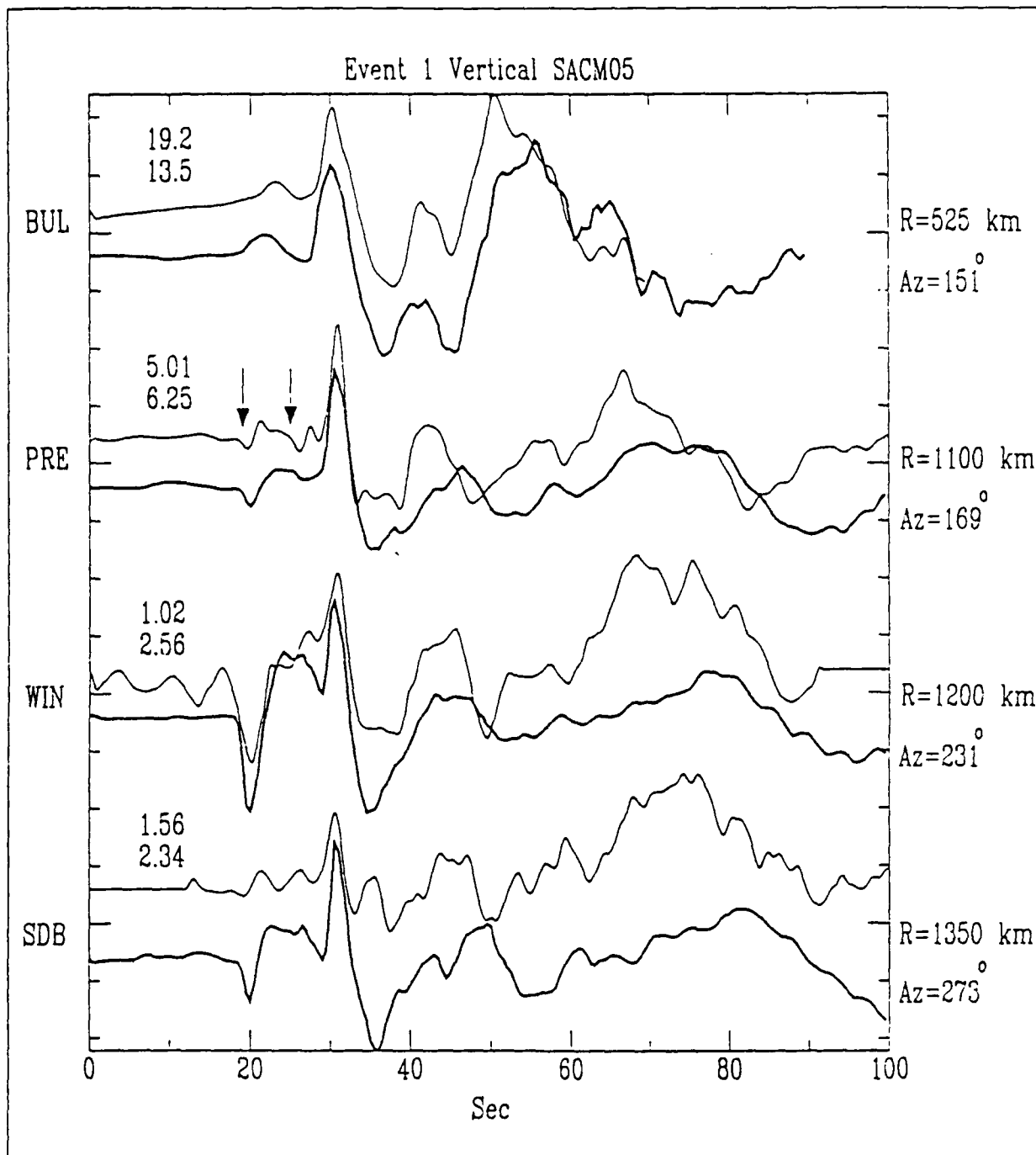


Figure 12. Vertical component data and synthetics for SACM05 and Event 1. $P_n A / PL$ ratio at WIN is greatly overestimated, and the large dilatational P-wave at SDB (18 sec) is not in the data. The $P_n A / PL$ ratio at BUL is close to the data ratio. At PRE, the synthetic $P_n A / PL$ ratio is slightly too large, indicating that the noise at BUL is causing an erroneous ratio. Notice that the $P_n A / PL$ ratio is not as highly overestimated at PRE as at WIN.

Obviously, the synthetic $P_n A/PL$ ratio at WIN in Figure 12 is greatly exaggerated, as we expected from the SACM04 synthetics, which already overestimated this ratio. At SDB, the very large direct mantle P-wave in the synthetics is totally absent from the data. Thus, the gradient in SACM05 is definitely too large for both cratonic and mobile belt paths, and that in SACM04 appears to give the best fitting synthetics for Event 1 cratonic path data. Radial components in Figure 13 yield the same conclusion.

Figure 14 shows the vertical component data and synthetics from SACM05 and Event 2. Clearly the gradient in this model is too high for the WIN data, as evidenced by the very large synthetic $P_n A/PL$ ratio at WIN, as well as the extreme absolute amplitude difference. At BUL though, the fit is good, except for the missing compressional precursor arrival. There is no long-period noise here to induce amplitude errors as there is for the Event 1 BUL data. The data and synthetic $P_n A/PL$ ratios are very close, though for the Event 1 data this model's synthetics overestimated the $P_n A/PL$ ratio at PRE. For raypaths as close together (azimuthally) as those to BUL and PRE, SACM05 could not be the best fitting model for Event 2 but not for Event 1. This could be explained if the BUL data could be fit with a model similar to SACM04 but with a higher gradient at shallow depth, as discussed above. This was not modeled, however, as it does not affect the quantitative conclusion about the average gradient, which is best constrained by the PRE and WIN data.

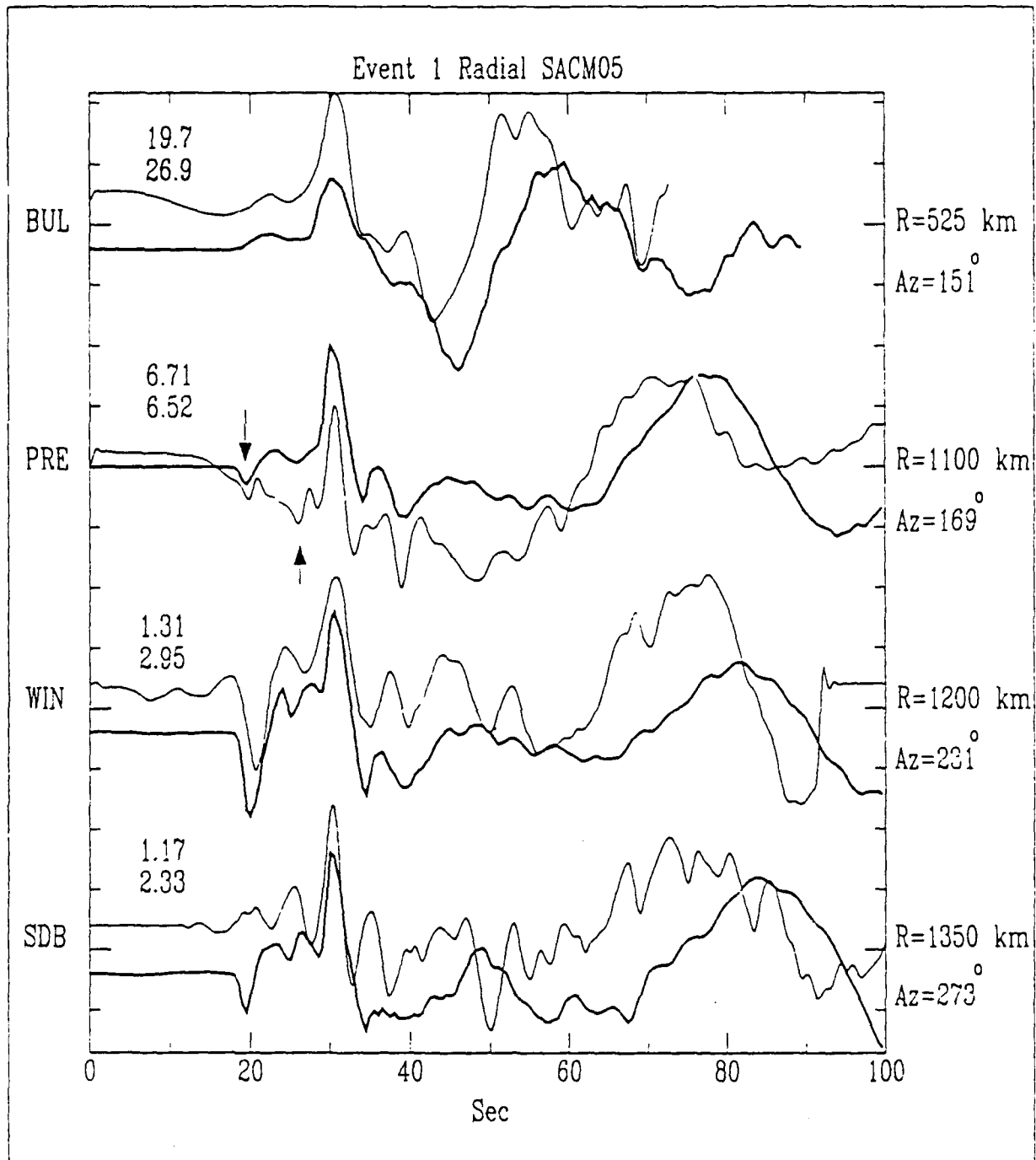


Figure 13. Radial component data and synthetics for SACM05 and Event 1. Long-period noise at BUL and PRE precludes measurement of $P_n A / PL$ ratios. Note large P arrival at SDB, missing in the data, and the too large synthetic $P_n A / PL$ ratio at WIN, indicating that the gradient is too large.

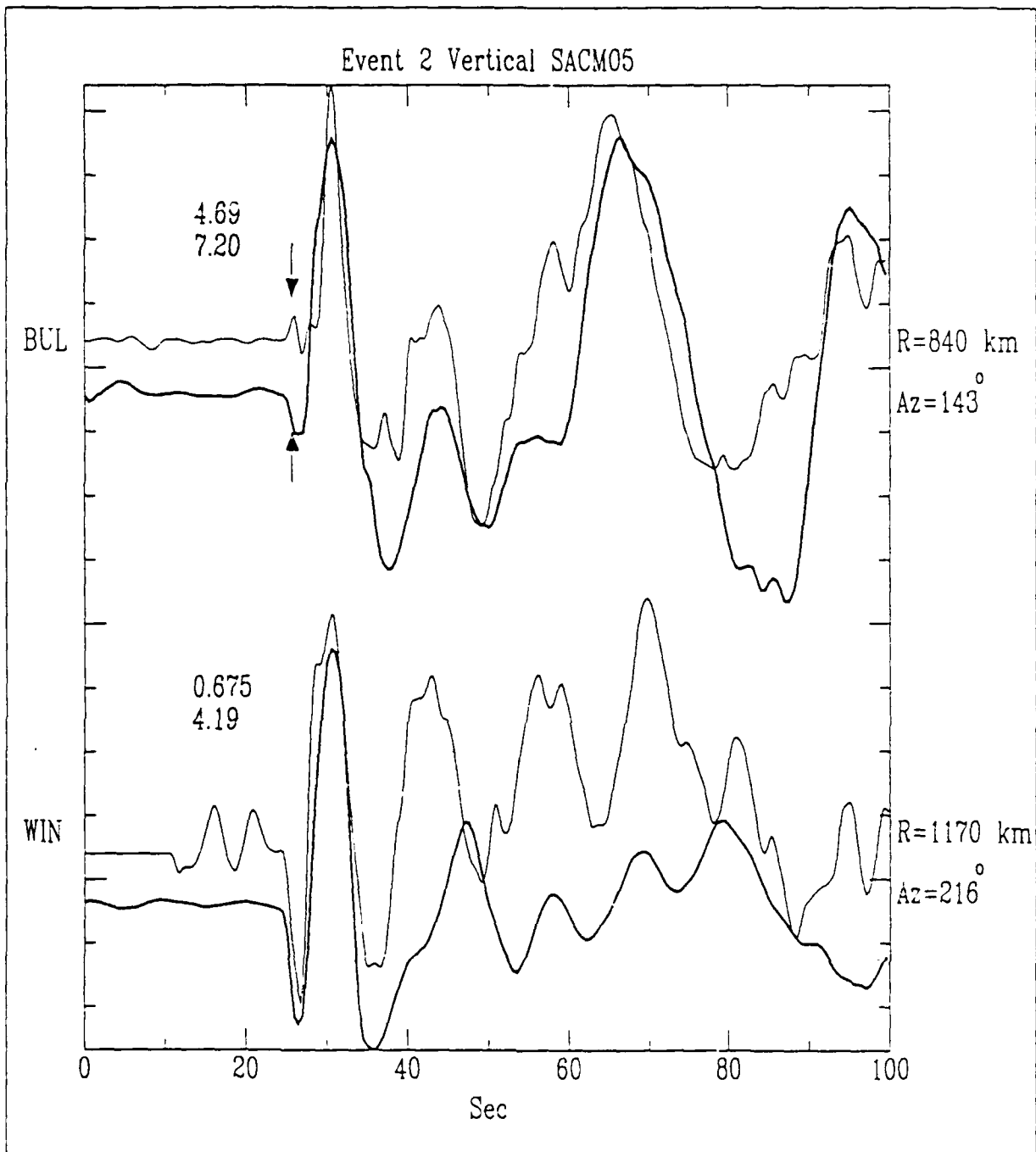


Figure 14. Vertical component data and synthetics for SACM05 and Event 2. The $P_n A/PL$ ratio at BUL is very similar to data ratio, but this gradient is too high, as shown by the PRE data, indicating a steeper gradient than SACM04 at shallow depth. The first arrival in the data is also missing, indicating more complicated structure than a simple gradient. The $P_n A/PL$ ratio at WIN is greatly overestimated in the synthetic.

DISCUSSION

Comparison of the data and synthetics above indicates that there is definitely a positive P-wave velocity gradient in the upper mantle beneath southern Africa. Evidence for this is two-fold. First, and most convincingly, the appearance in the data of mantle turning wave arrivals requires a positive gradient. This phase is totally lacking in the model with a constant mantle velocity (LH01). Secondly, a larger P_nA/PL ratio in the data than in the LH01 synthetics implies some amount of mantle turning wave energy in the seismograms.

The data also indicate that the mantle gradient is probably slightly lower beneath the mobile belt regions (WIN-SDB paths) than beneath the cratonic regions (BUL-PRE paths). This is based on the observation that the gradient model SACM04 synthetics fit the PRE data well, while they overestimate the P_nA/PL ratio at WIN for both events. The higher gradient model, SACM05, overestimates the P_nA/PL ratio at all stations except EUL for both events, indicating that this gradient is too high. We therefore deduce that the gradient is slightly less than 0.00333/sec beneath the mobile belts, and approximately 0.00333/sec beneath the cratons, though the data cannot constrain the gradient this accurately. This difference conveys important information about the tectono-thermal state of the region, as discussed below.

The criteria used to infer the gradient and its magnitude are affected by errors in the source parameters. Hence, an examination of how amplitudes of P, P_nA , and PL are affected by these factors is required. Error bounds on the moment tensor elements

are given by Wagner (1986). Since these do not relate directly to the double couple parameters, we determined strike, dip, and rake for various moment tensors to determine error bounds on these quantities. A conservative estimate for all parameters is: $\pm 3^\circ$ for Event 1, and $\pm 4^\circ$ for Event 2. Of particular interest is the sensitivity of the Event 1 PRE and WIN synthetics to these errors, since these data best constrain the gradient magnitude. We found that errors in the dip had the largest effect on the waveform, but that this effect was negligible with regards to the $P_n A / PL$ ratio. Strike and rake had similarly small effects on the synthetics, so that our conclusions remain unaffected by the allowable range in source parameters.

For comparison with other velocity models, and for delimiting the depths over which our model SACM04 applies, we summarize mantle P-wave bottoming depths at the appropriate stations. The P-wave arrival at PRE bottoms at 120 km depth beneath the Kapvaal-Rhodesian craton. The P-wave at WIN, 100 km further from the source, bottoms at 140 km beneath the Damara Fold Belt.

While they do not affect our conclusions about the average gradient, certain aspects of the data could not be reproduced in the synthetics. The most obvious misfit is that neither the second precursor phase at PRE for Event 1, nor the first arrival at BUL for Event 2 could be reproduced with our models (see Figs. 9 and 11). Both of these stations lie on the craton. Something more complicated than a monotonic gradient must be responsible for these discrepancies, because allowable changes in source parameters cannot produce these arrivals. The phases could be due to small foreshocks, but examination of short period teleseismic and regional records indicated no such events. Perhaps reflection from or refraction through a high-

velocity or high-velocity gradient layer beneath the craton is responsible; testing this would require further modeling.

The P-wave velocity model of Bloch, et al. (1969) contained no high-velocity zones, though their methods were not sensitive to the P-wave velocity regime, nor to thin layers. Other workers have reported high-velocity layers at shallow depth in the lithosphere. Hirn, et al (1973) described relatively high velocity refractors at 55 and 80 km depth in France from a long (1000 km) refraction profile. A compilation of similar long-range refraction results from many different areas, showing evidence of fine layering in the lithosphere, is given by Fuchs (1979). Proposed explanations for this phenomenon include anisotropy (due to preferred alignment of olivine crystals) within the layers, and lateral petrologic and chemical heterogeneities. Bamford (1977) has demonstrated a 7% anisotropy in P_n -velocity in western Germany, though a subsequent study (Bamford, et al., 1978) in northern Britain failed to reveal any significant anisotropy. Thus, such layering may not be ubiquitous, and more data is required to conclusively identify and study it in southern Africa.

Precise modeling of other aspects of the data would require a small modification to the gradient model. Recall that the SACM04 synthetics consistently underestimated the $P_n A/PL$ ratio at BUL for both events (Figs. 9 and 11). This was true even for Event 2, which contained no low-frequency noise. Model SACM05 produced better fitting synthetics at BUL, but not at PRE for Event 1, and the latter constrains the gradient better. Since BUL is nearer the source, this could indicate that a higher gradient is present at shallow depth, where the rays to BUL turn. Such a modification would increase the $P_n A/PL$ ratio at BUL without affecting further stations. Since our

purpose was to determine the average gradient, this aspect was not modeled.

Synthetic mantle turning wave amplitudes are also affected by our choice of upper mantle QP and QS values. Higher Q values would require a smaller velocity gradient to produce similar amplitudes, though relative travel-times would also be changed. When compared with published Q values (Anderson, et al., 1965; Anderson and Hart, 1978; Patton, 1980), our values are approximately twice as large. However, these studies generally find an averaged Q over broad regions; no attenuation studies have been undertaken in southern Africa. Therefore, our values may be high, but not unreasonable for an old, stable platform and cratonic region. If a subsequent, independent Q survey should yield a lower Q value, it could imply a slightly higher mantle gradient than determined here.

A positive mantle P-wave velocity gradient has implications for the southern African upper mantle thermal regime. Since our data reveal that the gradient is smaller beneath mobile belts than beneath cratons, this study supports the deep lithospheric root hypothesis. Assuming pressure changes with depth are roughly equal between the two provinces, and assuming similar petrologies, the higher velocity gradient indicates lower temperatures and temperature gradients in the cratonic root. The nominal model used by Ballard and Pollack (1987) predicts this difference in thermal structure. It indicates that at a depth of 100 km, the mobile belt mantle is about 600° C hotter than the cratonic root, and the temperature gradient is higher in the mobile belt lithosphere down to 100 km. Temperature gradients below 100 km are higher in the cratonic root than in the adjacent asthenospheric, mobile belt mantle, but between these two regions there is a major rheologic difference. The temperature

profiles do not merge until 800 km depth.

A lower limit to the depth of the root can be ascertained from the bottoming depths of the direct mantle P-waves at PRE for Event 1. The bottoming depth from SACM04 for the P-wave at PRE is 120 km, and there was no evidence for a P-wave LVZ. Ballard and Pollack (1986) estimate that the root may extend anywhere from 200 to 400 km depth, so our conclusion is well within the lower limit. Brune and Dormann (1963), using surface wave dispersion, did not detect a P-wave LVZ beneath the Canadian shield above 400 km. Like the Rhodesian-Kapvaal craton, the Canadian shield also has relatively low heat flow. In northwestern Eurasia, Given and Helmberger (1980), using body waves, did detect a small LVZ for P-waves, 50 km thick, beginning at 150 km depth. Thus, our data may not sample deep enough to detect an LVZ, but it does yield a minimum lithospheric thickness in the craton.

Fairhead and Reeves (1977) have estimated lithospheric thickness over most of the African continent by combining teleseismic delay times and Bouger anomalies. Their map shows a thickness of 150-175 km beneath BUL and PRE, which is consistent with our derived minimum lithospheric root thickness of 120 km, and with the Ballard and Pollack (1987) study.

Their map shows thinner lithosphere in the mobile belt regions, the thickness beneath WIN and SDB being less than 150 km. The direct P-wave at WIN for SACM04 for Event 1 bottoms at 140 km; however, since we believe that the gradient is slightly less than that in SACM04, the ray actually bottoms shallower. This depth is close to the lithospheric thickness in the region given by Fairhead and Reeves (1977), so the actual rays could be encountering a low velocity zone, an effect which

we did not model. However, there was no hard evidence from our small data set of interaction with an LVZ, so the lithosphere is somewhat less than 140 km thick beneath the mobile belts. Unfortunately, the SDB data, which would have given a deeper sampling of the structure, proved unusable.

Figure 15 compares our velocity models with those from previous studies. Green's (1978) model was obtained from inversion of P-wave travel times for earthquakes throughout eastern and southern Africa, the Red Sea, and Gulf of Aden. Because of source-station geometry, the upper 250 km of his model is more representative of the rift zone upper mantle, or at best an average of stable and active upper mantle regions. Only velocity values below this depth apply to southern Africa. It shows an overall slight positive gradient, but the values are considerably less than those in SACM04. This is probably a result of the different regions examined in the two studies, and our models do not extend deep enough to compare with Green's below 250 km.

Figure 15 also shows the P-wave velocity model of Gumper and Pomeroy (1970), obtained from surface wave dispersion. Notice that it agrees closely with that of Green (1978), probably because these models both average structure between the rift zone and more stable regions.

Finally, we compare our models with that of Bloch, et al. (1969). Their study region is nearly identical to ours, and their model does not average between major tectonic provinces. Our model SACM04 and the Bloch model coincide closely for most of the former's depth range. Model SACM05 diverges rapidly from theirs below 70 km depth, and we have shown that this gradient is too high. SACM04

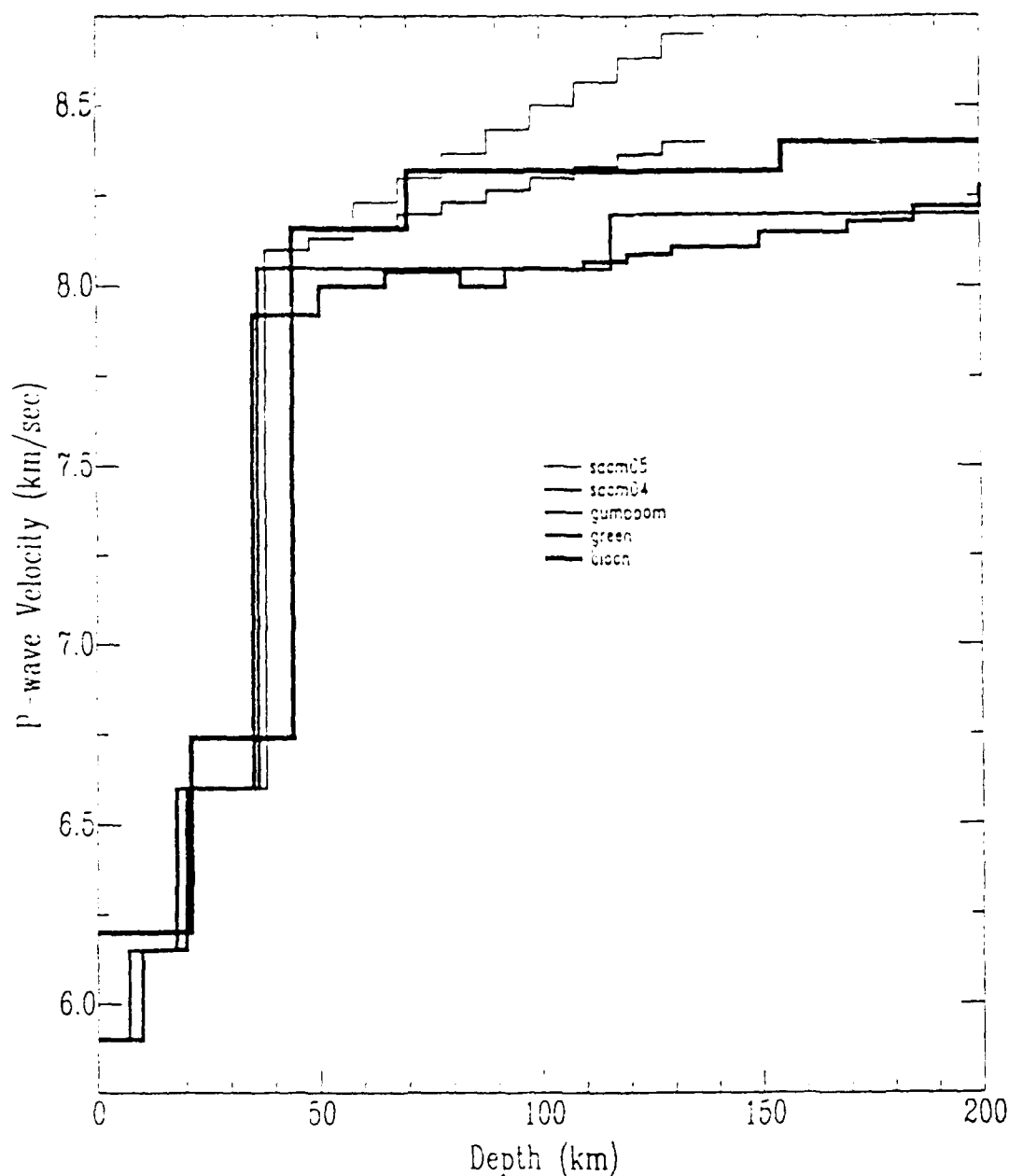


Figure 15. Comparison of models SACM04 and SACM05 with models of Gumper and Pomeroy (1970), Green (1978), and Bloch, et al. (1969). Models are for a spherically stratified earth. The first two models are more representative of the tectonically active regions. Note that SACM05 quickly diverges from all other models. The Bloch model agrees closely with our model: SACM04, resulting from the two studies examining the same region. SACM04 is defined by the PRE data to a depth of 120 km beneath the craton.

represents structure at least down to 120 km depth beneath the cratons, and probably deeper. Beneath the mobile belts, the actual gradient is less than in SACM04, and is probably defined to a depth somewhat less than 140 km. A lower gradient beneath the mobile belt regions would also agree closely with Bloch's model.

To determine if we could distinguish between a gradient and a velocity jump, as shown in the Bloch, et al. (1969) model at 70 km depth, we computed synthetics for their model. The velocity jump model synthetics did not match the PRE data for Event 1, and so we conclude that a gradient is more appropriate than a velocity jump. Surface wave dispersion cannot resolve a velocity gradient, so it represents it as a velocity jump. However, a model with a small velocity jump separating two layers having a positive velocity gradient was not examined, and could possibly explain the unmodeled precursor phase at PRE and BUL.

CONCLUSIONS

The data from this study indicate that there is a positive P-wave velocity gradient in the upper mantle beneath southern Africa. Synthetic seismograms were generated using a wavenumber integration routine, and compared with P_n waveform data from two Zambia earthquakes. Previous workers have determined the source parameters for these events, thereby allowing modeling of structure effects. The source-station distribution allows for examination of structure beneath cratons and mobile belts independently, to detect differences in upper mantle structure.

Based on the existence in the data of mantle turning wave phases P and sP, and

their amplitudes relative to PL, the gradient magnitude could be estimated. A gradient of approximately 0.00333/sec is indicated for the average velocity structure beneath the Kapvaal-Rhodesian craton (model SACM04). Some of the data suggest that the gradient may be steeper at shallower depths. From P-wave bottoming depths, this gradient extends at least to 120 km, which is also a lower limit on lithospheric thickness beneath the craton. This conclusion is consistent with lithospheric thickness studies from regional gravity and teleseismic P-wave delay times.

Based on similar criteria, a smaller positive gradient must exist beneath the mobile belts. A magnitude slightly less than 0.00333/sec, but still non-zero, is considered likely. For model SACM04 the bottoming depth of P-waves at WIN, the furthest mobile belt station showing no evidence of a LVZ, is 140 km. Lithospheric thickness studies give a thickness of less than 150 km for the mobile belt regions.

Our inability to model some precursor arrivals at PRE and BUL with a monotonic velocity gradient suggests that there may be high-velocity layers in the cratonic upper mantle. These precursors only occur at cratonic path stations, and more data is needed to determine the nature and cause of this phase.

Our conclusion of a higher velocity gradient beneath the cratonic province supports the hypothesis that a deep, cool lithospheric root exists underneath this region. Our data also place a minimum depth extent on the root of 120 km. The root was originally postulated as a mechanism for heat diversion to explain lower values of observed heat flow (Ballard and Pollack, 1987) in the craton than in the mobile belts. Tectonically, this implies that the cratonic lithosphere has remained largely unaffected by post-Archean heating events. Similar data sets could be used elsewhere

to detect upper mantle velocities and heterogeneities between tectonically old and young regions.

REFERENCES

- Anderson, D.L., Ben-Menahem, A., and C.B. Archambeau, 1965. Attenuation of seismic energy in the upper mantle. *J. Geophys. Res.*, 70:1441-1448.
- Anderson, D.L. and Hart, R.S., 1978. Q of the Earth. *J. Geophys. Res.*, 83:5869-5882.
- Anderson, D.L. and Sammis, C., 1970. Partial melting in the upper mantle. *Phys. Earth Planet. Interiors*, 3:41-50.
- Apsel, R., 1979. Dynamic Green's functions for layered media and applications to boundary value problems. Ph.D. Thesis, University of California, San Diego, La Jolla, California.
- Ballard, S. and Pollack, H.N., 1987. Diversion of heat by Archean cratons: a model for southern Africa. *Earth and Planet. Sci. Letters*, 85:253-264.
- Bamford, D., 1977. P_n velocity anisotropy in a continental upper mantle. *Geophys. J. R. astr. Soc.*, 49:29-48.
- Bamford, D., Nunn, K., Prodehl, C., and Jacob, B., 1978. LISP-IV. Crustal structure of northern Britain. *Geophys. J. R. astr. Soc.*, 54:43-60.
- Barker, J.S., 1984. A seismological analysis of the May 1980 Mammoth Lakes, California earthquakes. Ph.D. Thesis, Pennsylvania State University.
- Bloch, S., Hales, A.L., and Landisman, M., 1969. Velocities in the crust and upper mantle of southern Africa from multi-mode dispersion. *Bull. Seismol. Soc. Am.*, 59(4):1599-1629.
- Bott, M.H.P., 1982. The Interior of the Earth: its structure, constitution, and evolution. Second Edition. Elsevier, New York.
- Brune, J. and Dorman, J., 1963. Seismic waves and earth structure in the Canadian Shield. *Bull. Seismol. Soc. Am.*, 53:167-209.
- Chapman, D.S. and Pollack, H.N., 1977. Heat flow and heat production in Zambia: evidence for lithospheric thinning in central Africa. *Tectonophysics*, 41:79-100.
- Condie, K.C., 1982. Plate Tectonics and Crustal Evolution. Second edition. Pergamon Press, New York.
- de Beer, J.H., Gough, D.I., and van Zijl, J.S.V., 1975. An electrical conductivity anomaly and rifting in southern Africa. *Nature*, 255:678-680.
- Dunkin, J.W., 1965. Computations of model solutions in layered, elastic media at high frequencies. *Bull. Seismol. Soc. Am.*, 55:335-358.
- Fairhead, J.D., and Girdler, R.W., 1971. The seismicity of Africa. *Geophys. J. R. Astr. Soc.*, 24:271-301.
- Fairhead, J.D., and Reeves, C.V., 1977. Teleseismic delay times, Bouguer anomalies, and inferred thickness of the African lithosphere. *Earth and Planet. Sci. Letters*, 36:63-76.

- Fuchs, K., 1979. Structure, physical properties, and lateral heterogeneities of the sub-crustal lithosphere from long-range deep seismic sounding observations on continents. *Tectonophysics*, 56:1-15.
- Gane, P.G., Atkins, A.R., Sellschop, J.P.F., and Seligman, P., 1956. Crustal Structure in the Transvaal. *Bull. Seismol. Soc. Am.*, 46:293-316.
- Girdier, R.W., 1975. The great negative Bouguer anomaly over Africa. *EOS*, 56:516-519.
- Given, J.W. and Helmberger, D.V., 1980. Upper mantle structure of northwestern Eurasia. *J. Geophys. Res.*, 85:7183-7194.
- Green, A.G., 1978. An upper mantle P-wave velocity model for eastern and southern Africa. *Pageoph., Birkhuser Verlag, Basel*, 116:1262-1273.
- Gumper, F. and Pomeroy, P.W., 1970. Seismic wave velocities and earth structure on the African continent. *Bull. Seismol. Soc. Am.*, 60:651-668.
- Hales, A.L. and Sacks, I.S., 1959. Evidence for an intermediate layer from crustal structure studies in the eastern Transvaal. *Geophys. J. R. astr. Soc.*, 2:15-33.
- Haskell, N.A., 1953. The dispersion of surface waves on multilayered media. *Bull. Seismol. Soc. Am.*, 43:17-34.
- Helmberger, D.V., 1972. Long-period body-wave propagation from 4° to 13° . *Bull. Seismol. Soc. Am.*, 62(1):325-341.
- Helmberger, D.V., 1973. Numerical seismograms of long-period body waves from seventeen to forty degrees. *Bull. Seismol. Soc. Am.*, 63(2):633-646.
- Helmberger, D.V. and Engen, G.R., 1980. Modeling the long-period body waves from shallow earthquakes at regional ranges. *Bull. Seismol. Soc. Am.*, 70:1699-1714.
- Hirn, A., Steinmetz, L., Kind, R., and Fuchs, K., 1973. Long range profiles in western Europe: II. Fine structure of the lower lithosphere in France (southern Bretagne). *Z. Geophys.*, 39:363-384.
- Kroner, A., 1977. Precambrian mobile belts of southern and eastern Africa-ancient sutures or sites of ensialic mobility? A case for crustal evolution towards plate tectonics. *Tectonophysics*, 40:101-135.
- Oliver, J., 1964. Propagation of PL waves across the United States. *Bull. Seismol. Soc. Am.*, 54:151-160.
- Oliver, J. and Major, M., 1960. Leaking mode and the PL phase. *Bull. Seismol. Soc. Am.*, 50:165-180.
- Patton, H., 1980. Crust and upper mantle structure of the Eurasian continent from the phase velocity and Q of surface waves. *Rev. Geophys. space Phys.*, 18:605-625.
- Pavlin, G.B., 1981. Source parameter inversion of a reservoir-induced seismic sequence, Lake Kariba, Africa, September 1963-August 1974: a reassessment of triggering mechanisms. Ph. D. Thesis, Pennsylvania State University.

- Press, F., Ewing, M., and Oliver, J., 1956. Crustal structure and surface-wave dispersion in Africa. *Bull. Seismol. Soc. Am.*, 46:97-103.
- Reeves, C.V. and Hutchins, D.G., 1975. Crustal structure in central southern Africa. *Nature*, 254:408-409.
- Shaw, P. and Orcutt, J., 1984. Propagation of PL and implications for the structure of Tibet. *J. Geophys. Res.*, 89(B5): 3135-3152.
- Somville, O., 1930. A propos d'une onde longue dans la premiere phase de quelques seismogrammes. *Gerlands Beitr. Geophys.*, 27:437-442.
- Thomson, W.T., 1950. Transmission of elastic waves through a stratified solid medium. *J. Appl. Phys.*, 21:89-93.
- Thrower, E.N., 1965. The computation of the dispersion of elastic waves in layered media. *J. Sound Vib.*, 2:210-226.
- Wagner, G.S., 1986. Waveform inversion for five African earthquakes and tectonic implications. Master's Thesis, Pennsylvania State University.
- Wallace, T.C., 1983. Long period regional body waves. Ph.D. Thesis, California Institute of Technology, Pasadena, California.
- Willmore, P.L., Hales, A.L., and Gane, P.G., 1952. A seismic investigation of crustal structure in the western Transvaal. *Bull. Seismol. Soc. Am.*, 42:53-80.

CONTRACTORS (United States)

Professor Keiiti Aki
Center for Earth Sciences
University of Southern California
University Park
Los Angeles, CA 90089-0741

Professor Thomas Ahrens
Seismological Lab, 252-21
Div. of Geological and Planetary
Sciences
California Institute of Technology
Pasadena, CA 91125

Professor Charles B. Archambeau
Cooperative Institute for Resch
in Environmental Sciences
University of Colorado
Boulder, CO 80309

Dr. Thomas C. Bache Jr.
Science Applications Int'l Corp.
10210 Campus Point Drive
San Diego, CA 92121 (2 copies)

Dr. Muawia Baruzangi
Institute for the Study of
of the Continent
Cornell University
Ithaca, NY 14853

Dr. Douglas R. Baumgardt
Signal Analysis & Systems Div.
ENSCO, Inc.
5400 Port Royal Road
Springfield, VA 22151-2388

Dr. Jonathan Berger
Institute of Geophysics and
Planetary Physics
Scripps Institution of Oceanography
A-025
University of California, San Diego
La Jolla, CA 92093

Dr. S. Bratt
Science Applications Int'l Corp.
10210 Campus Point Drive
San Diego, CA 92121

Dr. Lawrence J. Burdick
Woodward-Clyde Consultants
P.O. Box 93245
Pasadena, CA 91109-3245 (2 copies)

Professor Robert W. Clayton
Seismological Laboratory/Div. of
Geological & Planetary Sciences
California Institute of Technology
Pasadena, CA 91125

Dr. Karl Coyner
New England Research, Inc.
76 Olcott Drive
White River Junction, VT 05001

Dr. Vernon F. Cormier
Department of Geology & Geophysics
U-45, Room 207
The University of Connecticut
Storrs, Connecticut 06268

Dr. Steven Day
Dept. of Geological Sciences
San Diego State U.
San Diego, CA 92182

Dr. Zoltan A. Der
ENSCO, Inc.
5400 Port Royal Road
Springfield, VA 22151-2388

Professor John Ferguson
Center for Lithospheric Studies
The University of Texas at Dallas
P.O. Box 830688
Richardson, TX 75083-0688

Professor Stanley Flatté
Applied Sciences Building
University of California,
Santa Cruz, CA 95064

Dr. Alexander Florence
SRI International
333 Ravenswood Avenue
Menlo Park, CA 94025-3493

Professor Steven Grand
University of Texas at Austin
Dept of Geological Sciences
Austin, TX 78713-7909

Dr. Henry L. Gray
Associate Dean of Dedman College
Department of Statistical Sciences
Southern Methodist University
Dallas, TX 75275

Professor Roy Greenfield
Geosciences Department
403 Deike Building
The Pennsylvania State University
University Park, PA 16802

Professor David G. Harkrider
Seismological Laboratory
Div of Geological & Planetary Sciences
California Institute of Technology
Pasadena, CA 91125

Professor Donald V. Helmberger
Seismological Laboratory
Div of Geological & Planetary Sciences
California Institute of Technology
Pasadena, CA 91125

Professor Eugene Herrin
Institute for the Study of Earth
and Man/Geophysical Laboratory
Southern Methodist University
Dallas, TX 75275

Professor Robert B. Herrmann
Department of Earth & Atmospheric
Sciences
Saint Louis University
Saint Louis, MO 63156

Professor Bryan Isacks
Cornell University
Dept of Geological Sciences
SNEE Hall
Ithaca, NY 14850

Professor Lane R. Johnson
Seismographic Station
University of California
Berkeley, CA 94720

Professor Thomas H. Jordan
Department of Earth, Atmospheric
and Planetary Sciences
Mass Institute of Technology
Cambridge, MA 02139

Dr. Alan Kafka
Department of Geology &
Geophysics
Boston College
Chestnut Hill, MA 02167

Professor Leon Knopoff
University of California
Institute of Geophysics
& Planetary Physics
Los Angeles, CA 90024

Professor Charles A. Langston
Geosciences Department
403 Deike Building
The Pennsylvania State University
University Park, PA 16802

Professor Thorne Lay
Department of Geological Sciences
1006 C.C. Little Building
University of Michigan
Ann Arbor, MI 48109-1063

Dr. Randolph Martin III
New England Research, Inc.
76 Olcott Drive
White River Junction, VT 05001

Dr. Gary McCarter
Mission Research Corp.
755 State Street
P.O. Drawer 719
Santa Barbara, CA 93102 (2 copies)

Professor Thomas V. McEvilly
Seismographic Station
University of California
Berkeley, CA 94720

Dr. Keith L. McLaughlin
S-CUBED,
A Division of Maxwell Laboratory
P.O. Box 1620
La Jolla, CA 92038-1620

Professor William Menke
Lamont-Doherty Geological Observatory
of Columbia University
Palisades, NY 10964

Professor Brian J. Mitchell
Department of Earth & Atmospheric
Sciences
Saint Louis University
Saint Louis, MO 63156

Mr. Jack Murphy
S-CUBED
A Division of Maxwell Laboratory
11800 Sunrise Valley Drive
Suite 1212
Reston, VA 22091 (2 copies)

Professor J. A. Orcutt
IGPP, A-205
Scripps Institute of Oceanography
Univ. of California, San Diego
La Jolla, CA 92093

Professor Keith Priestley
University of Nevada
Mackay School of Mines
Reno, NV 89557

Professor Paul G. Richards
Lamont-Doherty Geological
Observatory of Columbia Univ.
Palisades, NY 10964

Wilmer Rivers
Teledyne Geotech
314 Montgomery Street
Alexandria, VA 22314

Dr. Alan S. Ryall, Jr.
Center of Seismic Studies
1300 North 17th Street
Suite 1450
Arlington, VA 22209-2308 (4 copies)

Professor Charles G. Sammis
Center for Earth Sciences
University of Southern California
University Park
Los Angeles, CA 90089-0741

Professor Christopher H. Scholz
Geological Sciences
Lamont-Doherty Geological Observatory
Palisades, NY 10964

Dr. Jeffrey L. Stevens
S-CUBED,
A Division of Maxwell Laboratory
P.O. Box 1620
La Jolla, CA 92038-1620

Professor Brian Stump
Institute for the Study of Earth & Man
Geophysical Laboratory
Southern Methodist University
Dallas, TX 75275

Professor Tai-liang Teng
Center for Earth Sciences
University of Southern California
University Park
Los Angeles, CA 90089-0741

Dr. Clifford Thurber
State University of New York at
Stony Brooks
Dept of Earth and Space Sciences
Stony Brook, NY 11794-2100

Professor M. Nafi Toksoz
Earth Resources Lab
Dept of Earth, Atmospheric and
Planetary Sciences
Massachusetts Institute of Technology
42 Carleton Street
Cambridge, MA 02142

Professor Terry C. Wallace
Department of Geosciences
Building #77
University of Arizona
Tucson, AZ 85721

Weidlinger Associates
ATTN: Dr. Gregory Wojcik
4410 El Camino Real, Suite 110
Los Altos, CA 94022

Professor Francis T. Wu
Department of Geological Sciences
State University of New York
at Binghamton
Vestal, NY 13901

OTHERS (United States)

Dr. Monem Abdel-Gawad
Rockwell Internat'l Science Center
1049 Camino Dos Rios
Thousand Oaks, CA 91360

Professor Shelton S. Alexander
Geosciences Department
403 Deike Building
The Pennsylvania State University
University Park, PA 16802

Dr. Ralph Archuleta
Department of Geological
Sciences
Univ. of California at
Santa Barbara
Santa Barbara, CA

J. Barker
Department of Geological Sciences
State University of New York
at Binghamton
Vestal, NY 13901

Mr. William J. Best
907 Westwood Drive
Vienna, VA 22180

Dr. N. Biswas
Geophysical Institute
University of Alaska
Fairbanks, AK 99701

Dr. G. A. Bollinger
Department of Geological Sciences
Virginia Polytechnical Institute
21044 Derrington Hall
Blacksburg, VA 24061

Mr. Roy Burger
1221 Serry Rd.
Schenectady, NY 12309

Dr. Robert Burrige
Schlumberger-Doll Resch Ctr.
Old Quarry Road
Ridgefield, CT 06877

Science Horizons, Inc.
ATTN: Dr. Theodore Cherry
710 Encinitas Blvd., Suite 101
Encinitas, CA 92024 (2 copies)

Professor Jon F. Claerbout
Professor Amos Nur
Dept. of Geophysics
Stanford University
Stanford, CA 94305 (2 copies)

Dr. Anton W. Gainty
AFGL/LWH
Hanscom AFB, MA 01731

Professor Adam Dziewonski
Hoffman Laboratory
Harvard University
20 Oxford St.
Cambridge, MA 02138

Professor John Ebel
Dept of Geology and Geophysics
Boston College
Chestnut Hill, MA 02167

Dr. Donald Forsyth
Dept of Geological Sciences
Brown University
Providence, RI 02912

Dr. Anthony Gangi
Texas A&M University
Department of Geophysics
College Station, TX 77843

Dr. Freeman Gilbert
Institute of Geophysics &
Planetary Physics
University of California, San Diego
P.O. Box 109
La Jolla, CA 92037

Mr. Edward Giller
Pacific Seirra Research Corp.
1401 Wilson Boulevard
Arlington, VA 22209

Dr. Jeffrey W. Given
Sierra Geophysics
11255 Kirkland Way
Kirkland, WA 98033

Rong Song Jin
Teledyne Geotech
314 Montgomery Street
Alexandria, Virginia 22314

Professor F.K. Lamb
University of Illinois at
Urbana-Champaign
Department of Physics
1110 West Green Street
Urbana, IL 61801

Dr. Arthur Lerner-Lam
Lamont-Doherty Geological Observatory
of Columbia University
Palisades, NY 10964

Dr. L. Timothy Long
School of Geophysical Sciences
Georgia Institute of Technology
Atlanta, GA 30332

Dr. Peter Malin
University of California at
Santa Barbara
Institute for Central Studies
Santa Barbara, CA 93106

Dr. George R. Mellman
Sierra Geophysics
11255 Kirkland Way
Kirkland, WA 98033

Dr. Bernard Minster
ICPP, A-205
Scripps Institute of Oceanography
Univ. of California, San Diego
La Jolla, CA 92093

Professor John Nabelek
College of Oceanography
Oregon State University
Corvallis, OR 97331

Dr. Geza Nagy
U. California, San Diego
Dept of Ames, M.S. B-010
La Jolla, CA 92093

Dr. Jack Oliver
Department of Geology
Cornell University
Ithaca, NY 14850

Dr. Robert Phinney/Dr. F. A. Dahlen
Dept of Geological
Geological Science University
Princeton University
Princeton, NJ 08540

RADIX System, Inc.
Attn: Dr. Jay Pulli
2 Taft Court, Suite 203
Rockville, Maryland 20850

Dr. Norton Rimer
S-CUBED
A Division of Maxwell Laboratory
P.O. 1620
La Jolla, CA 92038-1620

Professor Larry J. Ruff
Department of Geological Sciences
1006 C.C. Little Building
University of Michigan
Ann Arbor, MI 48109-1063

Dr. Richard Sailor
TASC Inc.
55 Walkers Brook Drive
Reading, MA 01867

Thomas J. Sereno, Jr.
Service Application Int'l Corp.
10210 Campus Point Drive
San Diego, CA 92121

Dr. David G. Simpson
Lamont-Doherty Geological Observ.
of Columbia University
Palisades, NY 10964

Dr. Bob Smith
Department of Geophysics
University of Utah
1400 East 2nd South
Salt Lake City, UT 84112

Dr. S. W. Smith
Geophysics Program
University of Washington
Seattle, WA 98195

Dr. Stewart Smith
IRIS Inc.
1616 N. Fort Myer Drive
Suite 1440
Arlington, VA 22209

Rondout Associates
ATTN: Dr. George Sutton,
Dr. Jerry Carter, Dr. Paul Pomeroy
P.O. Box 224
Stone Ridge, NY 12484 (4 copies)

Dr. L. Sykes
Lamont Doherty Geological Observ.
Columbia University
Palisades, NY 10964

Dr. Pradeep Talwani
Department of Geological Sciences
University of South Carolina
Columbia, SC 29208

Dr. R. B. Tittmann
Rockwell International Science Center
1049 Camino Dos Rios
P.O. Box 1085
Thousand Oaks, CA 91360

Professor John H. Woodhouse
Hoffman Laboratory
Harvard University
20 Oxford St.
Cambridge, MA 02138

Dr. Gregory B. Young
ENSCO, Inc.
5400 Port Royal Road
Springfield, VA 22151-2388

FOREIGN (OTHERS)

Dr. Peter Basham
Earth Physics Branch
Geological Survey of Canada
1 Observatory Crescent
Ottawa, Ontario
CANADA K1A 0Y3

Professor Ari Ben-Menahem
Dept of Applied Mathematics
Weizman Institute of Science
Rehovot
ISRAEL 951729

Dr. Edward Berg
Institute of Geophysics
University of Hawaii
Honolulu, HI 96822

Dr. Michel Bouchon - Universite
Scientifique et Medicale de Grenou
Lab de Geophysique - Interne et
Tectonophysique - I.R.I.G.M-B.P.
38402 St. Martin D'Heres
Cedex FRANCE

Dr. Hilmar Bungum/NTNF/NORSAR
P.O. Box 51
Norwegian Council of Science,
Industry and Research, NORSAR
N-2007 Kjeller, NORWAY

Dr. Michel Campillo
I.R.I.G.M.-B.P. 68
38402 St. Martin D'Heres
Cedex, FRANCE

Dr. Kin-Yip Chun
Geophysics Division
Physics Department
University of Toronto
Ontario, CANADA M5S 1A7

Dr. Alan Douglas
Ministry of Defense
Blacknest, Brimpton,
Reading RG7-4RS
UNITED KINGDOM

Dr. Manfred Henger
Fed. Inst. For Geosciences & Nat'l Res.
Postfach 510153
D-3000 Hannover 51
FEDERAL REPUBLIC OF GERMANY

Ms. Eva Johannisson
Senior Research Officer
National Defense Research Inst.
P.O. Box 27322
S-102 54 Stockholm
SWEDEN

Tormod Kvaerna
NTNF/NORSAR
P.O. Box 51
N-2007 Kjeller, NORWAY

Mr. Peter Marshall, Procurement
Executive, Ministry of Defense
Blacknest, Brimpton,
Reading RG7-4RS
UNITED KINGDOM (3 copies)

Dr. Robert North
Geophysics Division
Geological Survey of Canada
1 Observatory Crescent
Ottawa, Ontario
CANADA, K1A 0Y3

Dr. Frode Ringdal
NTNF/NORSAR
P.O. Box 51
N-2007 Kjeller, NORWAY

Dr. Jorg Schlittenhardt
Federal Inst. for Geosciences & Nat'l Res.
Postfach 510153
D-3000 Hannover 51
FEDERAL REPUBLIC OF GERMANY

University of Hawaii
Institute of Geophysics
ATTN: Dr. Daniel Walker
Honolulu, HI 96822

FOREIGN CONTRACTORS

Dr. Ramon Cabre, S.J.
Observatorio San Calixto
Casilla 5939
La Paz Bolivia

Professor Peter Harjes
Institute for Geophysik
Rhur University/Bochum
P.O. Box 102148, 4630 Bochum 1
FEDERAL REPUBLIC OF GERMANY

Dr. E. Husebye
NTNF/NORSAR
P.O. Box 51
N-2007 Kjeller, NORWAY

Professor Brian L.N. Kennett
Research School of Earth Sciences
Institute of Advanced Studies
G.P.O. Box 4
Canberra 2601
AUSTRALIA

Dr. B. Massinon
Societe Radiomana
27, Rue Claude Bernard
7,005, Paris, FRANCE (2 copies)

Dr. Pierre Mechtier
Societe Radiomana
27, Rue Claude Bernard
75005, Paris, FRANCE

Dr. Svein Mykkeltveit
NTNF/NORSAR
P.O. Box 51
N-2007 Kjeller, NORWAY (3 copies)

GOVERNMENT

Dr. Ralph Alewine III
DARPA/NMRO
1400 Wilson Boulevard
Arlington, VA 22209-2308

Dr. Robert Blandford
DARPA/NMRO
1400 Wilson Boulevard
Arlington, VA 22209-2308

Sandia National Laboratory
ATTN: Dr. H. B. Durham
Albuquerque, NM 87185

Dr. Jack Evernden
USGS-Earthquake Studies
345 Middlefield Road
Menlo Park, CA 94025

U.S. Geological Survey
ATTN: Dr. T. Hanks
Nat'l Earthquake Resch Center
345 Middlefield Road
Menlo Park, CA 94025

Dr. James Hannon
Lawrence Livermore Nat'l Lab.
P.O. Box 808
Livermore, CA 94550

Paul Johnson
ESS-4, Mail Stop 1979
Los Alamos National Laboratory
Los Alamos, NM 87545

Ms. Ann Kerr
DARPA/NMRO
1400 Wilson Boulevard
Arlington, VA 22209-2308

Dr. Max Koontz
US Dept of Energy/DP 5
Forrestal Building
1000 Independence Ave.
Washington, D.C. 20585

Dr. W. H. K. Lee
USGS
Office of Earthquakes, Volcanoes,
& Engineering
Branch of Seismology
345 Middlefield Rd
Menlo Park, CA 94025

Dr. William Leith
U.S. Geological Survey
Mail Stop 928
Reston, VA 22092

Dr. Richard Lewis
Dir. Earthquake Engineering and
Geophysics
U.S. Army Corps of Engineers
Box 631
Vicksburg, MS 39180

Dr. Robert Masse!
Box 25046, Mail Stop 967
Denver Federal Center
Denver, Colorado 80225

Richard Morrow
ACDA/VI
Room 5741
320 21st Street N.W.
Washington, D.C. 20451

Dr. Keith K. Nakanishi
Lawrence Livermore National Laboratory
P.O. Box 808, L-205
Livermore, CA 94550 (2 copies)

Dr. Carl Newton
Los Alamos National Lab.
P.O. Box 1663
Mail Stop C335, Group ESS-3
Los Alamos, NM 87545

Dr. Kenneth H. Olsen
Los Alamos Scientific Lab.
P.O. Box 1663
Mail Stop C335, Group ESS-3
Los Alamos, NM 87545

Howard J. Patton
Lawrence Livermore National
Laboratory
P.O. Box 808, L-205
Livermore, CA 94550

Mr. Chris Paine
Office of Senator Kennedy
SR 315
United States Senate
Washington, D.C. 20510

AFOSR/NP
ATTN: Colonel Jerry J. Perrizo
Bldg 410
Bolling AFB, Wash D.C. 20332-6448

HQ AFTAC/TT
Attn: Dr. Frank F. Pilotte
Patrick AFB, Florida 32925-6001

Mr. Jack Rachlin
USGS - Geology, Rm 3 C136
Mail Stop 928 National Center
Reston, VA 22092

Robert Reinke
AFWL/NTEG
Kirtland AFB, NM 87117-6008

Dr. Byron Ristvet
HQ DNA, Nevada Operations Office
Attn: NVCG
P.O. Box 98539
Las Vegas, NV 89193

HQ AFTAC/TGR
Attn: Dr. George H. Rothe
Patrick AFB, Florida 32925-6001

Donald L. Springer
Lawrence Livermore National Laboratory
P.O. Box 808, L-205
Livermore, CA 94550

Dr. Lawrence Turnbull
OSWR/NED
Central Intelligence Agency
CIA, Room 5G48
Washington, D.C. 20505

Dr. Thomas Weaver
Los Alamos National Laboratory
P.O. Box 1663
MS C 335
Los Alamos, NM 87545

GL/SULL
Research Library
Hanscom AFB, MA 01731-5000 (2 copies)

Secretary of the Air Force (SAFRD)
Washington, DC 20330
Office of the Secretary Defense
DDR & E
Washington, DC 20330

HQ DNA
ATTN: Technical Library
Washington, DC 20305

DARPA/RMO/RETRIEVAL
1400 Wilson Blvd.
Arlington, VA 22209

DARPA/RMO/Security Office
1400 Wilson Blvd.
Arlington, VA 22209

GL/XO
Hanscom AFB, MA 01731-5000

GL/LW
Hanscom AFB, MA 01731-5000

DARPA/PM
1400 Wilson Boulevard
Arlington, VA 22209

Defense Technical
Information Center
Cameron Station
Alexandria, VA 22314
(5 copies)

Defense Intelligence Agency/
Directorate for Scientific &
Technical Intelligence
Washington, D.C. 20301

Defense Nuclear Agency/SPSS
ATTN: Dr. Michael Shore
6801 Telegraph Road
Alexandria, VA 22310

AFTAC/CA (STINFO)
Patrick AFB, FL 32925-6001

Dr. Gregory van der Vink
Congress of the United States
Office of Technology Assessment
Washington, D.C. 20510

Mr. Alfred Lieberman
ACDA/VI-OA'State Department Building
Room 5726
320 - 21st Street, NW
Washington, D.C. 20451

TACTEC
Battelle Memorial Institute
505 King Avenue
Columbus, OH 43201 (Final report only)